

Measurement of α_s with Scaling violations in e^+e^- annihilations ¹

Cristòfol Padilla
Universitat Autònoma de Barcelona
Institut de Física d'Altes Energies
Edifici C E-08193 Bellaterra (Barcelona) Spain

1995

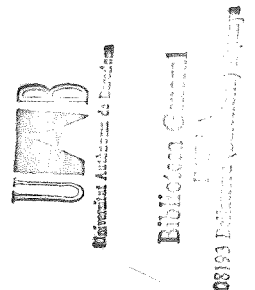
¹Phd disertation



Measurement of α_s with Scaling violations in e^+e^- annihilations ¹

Cristòfol Padilla
Universitat Autònoma de Barcelona
Institut de Física d'Altes Energies
Edifici C E-08193 Bellaterra (Barcelona) Spain

1995



¹Phd disertation

Contents

1	Introduction	1
2	theory	3
2.1	QCD	3
2.1.1	QCD lagrangian	4
2.1.2	Group structure and Color factors	5
2.1.3	The running coupling constant and RGE	6
2.2	Transverse and Longitudinal distributions	7
2.2.1	Fragmentation functions	9
2.2.2	Normalization of the total cross-section	12
2.3	Evolution of the fragmentation Functions	12
2.4	Power-law corrections	14
2.4.1	Kinematic corrections	15
2.4.2	Heavy quark masses	15
2.4.3	Heavy quark decays	16
2.4.4	Hadronization effects	18
3	The ALEPH detector	20
3.1	LEP	20
3.2	The ALEPH detector: general description	22
3.3	Subdetectors relevant to the analysis	30
3.3.1	The Mini Vertex Detector	30
3.3.2	The Inner Tracking Chamber	31
3.3.3	The Time Projection Chamber	32
3.3.4	The Electromagnetic and Hadronic Calorimeters	36
4	Event reconstruction and simulation	40
4.1	Tracking in ALEPH	40
4.1.1	Coordinate finding	40
4.1.2	Track Reconstruction	42
4.2	Energy and position reconstruction with the calorimeters	44
4.3	Energy flow determination	44
4.4	flavour tagging algorithms	47

4.4.1	Impact parameter tag	47
4.4.2	Event shape tag	51
4.5	The Event Simulation	53
5	Data used in the analysis	54
5.1	Selection of hadronic events	54
5.2	Scaled energy non-flavour tagged distribution	55
5.3	Enriched flavour distributions.	60
5.4	Correlation between the quark distributions	67
5.4.1	Normalization errors	67
5.4.2	Common-tracks correlations	67
5.5	Three-jet events gluons distribution	68
5.6	Transverse and longitudinal distribution	69
5.7	Low energy data	74
6	Description of the analysis	76
6.1	Evaluation of the Convolution Integrals	78
6.2	Methods to solve the Evolution equations	80
6.2.1	Runge-Kuta Method	80
6.2.2	Moments analysis method	81
6.3	Parametrization of the fragmentation functions	83
6.4	Parametrization of the non-perturbative terms	84
6.4.1	Non-perturbative terms in the Moments analysis	86
6.4.2	Monte Carlo study	87
6.5	Choice of parametrization scale	90
6.6	Results of the fit	91
6.7	Systematic errors	94
6.7.1	Experimental systematic errors	94
6.7.2	Theoretical errors	95
6.8	Consistency checks	97
6.8.1	Parametrization scale variation	97
6.8.2	Parametrization of the non-perturbative effects	97
6.8.3	Dependence on the fit range	98
6.8.4	Different experiment combinations	99
7	Summary and conclusions	105
A	Electro-weak cross-sections	107
B	Coefficient functions and Splitting Kernels	109
B.1	Coefficient functions	109
B.2	Evolution splitting kernels	110
B.2.1	Evolution of Flavour Non-Singlet Fragmentation Functions	111
B.2.2	Evolution of the Flavour Singlet Fragmentation Functions	112

List of Figures

2.1	Feynman diagrams contributing to first order in α_s to the x-inclusive distributions.	10
3.1	The LEP ring	21
3.2	Scheme of the LEP injectors and accelerators.	22
3.3	Schematic view of the ALEPH detector.	24
3.4	Schematic representation of the FALCON cluster.	29
3.5	Cut-away view of the VDET	31
3.6	The ITC drift cells.	32
3.7	Scheme of the TPC	34
3.8	View of a TPC end-plate	35
3.9	View of a TPC wire chamber	35
3.10	Overall view of the Electromagnetic and Hadronic calorimeters . . .	37
3.11	View of an ECAL stack layer	38
4.1	Helix parameters used in the TPC tracking programs	43
4.2	Impact parameter with respect to the coordinate origin and with respect to the beam spot centroid.	48
4.3	Definition of the signed impact parameter.	49
4.4	Moment of inertia and Lateral Mass distributions	52
5.1	All flavour detailed distributions	58
5.2	Cut variation systematics.	60
5.3	b enriched flavour detailed distributions	63
5.4	c enriched flavour detailed distributions	64
5.5	uds enriched flavour detailed distributions	65
5.6	Measured scaled energy distributions corrected measured by ALEPH. .	66
5.7	Scaled energy distribution measures in three jet simetric events by ALEPH.	69
5.8	Transverse detailed distributions	71
5.9	Longitudinal detailed distributions	72
5.10	Angular efficiency and differences between Monte Carlo and Real data	73
6.1	Scheme of the scaling violations analysis	76
6.2	Result of the leading moments analysis	89

6.3	Result of the fit	101
6.4	Residuals of the fit	102
	103	
6.6	Fragmentation functions result from the fit	104
A.1	Relative Electro-weak cross-section	108

List of Tables

3.1	Main LEP parameters.	23
5.1	Cut variation for the systematics computation.	59
5.2	Flavour composition of the different distributions considered in the analysis	62
5.3	Normalization errors for the scaled energy distributions used in the analysis	75
6.1	Monte-Carlo studies of non-perturbative correction	88
6.2	Results of the fit to all data	91
6.3	χ^2/n_{df} per experiment	93
6.4	$\alpha_s(M_Z)$ results for different tagged distributions	95
6.5	$\alpha_s(M_Z)$ results for different purities	96
6.6	Results of $\alpha_s(M_Z)$ for different factorization and renormalization scale assumptions.	96
6.7	$\alpha_s(M_Z)$ results for different fit intervals	99
6.8	$\alpha_s(M_Z)$ results for different fit intervals	99
6.9	$\alpha_s(M_Z)$ results with different sets of distributions	100
A.1	Vector and axial couplings	108
C.1	All flavour scaled energy inclusive distribution	116
C.2	uds-enriched scaled energy inclusive distribution	117
C.3	c-enriched scaled energy inclusive distribution	118
C.4	b-enriched scaled energy inclusive distribution	119
C.5	Gluon scaled energy distribution measured in three jet symmetric events.	120
C.6	All flavour scaled energy inclusive distribution	120
C.7	All flavour scaled energy inclusive distribution	121

Chapter 1

Introduction

The four LEP experiments have extensively studied the hadronic decays of the Z boson up to now. All results constrain the parameters of the theory of the strong interactions as being compatible with the Quantum Chromodynamics. The strong coupling constant, α_s , the only free parameter of the theory, has also been measured with a lot of different methods giving a precision that is now below 4%. This thesis presents a new test of QCD and a new measurement of α_s based on the study of scaling violations in fragmentation functions.

The study of scaling violations in structure functions in deep-inelastic lepton-nucleon scattering played a fundamental role in establishing Quantum Chromodynamics (QCD) as the theory of strong interactions. QCD predicts similar scaling violations in the fragmentation functions of quarks and gluons. In an electron-positron collider this translates into the fact that the distributions of the scaled-energy $x \equiv 2E/\sqrt{s}$ of final state particles in hadronic events depend on the centre-of-mass energy \sqrt{s} . These scaling violations come about because with increasing \sqrt{s} more phase space for gluon radiation and thus final state particle production becomes available, leading to a softer scaled energy distribution. As the probability for gluon radiation is proportional to the strong coupling constant, a measurement of the scaled-energy distributions at different centre-of-mass energies compared to the QCD prediction allows to determine the only free parameter of QCD, α_s .

In principle, variations with energy of the x distributions would establish the existence of scaling violations and allow the determination of α_s . However, the fact that the final state flavour composition depends strongly on the centre-of-mass energy (abundance of u -type quarks at PEP and PETRA energies and majority

of d -type quarks at LEP energies), and that the fragmentation functions depend on the quark mass, means that the effect would be biased by differences between fragmentation functions for the different quark flavours. Therefore, in order to disentangle scaling violations arising from gluon radiation from effects due to the changing flavour composition independently of Monte Carlo modeling, final state flavour identification is needed.

The fact that the scaled energy distributions measure all the particles produced after fragmentation and decay of the fragmented hadrons give contributions to the evolution that have nothing to do with QCD. Other effects come from the assumption of zero mass for the quarks and hadronization process. The measurement of the scaling violations and of the strong coupling constant will need that, either these effects are known or they have been demonstrated to not affect the perturbative QCD evolution.

The work presented here uses inclusive scaled-energy distributions of stable charged particles measured at PEP, PETRA, TRISTAN and LEP together with ALEPH measurements of the distributions in bottom-, charm- and light-quark enriched samples, an inclusive sample, and a gluon jet sample. These data, obtained in 1992 and 1993, correspond to approximately 40 pb^{-1} taken at a centre-of-mass energy around 91.2 GeV. They amount to close to 1.2 million hadronic decays of the Z .

Chapter 2 described the theoretical framework of the analysis which is based on the Dokshitzer-Gribov-Lipatov-Altarelli-Parisi (DGLAP) evolution equations with splitting kernels and coefficient functions computed to next-to-leading order. Chapter 3 gives a description of the main apparatus used for the analysis in the measurement of the inclusive and flavour-tagged and gluon scaled energy distributions, and the transverse and longitudinal cross-sections. This measurements need mainly the tracking reconstruction and special flavour tagging algorithms that are described in chapter 4. The measurement of the ALEPH and low energy data used in the analysis is described in chapter 5. The results are discussed in chapter 6. The final summary and conclusions is given in chapter ???. A list of appendix give some more detailed information on the formulas and data used.

Chapter 2

theory

After a brief introduction of the Quantum Chromodynamics theory with special emphasis in the running coupling constant, the longitudinal and transverse cross-sections are introduced. Their decomposition in fragmentation functions and the factorization theorem that leads to the energy dependent effective fragmentation functions that evolve following the evolution equation are introduced. Finally a theoretical study of the power-law corrections is given.

2.1 QCD

The theory of Quantum Chromodynamics was formulated about twenty years ago. It constitutes the part of the Standard Model [1] that describes the strong interactions of colored spin $1/2$ quarks with massless colored spin 1 gluons.

The fermions of the theory were formally introduced as constituents of mesons and baryons in the Gell-Mann-Zweig model [?]. It was realized that quarks are naturally associated with the pointlike constituents, named partons [?], discovered in deep inelastic lepton-nucleon scattering [?].

The concept of color [?] was introduced in order to avoid spin statistics problems appearing for baryons made out of three quarks with the same flavour, as for example the Δ^{++} resonance [?]. Assigning to the quarks a new quantum number, color, corresponding to a new symmetry, solves this problem. The number of colors was measured from the partial decay width of neutral pions into photons, which is proportional to N_c^2 [?] and from the total hadronic cross section in e^+e^-

annihilations, where it is proportional to N_c .

The gauge bosons are called gluons. They were introduced to explain hadrons as dynamically bound quark states. An important fact of QCD is that gluons carry color charge. Thus, they couple with other gluons apart to the quarks. As a consequence, vacuum polarization effects produce an anti-screening of the bare QCD charges, which results in a strong interactions at large distances and small at short distances. This explains the fact that quarks are not observed as free particles and leads to the concepts of confinements and asymptotic freedom.

2.1.1 QCD lagrangian

The fact that gluons are massless and have only two physical polarizations makes gauge invariance a desirable property of the lagrangian in order to perform covariant calculations adding two extra polarizations to the gluon fields. The QCD lagrangian density is then the Yang-Mills Lagrangian for an unbroken SU(3) gauge invariance and can be written as

$$\mathcal{L} = -\frac{1}{4}G_{\mu\nu}^a G_a^{\mu\nu} + \bar{q}_\alpha(i \not{D} - m)q^\alpha + \mathcal{L}^{\text{GF}} + \mathcal{L}^{\text{Ghost}} \quad (2.1)$$

with

$$G_{\mu\nu}^a = \partial_\mu A_\nu^a - \partial_\nu A_\mu^a + g f^{abc} A_\mu^b A_\nu^c \quad (2.2)$$

$$D_\mu = \partial_\mu - ig A_\mu^a T_F^a. \quad (2.3)$$

$q_\alpha = \{u_\alpha, d_\alpha, s_\alpha, c_\alpha, b_\alpha, t_\alpha\}$ represents the quark fields with color α , α having N_c (three) degrees of freedom. $m = \{m_q\}$ represents the quarks masses. A_μ^a is the gluon field, a being the gluon color index that has $N_c^2 - 1$ (eight) degrees of freedom. f^{abc} are the group structure constants and T_F^a the N_c dimension group generators in the fundamental representation. g is a gauge coupling constant related with the bare strong coupling constant, α_s , trough $\alpha_s = g^2/4\pi$.

\mathcal{L}^{GF} and $\mathcal{L}^{\text{Ghost}}$ are, respectively, the gauge fixing and ghost terms. The gauge fixing term is included to allow the inversion of the gluon propagator as is done in any gauge theory with massless gauge bosons. The Ghost term has to be included in non-abelian theories, where the gauge bosons interact among themselves, to cancel the non-physical contributions in those diagrams where these interactions appear.

They are given by

$$\mathcal{L}^{\text{GF}} = -\frac{1}{2\xi}(\partial^\mu G_\mu^a)(\partial^\nu G_\nu^a) \quad (2.4)$$

$$\mathcal{L}^{\text{Ghost}} = \partial^\mu \bar{\varphi}_a \nabla_{ab}^\mu \varphi^b \quad (2.5)$$

$$\nabla_{ab}^\mu = \delta_{ab} \partial^\mu - g f_{abc} A_c^\mu \quad (2.6)$$

being ξ a gauge fixing constant, which is, for example $\xi = 1$ in the Feynman gauge and $\xi = 0$ in the Landau gauge, and φ^b massless, hermitian, scalar fields with Fermi-Dirac statistics called ghosts fields.

The deduced Feynman rules for the above lagrangian can be found in any text-book [?]. From them, it can be deduced that the amplitude for a quark changing its color from α to β by emitting a gluon of type c is proportional to $g(T_F^c)_{\alpha\beta}$ and that the one for a gluons of type a changing to b by emitting a gluons of type c is proportional to gf^{abc} . Thus, the group structure constants and generators play an important role in strong interactions and they deserve a more careful study.

2.1.2 Group structure and Color factors

The structure constants are related to the generators, T^a , of the group through the relation

$$[T^a, T^b] = if^{abc} T_c. \quad (2.7)$$

Two important representations of the group are the fundamental ($N_F \times N_F$) = ($N_c \times N_c$) representation, which, in the case of SU(3) is

$$(T_F^a)_{\alpha\beta} = \frac{\lambda_{\alpha\beta}^a}{2} \quad (2.8)$$

being λ^a the Gell-Mann matrices, and the adjoint ($N_A \times N_A$) = ($N_c^2 - 1 \times N_c^2 - 1$) representation,

$$(T_A^a)_{\alpha\beta} = -if_{abc}. \quad (2.9)$$

From the relations (2.8) and (2.9), the following relations can be deduced:

$$\text{Tr}(T_F^a T_F^b) = T_F \delta^{ab} \quad , \quad \text{Tr}(T_A^a T_A^b) = C_A \delta^{ab} \quad , \quad (T_F^a T_F^b)_{\alpha\beta} = C_F \delta^{\alpha\beta} \quad (2.10)$$

being C_F the casimir operator of the fundamental (fermion) representation, C_A the casimir of the adjoint (gluon) representation and, T_F the factor that connects

both representations through $T_F = N_F C_F / N_A$. They are called ‘color factors’ and depend only on the gauge group of the theory. In QCD (SU(3)) they are given by

$$C_F = \frac{N_c^2 - 1}{2N_c} = \frac{4}{3} \quad , \quad C_A = N_c = 3 \quad , \quad T_F = \frac{1}{2}. \quad (2.11)$$

Since a factor C_F frequently appears accompanying the coupling constant α_s , it is common practice to define

$$a = \frac{\alpha_s C_F}{2\pi} \quad , \quad X = \frac{C_A}{C_F} \quad , \quad Z = n_f \frac{T_F}{C_F} \quad (2.12)$$

which are the couplant constant and the factors that parametrize the gauge structure of the underlying theory. n_f is the number of active flavours. Physically, they are the ratio of the gluon-self coupling to the quark gluons coupling (X) and the ratio of the $q\bar{q}$ splitting from a gluon to the quark-gluon coupling. The results of these constants has been found in agreement with the SU(3) QCD structure by the four LEP collaborations [?].

2.1.3 The running coupling constant and RGE

The lagrangian (2.1) contains only a free parameters: the gauge coupling constant, g or, equivalently, α_s . Supposing this is a small number, perturbation theory can be performed to have physical predictions. When this is done, there appear calculations of Feynmann diagrams that contain loops which are ultraviolet divergents. These divergences are first regularized [3] and then removed by absorbing them into the redefinition of the physical bare parameters through some renormalization procedure [4]. In this procedure, a dependence on an arbitrary scale, μ , is introduced. Since any physical quantity, $P(\alpha_s, m, \mu)$, must not depend on the value of μ , provided bare parameters g_B, m_B , are kept fixed, the renormalization group equation (RGE) must hold

$$\mu^2 \frac{d}{d\mu^2} P(\alpha_s, \mathbf{m}, \mu) \Big|_{g_B, m_B} = \left[\mu^2 \frac{\partial}{\partial \mu^2} + \beta(\alpha_s(\mu)) \frac{\partial}{\partial \alpha_s} + 2\bar{m}^2 \gamma_m(\alpha_s(\mu)) \frac{\partial}{\partial \bar{m}^2} \right] P(\alpha_s, \mathbf{m}, \mu) \Big|_{g_B, m_B} \equiv 0. \quad (2.13)$$

$\bar{m} = \bar{m}(\mu)$ are the running masses and $\alpha_s(\mu)$ is the running coupling constant. $\gamma_m(\alpha_s(\mu))$ is the mass anomalous dimension that will determine the functional form of the running masses with the scale μ . The β -function controls the renormalization

scale dependence of α_s though

$$\mu^2 \frac{d\alpha_s(\mu)}{d\mu^2} \Big|_{g_B, m_B} = \beta(\alpha_s) = - \sum_{i \geq 0} \beta_i \left(\frac{\alpha_s}{\pi} \right)^{i+2}. \quad (2.14)$$

The expansion of (2.14) is known up to three loops [5]. In the analysis, the two first coefficients are needed

$$\beta_0 = \left(11 - \frac{2}{3n_f} \right) / 4 \quad (2.15)$$

$$\beta_1 = \left(102 - \frac{38}{3n_f} \right) / 16. \quad (2.16)$$

These expressions and equation (2.14) allow to write an explicit solution for the running of α_s ,

$$\alpha_s(\sqrt{s}) = \frac{\alpha_s(\mu)}{w} \left(1 - \frac{\beta_1}{\beta_0} \frac{\alpha_s(\mu)}{4\pi} \frac{\ln w}{w} \right) \quad \text{with} \quad w = 1 - \beta_0 \frac{\alpha_s(\mu)}{4\pi} \ln \frac{\mu^2}{s} \quad (2.17)$$

which is exact to leading and next-to-leading logarithm accuracy, i.e. it contains all terms and only those terms of the full solution of the type $\alpha_s^n(\mu) \ln^m(\mu^2/s)$ with $m = n - 1, n - 2$.

The scale $\Lambda_{\overline{MS}}$ at which the strong coupling constant becomes infinite, is implicitly defined as

$$\alpha_s(\mu) = \frac{4\pi}{\beta_0 L} \left(1 - \frac{\beta_1}{\beta_0} \frac{\ln L}{L} \right) \quad \text{with} \quad L = \ln \frac{\mu^2}{\Lambda_{\overline{MS}}^2}. \quad (2.18)$$

In the analysis of scaling violations performed, a representation is chosen that express the running couplant, $a(s)$, as a function of the strong couplant at a reference scale, M_Z , though

$$a(s) = \frac{a(M_Z^2)}{w} \left(1 - a(M_Z^2) \frac{b_1}{b_0} \frac{\ln w}{w} \right) \quad \text{with} \quad w = 1 - a(M_Z^2) b_0 \ln \left(\frac{M_Z^2}{s} \right) \quad (2.19)$$

where

$$b_0 = \frac{2}{C_F} \beta_0 \quad \text{and} \quad b_1 = \left(\frac{2}{C_F} \right)^2 \beta_1. \quad (2.20)$$

2.2 Transverse and Longitudinal distributions

The single inclusive particle spectrum produced in the process $e^+e^- \rightarrow \text{hadrons}$ can be written as a sum of a 'transverse' (T), a 'longitudinal' (L) and an 'asymmetric'

(A) cross section:

$$\frac{d^2\sigma(s)}{dx d\cos\theta} = \frac{3}{8}(1 + \cos^2\theta) \frac{d\sigma^T(s)}{dx} + \frac{3}{4}\sin^2\theta \frac{d\sigma^L(s)}{dx} + \frac{3}{4}\cos\theta \frac{d\sigma^A(s)}{dx} \quad (2.21)$$

Here θ is the polar angle of the produced particle with respect to the beam direction. The Lorentz-invariant variable x is defined through $x = 2(k \cdot Q)/(Q \cdot Q)$ where k is the 4-momentum of the produced hadron and Q the 4-momentum of the virtual photon or Z . In the centre-of-mass frame of the collision (which is the laboratory frame of an e^+e^- -collider if initial state radiation can be neglected) it reduces to $x = E_{hadron}/E_{beam}$.

The first term, proportional to $(1 + \cos^2\theta)$, has its origin in fragmentation of the original quarks while the second one would not be present in a theory without gluon radiation. A physical insight of their origin can be given considering the initial and final spin states. In e^+e^- annihilations, the electron and positron spins are oriented along the beam line in such a way that the system is in a state of angular momentum of the form $|J, J_z\rangle = |1, \pm 1\rangle$ corresponding to the transverse polarizations of the virtual boson formed in the collision. Then, two particles are emitted forming an angle θ with the beam line in a state of angular momentum characterized by $|J, J_{z'}\rangle = |1, \pm 1\rangle$, where z' is the axis defined by the direction of the outgoing particles. The transition amplitude for this event to happen is then proportional to

$$\langle 1, \pm 1 | e^{-i\theta J_y} | 1, \pm 1 \rangle = d_{\pm 1, \pm 1}^1 = \frac{1}{2}(1 \pm \cos\theta) \quad (2.22)$$

which, averaging its square over the initial states, gives the expected angular behaviour. If now, a gluon (of spin 1) is radiated from one of the outgoing quarks, the final state could be characterized by $|J, J_{z'}\rangle = |1, 0\rangle$, thus giving terms proportional to

$$d_{0, \pm 1(-1)}^1 = \pm \frac{\sin\theta}{\sqrt{2}}, \quad (2.23)$$

which are the ones forming part of the longitudinal term in equation (2.21)

The third term has its origin in parity-violating terms that will not be used in this analysis.

Integration over $\cos\theta$ of eq. (2.21) yields the scaled energy spectrum.

$$\frac{1}{\sigma_{tot}} \frac{d\sigma(s)}{dx} = \frac{1}{\sigma_{tot}} \frac{d\sigma^T(s)}{dx} + \frac{1}{\sigma_{tot}} \frac{d\sigma^L(s)}{dx}. \quad (2.24)$$

which has been defined in such a way that the integral gives the average number of particles dividing by the total cross section, σ_{tot} .

2.2.1 Fragmentation functions

In perturbative QCD, an expression can be computed for the transverse and longitudinal cross-sections. In the naive parton model, the transverse differential cross-sections are given by

$$\frac{d\sigma^T(s)}{dx} = 2\sigma_0(s) \sum_{i=u,d,s,c,b} w_i(s) \mathcal{D}_{0,i}(x) \quad (2.25)$$

and the longitudinal cross-section is zero. In equation (2.25), $\sigma_0(s)$ is the Born cross section at a centre-of-mass $\sqrt{s} \equiv Q$, $w_i(s)$ are the relative electro-weak cross sections for the production of primary quarks of type i which explicit expressions are given in appendix ??, and $\mathcal{D}_{0,i}(x)$ are the bare fragmentation functions that give the probability of having an hadron of fractional beam energy x proceeding from the fragmentation of a quark or an antiquark q_i and defined as the mean of the fragmentation of a quark and and antiquark of the same flavour, as

$$\mathcal{D}_{0,q} = \frac{1}{2} (q(x) + \bar{q}(x)) \quad (2.26)$$

The fact that the total energy carried out by all fragments is equal to that of the original parton implies the following sum rule for the *bare fragmentation functions*

$$\int_0^1 dz z \mathcal{D}_{0,i}(x) = 1. \quad (2.27)$$

Proceeding beyond the zeroth order in α_s , before the quark fragments into the hadron, it can radiate a gluon. Therefore, the probability of having an hadron in the momentum region between z and dz is given by

$$\left(\frac{d\sigma^{T,L}}{dx}(s) \right) dx = \left(\frac{d\sigma_q^{T,L}}{dz}(s) \right) dz \mathcal{D}_{0,q}(y) dy + \left(\frac{d\sigma_g^{T,L}}{dz}(s) \right) dz \mathcal{D}_{0,g}(y) dy \quad (2.28)$$

where $(d\sigma_{g(g)}^{T,L}/dz(s))dz$ is the probability of finding a quark(gluon) with energy

$$E_{q(g)} = \frac{1}{2} z Q \quad (2.29)$$

in an angular momentum final state $|1, \pm 1\rangle$ (transverse) of $|1, 0\rangle$ (longitudinal), and $\mathcal{D}_{0,q(g)}(y) dy$ is the probability that this quark (gluon) fragments into a hadron carrying fractional energy

$$y = E_h / E_{q(g)}. \quad (2.30)$$

The outside experimental variable, z , is related to the two inside parton variable through

$$y = z/z. \quad (2.31)$$

Figure 2.1: Feynman graphs for the parton subprocess $Z \rightarrow q + \text{anything}$, contributing to the reaction $e^+e^- \rightarrow h + \text{anything}$. The cross denotes the quark which fragments to the observed hadron h .

The cross section for having real quark or gluon are given by the Feynman diagrams of figure ??(a). Their calculation contains infrared or soft divergences, and parallel or mass singularities. The first ones occur when the energy of the emitted gluon or its mass tends to zero. The second one occurs when the gluon is emitted parallel to the quark or the mass of the quark tends to zero being the gluon mass zero. The virtual diagrams of figure ??(b) contain ultraviolet divergences that

cancel when summed all together. However, some infrared divergences and mass singularities remain. All the divergences will cancel when the total cross-section is computed (the integral over x of the scaled energy distribution) but, the differential cross-section of equation (2.28) leads to a functional form

$$\frac{d\sigma^{T,L}}{dx}(s) = 2\sigma_0 \int_x^1 \frac{dz}{z} \mathcal{D}_{0,i}\left(\frac{x}{z}\right) \left[\delta(1-z) + \frac{\alpha_s}{2\pi} R_i(z) \log\left(\frac{s}{m^2}\right) + \alpha_s f_i(z) \right] \quad (2.32)$$

where i runs over all the flavours and the gluon. m is the scale that appears in the regularization of the mass singularities.

The coefficient accompanying the logarithmic part is not dependent on the regularization scheme used but the f_i functions are. Moreover, formula is not only regularization scheme dependent but is also divergent as $m \rightarrow 0$. Since the cross-section is a measurable quantity, the bare fragmentation functions, which cannot be measured, should have some mass dependence that cancels the mass singularities. However still remains the problem of the regularization scheme dependence on f_i .

The way to solve the problem consist in absorbing all the mass singularities and the ambiguity of the f_i functions in a redefinition of the bare fragmentation functions, which then become

$$D_i(z, \mu_F^2) = \int_z^1 \frac{dy}{y} \mathcal{D}_{0,i} \left[\delta(1-y) + \frac{\alpha_s}{2\pi} R_i(y) \log\left(\frac{\mu_F^2}{m^2}\right) + \alpha_s g_i(z) \right] \quad (2.33)$$

and are scale dependent. $D_i(z, \mu_F^2)$ are called the effective fragmentation functions.

With the definition of the effective fragmentation functions, and taking into account the running of α_s , equation (2.32) becomes,

$$\begin{aligned} \frac{d\sigma^{T,L}(s)}{dx} &= 2\sigma_0(s) \int_x^1 \frac{dz}{z} C_q^{T,L}(z, \alpha_s(\mu_F), \mu_F^2/s) \sum_{i=u,d,s,c,b} w_i(s) D_i(x/z, \mu_F^2) \\ &+ 2\sigma_0(s) \int_x^1 \frac{dz}{z} C_g^{T,L}(z, \alpha_s(\mu_F), \mu_F^2/s) D_g(x/z, \mu_F^2). \end{aligned} \quad (2.34)$$

The $C_{g,q}^{T,L}$ are the so called coefficient functions. This procedure is called mass factorization and its validity is ensured by the general factorization theorem [?]. The separation of the singular part in equation (2.32) from the remaining finite part (the coefficient functions) takes place at a factorization scale, μ_F , which relates the short distance ('partonic') from the long distance ('hadronic') effects.

The coefficient functions reduce to the parton model at first order. They have been computed up to next-to-leading order and their expressions are given in section ?? in appendix B.

The coefficient functions for the transverse and longitudinal cross-section give the relation

$$\frac{1}{\sigma_{tot}} \frac{d\sigma^L}{dx} = \frac{\alpha_s}{2\pi} \int_x^1 \frac{dz}{z} \left[\frac{1}{\sigma_{tot}} \frac{d\sigma^T}{dz} + 4 \left(\frac{z}{x} - 1 \right) D_g(z) \right] + \mathcal{O}(\alpha_s^2), \quad (2.35)$$

from where additional information of the gluon fragmentation function can be extracted.

2.2.2 Normalization of the total cross-section

Since what is usually measured are the scaled energy distribution of equation (2.24), expression (2.34) will contain the ratios of the total cross-section, σ_{tot} and the born cross-section, σ_0 . This can be computed integrating the differential cross-sections. Up to first order in α_s ,

$$\sigma_T = \sigma_0 \quad , \quad \sigma_L = \frac{\alpha_s}{\pi} \sigma_0. \quad (2.36)$$

Thus, the ratio of the two cross-sections is given by

$$\frac{\sigma_{tot}}{\sigma_0} = 1 + \frac{3}{2} \frac{\alpha_s}{2\pi} C_F = \frac{3}{2} a. \quad (2.37)$$

Equations (2.36) and (2.37) show that, up to first order in α_s , the total correction to σ_{tot} comes from the longitudinal cross-section. Higher orders have been computed for the α_s corrections to the total cross section [?], but not the contributions of the transverse and longitudinal cross-sections. Thus, it is not known whether this remains to higher orders.

2.3 Evolution of the fragmentation Functions

Although the effective fragmentation functions cannot be computed perturbatively, their change with the energy is predicted in perturbative QCD. This change is governed by the Dokshitzer-Gribov-Lipatov-Altarelli-Parisi (DGLAP) evolution [?] equations that can be written as

$$\frac{dD_j(x, s)}{d \ln s} = \sum_{i=u,d,s,c,b,g} \int_x^1 \frac{dz}{z} P_{ij}(z, \alpha_s(\mu_R), \mu_R^2/s) D_i(x/z, s) \quad (2.38)$$

where the splitting kernels (P_{ij}) are known to next-to-leading order accuracy and contain also all the leading log terms

$$P_{ij}(x, \alpha_s(\mu_R), \mu_R^2/s) = \frac{\alpha_s(\mu_R)}{2\pi} P_{ij}^{(0)}(x) + \left(\frac{\alpha_s(\mu_R)}{2\pi} \right)^2 P_{ij}^{(1)}(x, \frac{\mu_R^2}{s}) \quad (2.39)$$

The renormalization scale, μ_R , relates the splitting functions at a given scale \sqrt{s} to the strong coupling constant at the renormalization point μ_R . The indices i, j run over all active quark flavours and the gluon. What equation (2.38) tells is that the logarithmic energy change in the effective fragmentation functions is due to processes in which a quark or a gluon (partons) with a given scaled energy higher than x (the scaled energy of the observed hadron) radiate becoming another parton of fractional energy z (the probability of this being proportional to the corresponding splitting kernel) that afterwards fragments into the hadron. The probability of the last fragmentation is given by the probability of having an hadron of scaled energy x in a jet of energy z/E_{beam} . The sum takes into account all the cases with $z > x$.

Up to first order in α_s , the dependence on $\ln s$ on the quark fragmentation functions is due to two processes: the quarks can radiate a gluon and then fragment; or it can radiate a gluon which then fragments to the hadron. Analogously, the change in the gluon fragmentation function can be due to the gluon splitting to produce a quark that then fragments or it can pair-produce gluons which then fragment to the observed hadrons.

In higher order, other possibilities arise. A quark can split into a quark of different flavour, or to an antiquark of the same or different flavour before the fragmentation takes place.

It is most convenient to write the coupled system of evolution equations in (2.38) in terms of *singlet* and *non-singlet* parts defined as

$$S(x, s) = \frac{1}{n_f} \sum_{i=u,d,s,c,b} x D_i(x, s) \quad \text{and} \quad N_i(x, s) = x D_i(x, s) - S(x, s) \quad (2.40)$$

where the singlet and non-singlet components have been defined with the x -weighted particle spectra. This definition, which slightly deviates from common practice, results in a less singular behaviour for $x \rightarrow 0$. The evolution equations then become

$$s \frac{d}{ds} N_i(x, s) = \int_x^1 dz P_N(z, \alpha_s(\mu_R), \mu_R^2/s) N_i(\frac{x}{z}, s) \quad (2.41)$$

for the *non-singlet* components, while evolution of the singlet components is described by the coupled system

$$\begin{aligned} s \frac{d}{ds} G(x, s) &= \int_x^1 dz \left[P_{GG}(z, s, \mu_R) G\left(\frac{x}{z}, s\right) + P_{GQ}(z, s, \mu_R) S\left(\frac{x}{z}, s\right) \right] \\ s \frac{d}{ds} S(x, s) &= \int_x^1 dz \left[P_{QG}(z, s, \mu_R) G\left(\frac{x}{z}, s\right) + P_{QQ}(z, s, \mu_R) S\left(\frac{x}{z}, s\right) \right] \end{aligned} \quad (2.42)$$

where $G(x, s) \equiv x D_G(x, s)$ is used. The terms containing $P_Q Q$ and $P_G G$ are called the diagonal parts and $P_G Q$ and $P_Q G$ the off-diagonal parts. The expressions of the splitting kernels used in the analysis are given in section B.2 in appendix B.

2.4 Power-law corrections

The theory described in section 2.3 concerning the evolution of the fragmentation functions is not complete. All the equations were developed with the assumption of zero mass quark. This is not true at all, at least for charm and bottom quarks and, the effects that their masses in the evolution, could induce some corrections that should be controlled. The fact that the theory describes the evolution of scaled-energy distributions and that what is usually measured is the scaled-momentum distributions can also produce some corrections.

The fragmentation functions have been defined after the fragmentation stage. It is known that heavy flavour quarks fragment in a heavy hadron that carries most of the initial quark momentum and some light hadrons that share the rest of the initial momentum. This would produce a hard fragmentation function that, after decay, would finally give the softer observed fragmentation function for these flavours. The last step in the formation of them is not governed by QCD and it should not be considered in the evolution. Since the fragmentation functions before the decay are not easy to measure, it is necessary to work with some redefined fragmentation functions that include the decay of the heavy hadrons. The fact that the evolution is made in the final fragmentation function is only a practical matter and, again, the effect that this could induce in the evolution should be studied and controlled.

Finally the fragmentation itself is a non-perturbative phenomena that, for sure, induce corrections to the evolution. This is a less known effect that has to be parametrized somehow into the evolution.

2.4.1 Kinematic corrections

The simplest Power-law correction comes from the fact that the momentum fraction, $x_p = 2p/Q$ is used instead of the energy fraction, $x = 2E/Q$. The relation between the two approaches is given by

$$x = x_p + \frac{2m^2}{xQ^2} + \mathcal{O}(1/q^4). \quad (2.43)$$

The largest corrections come from considering the minimum values of x and energies in the analysis. In this regions, the corrections are of the order of the systematic errors, being even smaller at any other values.

2.4.2 Heavy quark masses

The coefficient functions and splitting kernels computed presented in section ?? assumed no mass for the quark production and fragmentation. This is a good approximation for the light quarks, but for heavy quarks, and specially for the b quark fragmentation, with 5 GeV of mass, this could not be the case.

In case the masses of the quarks are considered, the coefficient functions have to be recomputed. In [2] a full list of all the coefficient functions up to order α_s is given.

As an example, the coefficient function C_g^L is modified to

$$\begin{aligned} 2\sigma_0(s)C_g^L &= \sigma^{(a)}(s) \left[\rho \frac{\rho + x^2 + 2x - 4}{x} \ln \frac{1 + \beta_x}{1 - \beta_x} + 2\beta_x(2 + \rho) \frac{1 - x}{x} \right] \\ &+ \sigma^{(v)}(s) \left[-\frac{2\rho}{x} \ln \frac{1 + \beta_x}{1 - \beta_x} + 4\beta_x \frac{1 - x}{x} \right] \end{aligned} \quad (2.44)$$

where $\beta_x = \sqrt{1 - \rho/(1 - x)}$ and $\rho = 4m^2/s$ being m the mass of the heavy hadron. When the mass is set to zero, $\rho \rightarrow 1$ and expression (2.44) reduces to the one given in equation (B.1). The same procedure can be performed to the other coefficient functions.

From equation (2.44) it can be seen that all the corrections due to the mass of the hadron are of order ρ , that is, of at least two powers of m/Q . Thus, this corrections are expected to be small. Since they can be reabsorbed into the definition of the fragmentation functions at one energy, they only affect to the evolution process. Any

residual uncertainty can be taken into account with the variation of the factorization scale.

2.4.3 Heavy quark decays

The evolution equations contain the fragmentation functions of quarks. They describe the change of them, due only to perturbative QCD. However, experimentally, it is difficult to measure the fragmentation functions of the heavy quarks, since a full reconstruction of their decay would be necessary. Instead, the total scaled energy distribution after the decay to lighter product of the heavy hadrons produced from the fragmentation of a heavy quark, is easy to measure. This section describes the corrections to the evolution from using the 'total' fragmentation functions (after the decay) with respect to the 'true' one.

The probability of finding a particle with scaled energy x after fragmentation and decay of a quark is defined by

$$T_i(x, Q)dx = D_i(y, Q)dy \varphi_i(z, Q)dz \quad (2.45)$$

where $\varphi_i(z, Q)dz$ is the decay probability of the hadron. $x = 2E_d/Q$ is the fractional energy of the beam of the final decay product, $y = 2E_h/Q$ is the fractional energy of the beam taken by the hadron right after fragmentation, and $z = E_d/E_h = x/y$. The index i refers to the different quarks species. The total fragmentation function is then given by

$$T_i(x, Q) = \int_x^1 \frac{dy}{y} D_i(y, Q) \varphi_i\left(\frac{x}{y}, Q\right). \quad (2.46)$$

The evolution equations hold for the fragmentation functions $D_i(y, Q)$. But the measured cross-sections are related with $T_i(x, Q)$. The derivative of the later with respect to the $\ln Q$ is

$$\frac{\partial T_i(x, Q)}{\partial \ln Q} = A + B \quad (2.47)$$

The following definitions were introduced:

$$A \equiv \int_x^1 \frac{dy}{y} \varphi_i\left(\frac{x}{y}, Q\right) \frac{\partial D_i(y, Q)}{\partial \ln Q} \quad (2.48)$$

$$B \equiv \int_x^1 \frac{dy}{y} D_i(y, Q) \frac{\partial \varphi_i(x/y, Q)}{\partial \ln Q}. \quad (2.49)$$

The evolution equations can be applied to A , which can be written as

$$A = \int_x^1 \frac{dy}{y} \varphi_i \left(\frac{x}{y}, Q \right) \int_y^1 \frac{dz}{z} P_{ij}(z) D_j \left(\frac{y}{z}, Q \right). \quad (2.50)$$

Delta and step functions can be introduced in (2.50) as

$$A = \int \frac{dy}{y} \theta(1-y) \theta(y-x) \int d\xi \delta \left(\xi - \frac{x}{y} \right) \varphi_i(\xi, Q) \cdot \int \frac{dz}{z} \theta(1-z) \theta(z-y) P_{ij}(z) \int d\eta \delta \left(\eta - \frac{y}{z} \right) D_j(\eta, Q). \quad (2.51)$$

Taking into account that $\delta(\eta - y/z) = z\delta(y - z\eta)$ and performing the integrals over y and ξ

$$A = \int \frac{dz}{z} P_{ij}(z) \int \frac{d\eta}{\eta} D_j(\eta) \varphi_i \left(\frac{x/z}{\eta} \right) \cdot \theta(1 - z\eta) \theta(z\eta - x) \theta(1 - z) \theta(1 - \eta). \quad (2.52)$$

The φ_i will only act over the D_j with the same flavour. Since the index j runs over all the flavours, generalized T_j can be defined as the convolution of the fragmentation functions and the decay. The θ functions in (2.52) serve only to define the integration limits giving finally

$$\begin{aligned} A &= \int_x^1 \frac{dz}{z} P_{ij}(z) \int_{x/z}^1 \frac{d\eta}{\eta} D_j(\eta, Q) \varphi_i \left(\frac{x/z}{\eta} \right) \\ &= \int_x^1 \frac{dz}{z} P_{ij}(z) T_j \left(\frac{x}{z}, Q \right). \end{aligned} \quad (2.53)$$

The left side of (2.47) together with the result in (2.53) have the same structure as the evolution equations applied to the total fragmentation functions, T_i . Thus, the term in B would constitute non-QCD correction to the evolution equations coming from the decay effects included in T_i . The B term contains a derivative of the decay function, φ_i which can be written as

$$\int_x^1 d\xi \delta \left(\xi - \frac{x}{y} \right) \frac{\partial \varphi_i(\xi, Q)}{\partial \ln Q}. \quad (2.54)$$

The decay spectrum, $\varphi_i(\xi, Q)$, can be computed as the Lorentz boost of the rest frame spectrum, $\Phi_i(E^*)$. If E^* is the energy of the decay product in the heavy hadron rest frame and θ^* the angle of the decay particle with respect to the line of

flight of the heavy hadron in the centre-of-mass frame, the observed energy of the decay product can be written as

$$E = \frac{1}{2}\xi Q = \gamma E^* (1 + \beta \cos \theta^*) \quad (2.55)$$

where $\gamma = E_h/m$, being E_h and m the energy and mass of the heavy hadron, respectively. This allows to write φ_i as

$$\begin{aligned} \varphi_i(\xi, Q) = & \int d\cos^* \theta (1 - \cos \theta^*) \theta(\cos \theta^* + 1) \cdot \\ & \int dE^* \Phi_i(E^*) \delta \left[\xi - 2 \frac{\gamma E^*}{Q} (1 + \beta \cos \theta^*) \right] \end{aligned} \quad (2.56)$$

which can be integrated over $\cos \theta^*$ to finally have the following expression for the B correction:

$$B = \int_x^1 \delta \left(\xi - \frac{x}{y} \right) \frac{\partial}{\partial \ln Q} \int_{E/\alpha}^{E\alpha} \frac{dE^*}{E^*} \Phi_i(E^*) \frac{Q}{2} \frac{1}{\gamma\beta}. \quad (2.57)$$

The variable α was defined as

$$\alpha = \sqrt{\frac{1+\beta}{1-\beta}}. \quad (2.58)$$

The amount of correction can be traced if a decay to two particles are considered. In this case, equation (2.57) can be simplified to

$$\int_x^1 \delta \left(\xi - \frac{x}{y} \right) Q \frac{\partial}{\partial Q} \left[\frac{m}{y} \frac{2}{m} \left(\sqrt{1 - \frac{4m^2}{y^2 Q^2}} \right)^{-1} \right] \quad (2.59)$$

whose first term is of order m^2/Q^2 . In [2], a different approach based in the moments of the total fragmentation functions arrives to the same conclusion.

The conclusion is then that the effects of the decay of heavy hadrons in the evolution is, at least of two powers of m/Q which, at LEP energies is, for example of the order of 0.2% multiplied by the b fraction.

2.4.4 Hadronization effects

The hadronization effects are the less well known effects in the evolution. They have not been computed explicitly for the fragmentation functions neither for their evolution. In deep-inelastic scattering, they are known to go as $1/Q^2$ [?]. However,

no clear statement on their dependence with Q has been given for the case of e^+e^- collisions.

Nevertheless, the fact that corrections to the thrust and sphericity variables have been shown to go as $1/Q$ [52, 53]. Phenomenological arguments arrive to the same conclusion for the fragmentation functions. However, since no explicit calculation have been given, some parametrization has to be done.

Chapter 3

The ALEPH detector

The ALEPH detector [6, 7] (ALEPH: 'A detector for LEP PHysics') is one of the four large detectors installed in the LEP accelerator. The other three are DELPHI [8], L3 [9], and OPAL [10]. It was designed to study in detail the parameters of the Standard Electroweak model, to test QCD at large Q^2 and to search for new physics (such as the top quark, the Higgs boson or supersymmetric particles) in the e^+e^- interactions that take place in the LEP accelerator. The detector was conceived to be as hermetic as possible covering the maximum allowed solid angle and to collect as much information as possible from each event. This chapter describes the ALEPH detector with special emphasis in those parts used in the analysis.

3.1 LEP

The Large Electron Positron storage ring (LEP) [11], is a nearly circular accelerator sited at the European Centre of Nuclear Research (CERN) in Geneva. It is located inside a nearly horizontal tunnel of 26.7 km of circumference, at a depth between 80 and 137 m spanning the French and Swiss territories (figure 3.1). It consists in 8 arcs and 8 straight sections. The beams are formed by bunches of electrons and positrons that circulate inside the beam pipe. They are accelerated in opposite directions and cross in eight or sixteen points in case the number of bunches per beam is four or eight, respectively, although they are steered to collide only in the 4 points where the detectors are installed. The collisions in the other two points are avoided by a system of electrostatic separators.

The accelerator program is comprised of two phases. In the first (current) phase,

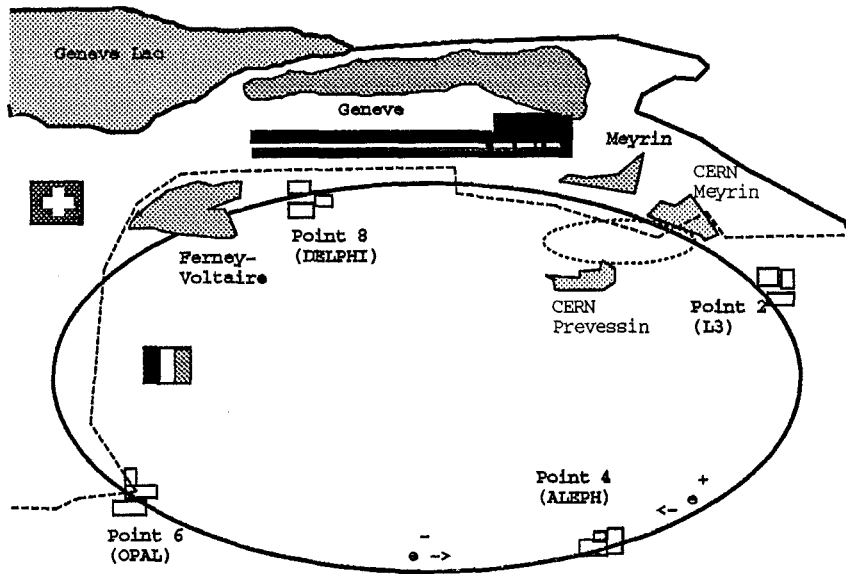


Figure 3.1: The LEP ring.

LEP accelerates, stores and collides electrons and positrons at a centre-of-mass energy around 90 GeV and produces Z bosons with a luminosity (the number of events per time per unit of cross-section) that has been growing every year and that is now above $10^{31} \text{ cm}^{-2} \text{ s}^{-1}$. In the second phase, to start in 1996, an increase of a center-of-mass energy up to 180 GeV would allow the production of W -pairs at a foreseen luminosity of $10^{32} \text{ cm}^{-2} \text{ s}^{-1}$.

The LEP injection chain can be seen in figure 3.2. It consists of the LINear ACcelerator (LINAC) which accelerates electrons and positrons in two stages. The electrons are first accelerated up to 200 MeV. Part of the electrons are used to produce positrons and the rest, together with the positrons are accelerated up to 600 MeV. After the LINAC, the particles are inserted in a small circular e^+e^- accelerator (EPA). From there, they are inserted to the PS accelerator, where the energy is taken up to 3.5 GeV. The particles are injected to the SPS accelerator, rising to an energy of 20 GeV. Finally, they are injected to the LEP main ring and accelerated to a maximum of $\simeq 55$ GeV with a current up to 2.9 mA per beam.

The running and optics configuration of LEP has changed with time trying to reach higher luminosities. While in the first years of operation (from 1989 to Oct

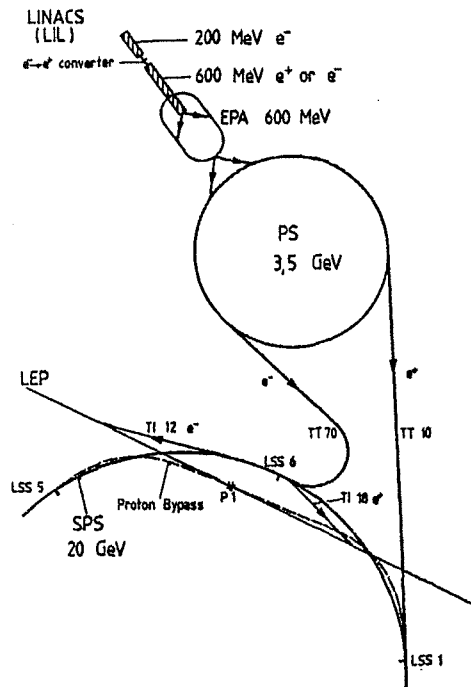


Figure 3.2: Scheme of the LEP injectors and accelerators.

1992), four bunches of electrons were circulating inside the accelerator and were colliding in the interaction points every $22 \mu\text{sec}$, in the 1993 and 1994 running periods, collisions of 8 bunches spaced $11 \mu\text{sec}$ gave a considerable increase in luminosity. For the 1995 running period an scheme of four bunch trains of electrons and positrons consisting of two, three or four equally spaced wagons is expected to produce 50K Z per day in each collision point. Table 3.1 gives the main parameters of LEP.

3.2 The ALEPH detector: general description

The ALEPH detector is located at experimental point number 4 in a cavern of 143 m under the surface. It is a 12 m diameter by 12 m lenght cylinder of positioned around the beam pipe (tube of 10 cm of radius that forms part of the accelerator). In the ALEPH reference system (ARS) the z direction is along the beam line, positive in the direction followed by the e^- , thereby slightly different from the local horizontal due to the small tilt of the accelerator. The positive x direction points to the center

Parameter	Value
Circumference	26667.00m
Average radius	4242.893 m
Bending radius in the dipoles	3096.175 m
Depth	80-130 m
Number of interaction points	4
Number of experimental areas	4
Number of bunches per beam	4-8
RMS Bunch length	11.67 mm
Horizontal bunch sigma	200 μm
Vertical bunch sigma	12 μm
Injection Energy	20 GeV
Maximum beam energy (phase I)	55 GeV
RF Frequency	353 MHz
Total current per beam	0.029 A
Luminosity	$10^{31} \text{cm}^{-2} \text{s}^{-1}$
Vertical β_V^*	5 cm
Horizontal β_H^*	$25 \times \beta_V^*$ cm

Table 3.1: Main LEP parameters.

of LEP, and is horizontal by definition. The positive y direction is orthogonal to z and x and deviates 3.5875 mrad from the local vertical up.

The detector consist of subdetectors, each of one specialized in a diferent task. The tracking devices allow to reconstruct the trajectories of charged particles and to clasify them using the ionization left in the detectors. The electromagnetic and hadronic calorimeters give a measurement of the energy of the particles, being also the only detectors capable to give positional information for the neutral particles. Muons are identified using the muon chambers or the final planes of the hadronic calorimeter. Specialized detectors situated at low angle serve to give a precise measurement of the luminosity. Some other subdetectors are specialized in monitoring tasks. Finally, the trigger and data acquisition system is used to manage everything and record the useful information. A brief description of these devices follows.

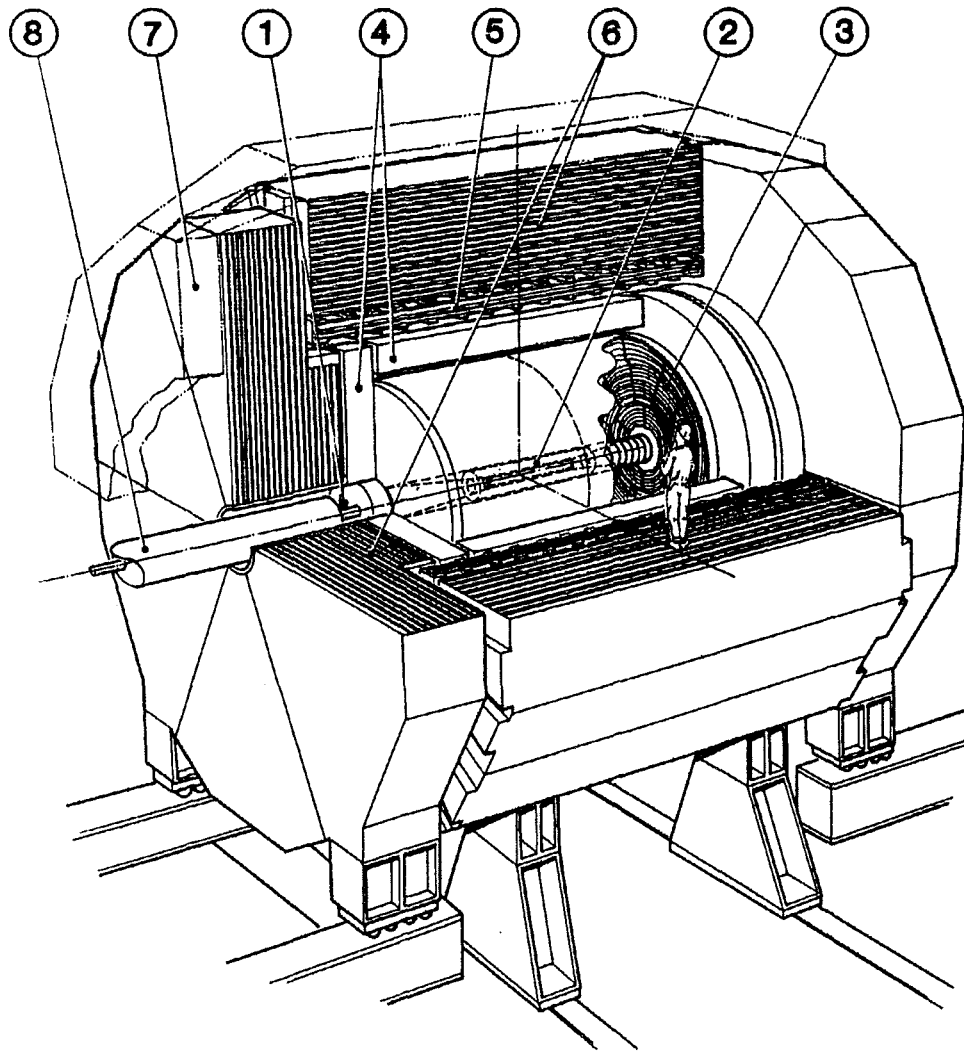


Figure 3.3: Schematic view of the ALEPH detector. (1) Luminosity Monitor. (2) Inner Tracking Chamber. (3) Time Proportional Chamber. (4) Electromagnetic Calorimeter. (5) Superconducting Coil. (6) Hadronic Calorimeter. (7) Muon Chambers. (8) Beam Pipe.

Main detectors

A particle leaving the interaction point would encounter the following subdetectors (figure 3.3):

- The Mini Vertex DETector (VDET), fully operational since end 1991, is a double sided silicon strip device with two layers of strips parallel (z) and perpendicular ($r\phi$) to the beam, situated around the beam pipe, providing a

very accurate vertex tagging of tracks coming from the interaction point. The coordinate spatial resolution is $10\,\mu\text{m}$ in $r\phi$ and $13\,\mu\text{m}$ in z .

- The Inner Tracking Chamber (ITC) is a cylindrical multiwire drift chamber. It contributes to the global ALEPH tracking and is also used for triggering of charged particles coming from the interaction region. It can provide up to eight precise $r\phi$ coordinates per track, with an accuracy of $100\,\mu\text{m}$ per coordinate.
- The Time Projection Chamber (TPC), the central track detector of ALEPH, is a very large three-dimensional imaging drift chamber. It provides up to 27 three dimensional coordinate points of each track. The single-coordinate resolutions are $173\,\mu\text{m}$ in the azimuthal direction and $740\,\mu\text{m}$ in the longitudinal direction. From the curvature of the tracks in the magnetic field, the TPC gives a measurement of transverse particle momenta p_t with an accuracy of $\Delta p_t/p_t^2 = 0.6 \cdot 10^{-3} (\text{GeV}/c)^{-1}$ at 45 GeV if it is used together with the ITC and the VDET. The chamber also contributes to particle identification through measurements of energy loss (dE/dx) derived from about 340 samples of the ionization for a track traversing the full radial range.
- The Electromagnetic CALorimeter (ECAL) is a sampling calorimeter consisting of alternating lead sheets and proportional wire chambers read out in projective towers to obtain a very high granularity (about $1^\circ \times 1^\circ$). It measures the energy and position of electromagnetic showers. The high position and energy resolutions achieved lead to good electron identification and allow to measure photon energy even in the vicinity of hadrons.
- The superconducting coil is a liquid-Helium cooled superconducting solenoid creating, together with the iron yoke, a 1.5 T magnetic field in the central detector.
- The Hadronic CALorimeter (HCAL) is a sampling calorimeter made of layers of iron and streamer tubes. It measures energy and position for hadronic showers and, complemented with the muon chambers, acts as a muon filter. The readout is performed twice: using cathode pads forming projective towers and using digital readout of the streamer tubes for muon tracking and also

for triggering. It also provides the main support of ALEPH, the large iron structure serving both as hadron absorber and as return yoke of the magnet.

- The MUON chambers (MUON), outside HCAL, are two double layers of limited streamer tubes which measure position coordinates of the muons, only detectable particles reaching this subdetector.

Luminosity and beam monitoring

An accurate luminosity measurement is required for the precise measurement of cross-sections. This is provided by four detectors for small angle Bhabha scattering installed around the beam pipe:

- The Luminosity CALorimeter (LCAL), is a lead/wire calorimeter similar to the ECAL in its operation. It consists of two pairs of semi-circular modules placed around the beam pipe at each end of the detector.
- The Silicon luminosity CALorimeter (SICAL) was installed in September 1992 on each side of the interaction region. It uses 12 silicon/tungsten layers to sample the showers produced by small angle Bhabhas. It improves the statistical precision of the luminosity measurement by sampling at smaller angles than LCAL. The systematic error of the luminosity is also reduced thanks mainly to the greater precision in the positioning of its components.
- The very small Bhabha CALorimeter (BCAL) located behind the final focus quadrupoles, is used to give a measurement of the instantaneous and specific luminosity and also as a background monitor. It is a sampling calorimeter made of tungsten converter sheets sandwiched with sampling layers of plastic scintillator. A single plane of vertical silicon strips is used to locate the shower position.

The optimization of LEP performance needs also some monitoring of the beam conditions which is accomplished by:

- The Small Angle Monitor of the Background (SAMBA) is positioned in front of the LCAL at either end of the detector. It consists of two multi-wire proportional chambers at each end, read out in two rings of 8 pads per ring. It is used as a background monitor.

- The Beam Orbit Monitors (BOMs), located around the circumference of LEP, measure the mean position and angle of the beam orbits which are used by LEP to optimize the beam conditions, and by ALEPH to determine the (x, y) position of the beam spot as a starting point for offline reconstruction of the primary vertex.

Trigger system

Not all the collisions that take place at LEP are useful for the physics that ALEPH is willing to study. The large amount of non-useful events have to be filtered out in order to avoid inefficiencies in the detector and a large amount of unused data. For example, if an event is decided to be recorded, it takes up to $45\mu\text{sec}$ for the ionization electrons to reach the end-plates of the TPC and the electromagnetic calorimeter takes up to $61\mu\text{sec}$ to be cleared and ready for the next event. Since three bunch crossings are made in this time, this operation must be performed only when the event will be useful, otherwise large inefficiencies would be introduced. The purpose of the trigger system is to produce a signal that starts the readout of the events. It is desirable to keep all the electron-positron collisions and to reduce as much as possible the rate of background events. The trigger system has been organized in a three-level scheme:

- **Level one** decides whether or not to read out all the detector elements. Its purpose is to operate the TPC at a suitable rate. The decision is taken approximately $5\mu\text{s}$ after the beam crossing from pad and wire information from the ECAL and HCAL and hit patterns from the ITC. The level one rate must not exceed a few hundred Hz. If the decision is not to take the event, the TPC is resetted and kept ready for the next event.
- **Level two** refines the level one charged track trigger using the TPC tracking information. If level one decision cannot be confirmed, the readout process is stopped and cleared. The decision is taken approximately $50\mu\text{s}$ after the beam crossing (the time at which the TPC tracking information is available). The maximum trigger rate allowed for level two is about 10 Hz.
- **Level three** is performed by software. It has access to the information from all detector components and is used to reject background, mainly from beam-

gas interactions and off-momentum beam particles. It ensures a reduction of the trigger rate to 1–2 Hz, which is acceptable for data storage.

This trigger scheme has to be rather flexible since it has to be able to reject the background and keep signals from possible new physics events. Therefore the available electronic signals from different ALEPH detector components allow for a variety of triggers which, together, cover all possible types of events.

Data Acquisition System and Event Reconstruction

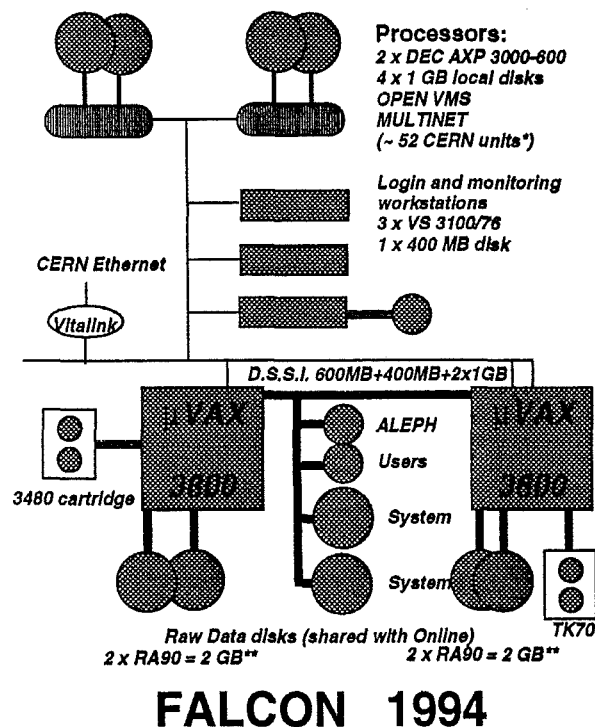
The data acquisition system allows each subdetector to take data independently. The DAQ [12] architecture is highly hierarchical. Following the data and/or control flow from the bunch crossing of the accelerator down to storage device, the components found and its tasks are briefly described below:

- Timing, Trigger and Main Trigger Supervisor: synchronize the readout electronics to the accelerator and inform the ReadOut Controllers (ROCs) about the availability of the data.
- ROCs: initialize the front-end modules, read them out and format the data.
- Event Builders (EBs): build a subevent at the level of each subdetector and provide a ‘spy event’ to a subdetector computer.
- Main Event Builder (MEB): collects the pieces of an event from the various EBs and ensures resynchronization and completeness.
- Level three trigger: as seen, performs a refined data reduction.
- Main host and subdetector computers: The main machine (a VAX-AXPCluster) initializes the complete system, collects all data for storage and provides the common services. The subdetector computers get the ‘spy events’ and perform the monitoring of the large subdetectors (TPC, ECAL, HCAL).

The data taken by the ONLINE computers is called raw data and is reconstructed quasy online. In less than two hours after the data is taken, the reconstruction

and a check of the quality of it is done, thus allowing ALEPH to have a fast cross-check of it and correct possible detector problems. This task is performed by the Facility for ALEPH Computing and Networking (FALCON) [13].

The year by year continuous increase of CPU power of the machines has made the hardware and software of FALCON develop in order to accommodate to the available performance and requirements.



(*) has to be tested with ALEPH programs, JULIA etc..
 (**) one or two disks might be changed to 800 MB.

Figure 3.4: Schematic representation of the FALCON cluster.

In its actual configuration consists of three processors (three AXP machines with a total power of $\simeq 60$ CERN units¹) Each of the processors runs the full ALEPH reconstruction program JULIA (Job to Understand Lep Interactions in ALEPH) [14] which, for each event of the raw data file, processes all the information from the different subdetectors. Other programs also run to compute the drift velocity

¹A CERN unit is equivalent to an IBM 168 CPU unit, approximately 1/6 of an IBM 3090 processor or about 1.2 Mflops.

in the TPC (PASS0), or to analyze the quality of the data taken (RunQuality).

After their reconstruction, the events are written in POT (Production Output Tape) data files and transmitted to the CERN computer center where they are converted into different data types more suitable for physics analysis. The events are ready to be analyzed only a few hours after having been taken.

3.3 Subdetectors relevant to the analysis

The measurement of the scaled energy distributions and the selection of hadronic events necessaries for the analysis need only the use of tracking devices, specially the TPC and the ITC that serve for the measurement azimuthal angle (used in the measurement of the longitudinal and transverse cross-sections) and the momentum of the particles. However, the selection of flavour-tagged samples of events needs the VDET detector and, also the use of the calorimeters.

The main tracking detectors are described in detail in the following sections. Also a description of the electromagnetic and hadronic calorimeters is given, although less detailed due to their more limited importance for the analysis.

3.3.1 The Mini Vertex Detector

The VDET is formed from 96 silicon wafers each of dimension $(5.12 \times 5.12 \times 0.03)$ cm arranged in two coaxial cylinders around the beam pipe. The inner layer has nine wafers in azimuth, with average radius of 6.5 cm, and the outer has 15 wafers with average radius of 11.3 cm, both layers being four wafers long. Each wafer has $100 \mu\text{m}$ strip readout both parallel ($r\phi$) and perpendicular (rz) to the beam direction. Particles passing through a wafer deposit ionization energy, which is collected on each side of the wafer.

The advantage of the VDET is that it pinpoints a track's location in space quite near to the beam pipe. VDET hits are used by extrapolating a track found by the ITC and/or the TPC to the VDET and then refitting the track more precisely using VDET hits which are consistent with it. The addition of VDET to the tracking improved the momentum resolution at 45 GeV to $\Delta p_T/p_T^2 = 0.6 \cdot 10^{-3} (\text{GeV}/c)^{-1}$ from $\Delta p_T/p_T^2 = 0.8 \cdot 10^{-3} (\text{GeV}/c)^{-1}$ when only TPC and ITC were used [26].

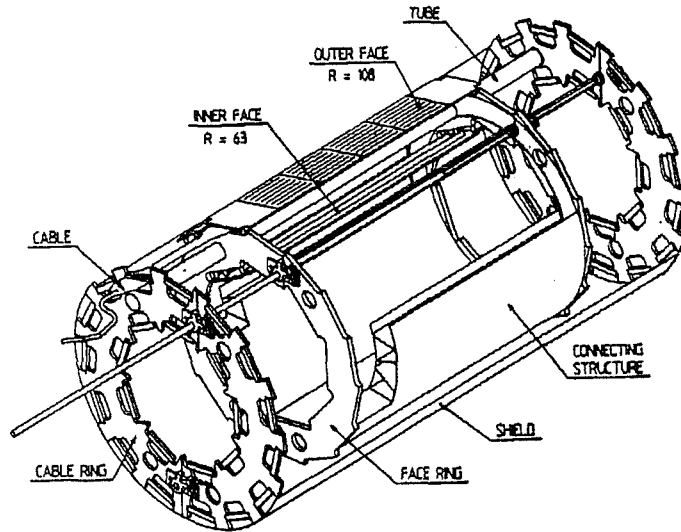


Figure 3.5: Cut-away view of the VDET.

Using VDET, together with the other tracking detectors, the spatial coordinates of the origin of a 45 GeV charged track's helix (impact parameter) can be found to within about $23\text{ }\mu\text{m}$ in the $r\phi$ view and $28\text{ }\mu\text{m}$ in the rz view measured from dimuon events. For lower momentum tracks, this parameter is measured from hadronic Z decays. The resolution on the impact parameter can be parametrized as

$$\sigma(\delta) = 25\text{ }\mu\text{m} + \frac{95\text{ }\mu\text{m}}{p}(\text{GeV}/c)^{-1}. \quad (3.1)$$

This allows tracks produced by decay of short-lived particles to be separated from those at the primary interaction point with good efficiency.

3.3.2 The Inner Tracking Chamber

The Inner Tracking Chamber (ITC) [27] using axial wires made of gold and tungsten provides up to eight $r\phi$ points for tracking in the radial region between 16 and 26 cm. It also provides the only tracking information for the level one trigger system. It is able to identify roughly the number and geometry of tracks, due to its fast response time (the trigger is available within 2–3 μs of a beam crossing) and allows non-interesting events to be quickly rejected.

The ITC is operated with a gas mixture of argon (50%) and ethane (50%) at atmospheric pressure.

The ITC is composed of 8 layers of sensing wires (operated at a positive potential in the range $1.8 - -2.5$ kV) running parallel to the beam direction, located forming hexagonal cells with the central sense wire surrounded by six field wires held at earth potential (figure 3.6). The sense wires detect the ionization of particles passing close by. The measurement of the drift time, gives the measurement of the $r\phi$ coordinate within about $150\ \mu\text{m}$. The z coordinate is found by measuring the difference in arrival times of pulses at the two ends of each sense wire, but with an accuracy of only about 3 cm. The particles with polar angles between 14 and 165 degrees pass through the 8 layers.

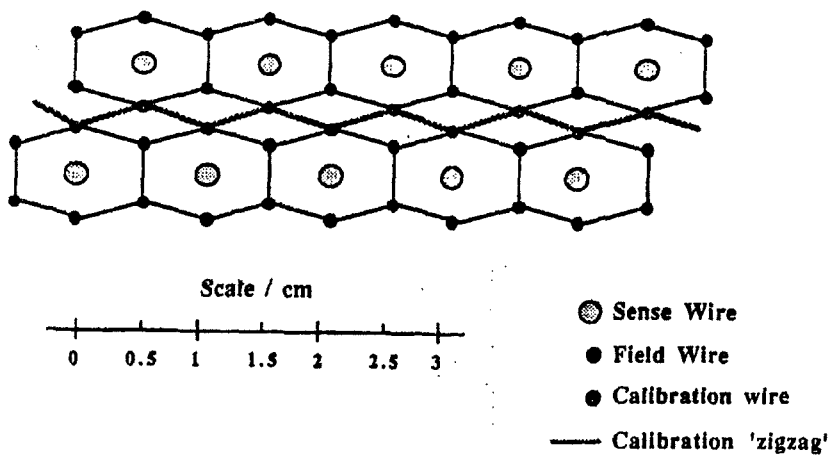


Figure 3.6: The ITC drift cells.

3.3.3 The Time Projection Chamber

The Time Projection Chamber (TPC) [28] was designed to obtain high precision measurements of the track coordinates, to get good momentum resolution and to measure the dE/dx depositions of charged particles.

The time projection chambers use the techniques of the ionization chambers to measure the transverse ($x - y$) coordinates, while measuring the time to detect each ionized bunch of electrons gives the position in the z coordinate. In the case

of ALEPH, the charged particles create ionization in the gas that fills the TPC. The electrons produced in this ionization are driven by an electric field to the end-plates where wire chambers are located. There, a secondary ionization takes places and the position where this happens gives the $r\phi$ coordinate. The time needed for the electrons to reach the end-plate gives the z coordinate. Due to the 1.5 T magnetic field produced by a superconducting solenoid surrounding the TPC whose axis is parallel to the TPC symmetry axis, the trajectory of a charged particle inside the TPC is a helix, and its projection onto the end-plate is an arc of a circle. By measuring the sagitta of this arc, one obtains the curvature radius that is proportional to the modulus of the component of the momentum perpendicular to \vec{B} .

The TPC has a cylindrical structure of 4.4 m long and with 35 cm and 180 cm of inner and outer radius, respectively (figure 3.7). Its volume is delimited by two coaxial cylinders which hold the end-plates. The dimensions were designed to reach 10% resolution in transverse momentum for the highest possible momenta (muon pairs produced at the LEP energy of 100 GeV per beam). The resolution Δp_t in transverse momentum p_t (GeV/c) is proportional to the resolution in the measurement of the sagitta Δs (mm),

$$\frac{\Delta p_t}{p_t} = 0.027 p_t \frac{\Delta s}{l^2 B} \quad (3.2)$$

where B (T) is the modulus of the magnetic field and l (m) is the length of the projected trajectory. This was optimized by choosing the largest practical lever arm $l = R_{max} - R_{min} \simeq 1.4$ m.

The device is divided into two half-detectors by a membrane which is situated in the plane perpendicular to the axis and midway between the end planes. This central membrane is held at a negative high voltage (-26 kV) and the end-plates are at a potential near ground. The curved cylindrical surfaces are covered with electrodes held at potentials such that the electric field in the chamber volume is uniform and parallel to the cylinder axis.

The TPC volume is filled with a nonflammable gas so that traversing particles will ionize it producing electrons that will be drifted towards one end-plate by the electric field of 110 V/cm. The argon(91%) + methane(9%) gas mixture was chosen because with this mixture is possible to reach high $\omega\tau$ values (ω = cyclotron

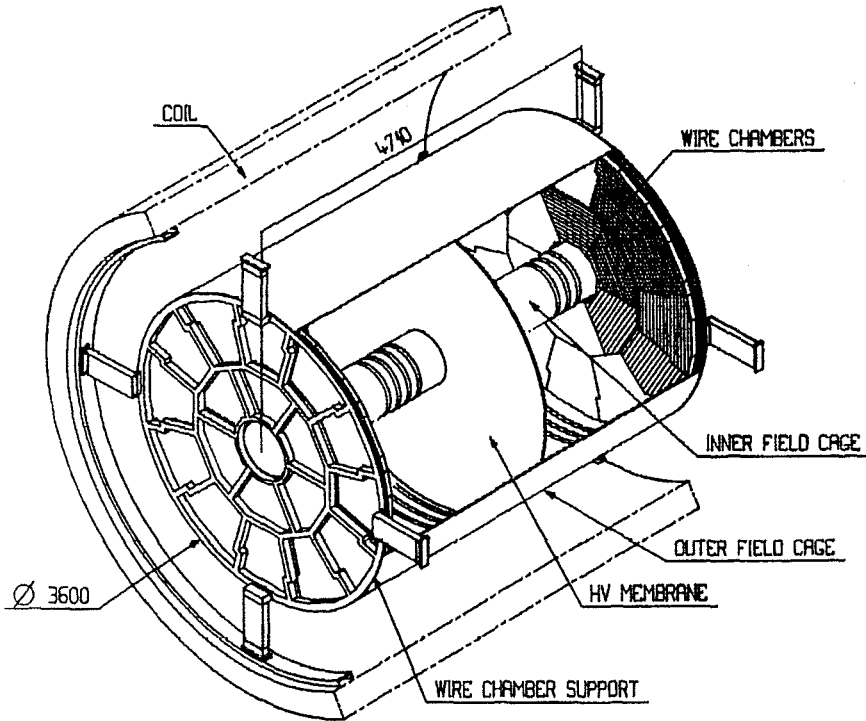


Figure 3.7: Scheme of the TPC.

frequency; τ = mean collision time of the drifting electrons). This causes the electrons to drift mainly along the magnetic field lines and thereby reduces the systematic displacements due to the electric field inhomogeneities.

The electrons produced by the ionization are amplified in the proportional wire chambers positioned in the end-plates. There are 18 wire chambers ('sectors') on each end-plate. In each end-plate, there are six sectors of type K (Kind), surrounded by a ring of alternating sectors of type M(Mann) and W(Weib). In order to get a minimum loss of tracks at boundaries, the sectors are arranged in the 'zig-zag' geometry that can be seen in figure 3.8 in order to get a minimum loss of tracks at boundaries. The gaps between the sectors must be as small as possible. High precision in the alignment of each chamber with the others is also required because each radial track is measured by 2 different wire chambers.

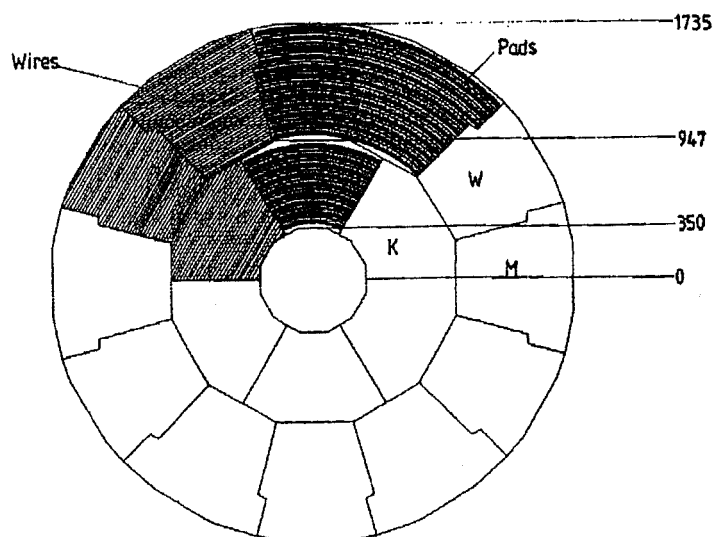


Figure 3.8: View of a TPC end-plate.

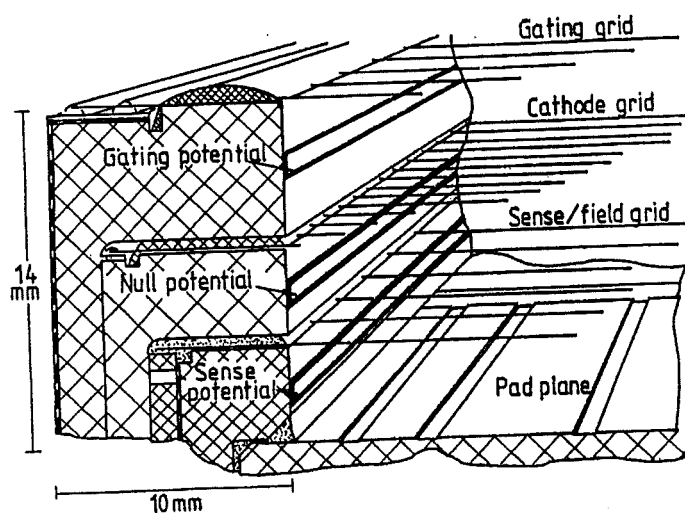


Figure 3.9: View of a TPC wire chamber.

The wire chambers consist on three layers of wires (figure 3.9):

- The gating grid [29] prevents positive ions produced in the avalanches near the

sense wires from entering the main volume of the TPC, distorting the electric field. Potentials of $V_g \pm \Delta V_g$ ($V_g \simeq -67$ V) are placed on alternative wires of the grid. A ΔV_g of 150 V was chosen to block both the passage of positive ions to the drifting volume of the chambers and the incoming electrons in the wire region. The gate is opened $3 \mu\text{s}$ before every beam crossing. If a positive trigger signal arrives, the gate is kept open, otherwise the gate is closed after $\sim 5 \mu\text{s}$.

- The cathode wires keep the end-plates at null potential and together with the central membrane create the electric drift field.
- The sense wires are read out to give the energy deposition (dE/dx) [30] for particle identification and the z measurement of the tracks. For the estimation of the dE/dx a truncated mean algorithm is used, taking the mean of the 60% smaller pulses associated with a track. The achieved resolution is 4.6% for electrons in hadronic events (slightly better for low multiplicity events).

The field wires are kept at null potential to create equipotential surfaces around the sense wires.

The ionization avalanches created around the sense wires are read out by the signal induced on cathode pads at a distance of 4 mm from the sense wires. The pads are connected to preamplifiers via wires passing through the structure which supports the wire grids.

3.3.4 The Electromagnetic and Hadronic Calorimeters

The Electromagnetic [33] and hadronic [?] calorimeters consist both of a barrel and two end-caps located around the TPC. While the Electromagnetic calorimeter is placed inside the coil, the hadronic calorimeter is placed outside, which makes it to be also the return of the magnetic flux of the magnet (figure 3.10).

Both are sampling calorimeters where the main active material is gas. Their barrels and end-caps are divided into modules of 30° in azimuthal angle ϕ . These modules have a small rotation angle between them to avoid cracks in all the calorimeter system. The modules of the end-caps are also rotated with respect to the ones in the barrels.

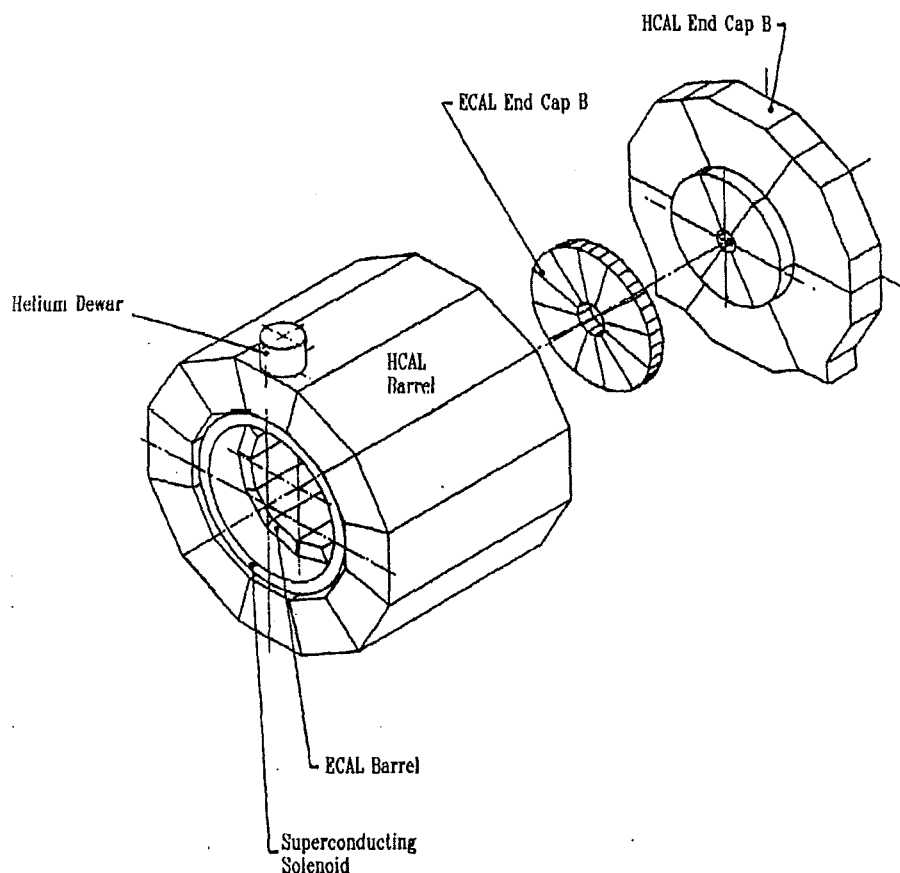


Figure 3.10: Overall view of the Electromagnetic and Hadronic calorimeters.

The barrels are 4.8 m and 6.3 m long for the ECAL and HCAL respectively. The ECAL extends from an inner radius of 1.85 m to an outer radius of 2.25 m and the HCAL from 3 m to 4.68 m.

The modules of the electromagnetic calorimeter, with a total thickness of 22 radiation lengths, consist of 45 layers of lead and wire chambers full with 80% Xenon and 20% CO_2 gas. The structure of a single layer consists (figure 3.11) of a lead sheet, a wire chamber plane (anode plane) made of open-sided aluminium extrusions and a pad plane (cathode plane) covered by a graphited mylar sheet.

The cathode pads are connected internally forming towers which point to the

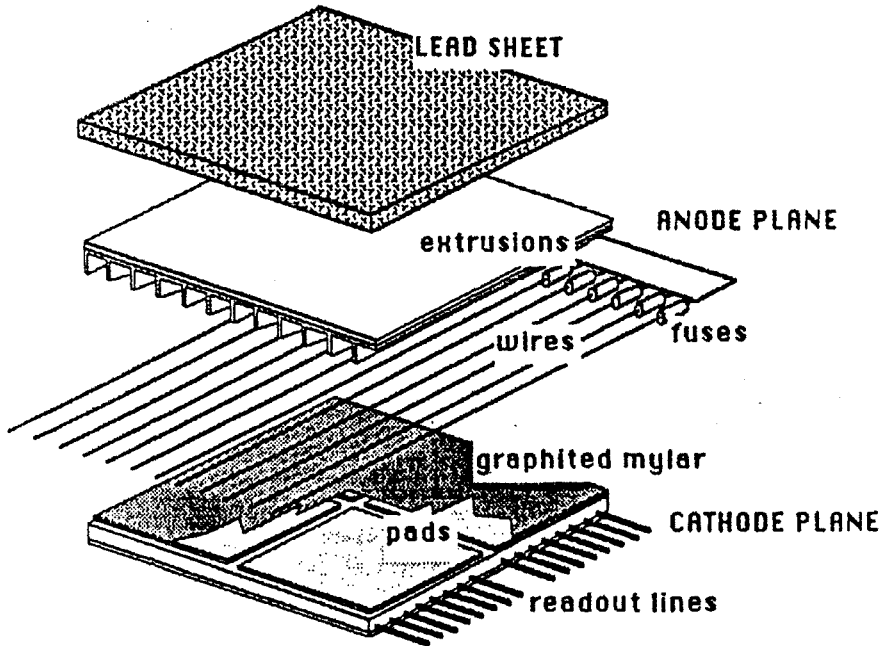


Figure 3.11: View of an ECAL stack layer.

interaction point. Each tower is read out in three sections in depth ('storeys'). The size of the pads is approximately $30 \times 30 \text{ mm}^2$ leading to a high granularity (73728 towers). In addition to the signal of the pads, an analog signal is also available from each anode wire plane. These signals are used for testing and calibrating the modules and also for triggering.

The achieved energy resolution for electrons and photons is

$$\frac{\sigma(E)}{E} = \frac{0.178}{\sqrt{E/\text{GeV}}} \oplus 0.019 \quad (3.3)$$

and the angular resolution for charged tracks with $|\cos \theta_{\text{track}}| < 0.98$ is

$$\sigma_{\theta, \phi} = \left(\frac{2.5}{\sqrt{E/\text{GeV}}} + 0.25 \right) \text{mrad} \quad (3.4)$$

The hadronic modules have 22 iron sheets, each one with a width of 5 cm and an external plane of 10 cm, with a total amount of iron of 1.20 m (7.16 interaction lengths), which is enough to contain the hadronic showers at LEP energies. Between

the iron sheets, there are modules of streamer tubes filled with a mixture of Argon (21%), CO₂ (42%) and n-pentane (37%).

Three different kinds of signals are read out in the hadronic calorimeter: Signals from the pads situated outside the modules containing the streamer tubes, which are used to measure the energy of the showers; signals from the strips situated along the streamer tubes modules, which give the pattern of the streamer tubes in the event and are used as a 'tracking' of the showers and; the signal from the wires, which measure the energy released in the planes and is used mainly for triggering.

The energy resolution is given by:

$$\frac{\sigma_E}{E} = \frac{0.85}{\sqrt{E/\text{GeV}}} \quad (3.5)$$

Chapter 4

Event reconstruction and simulation

4.1 Tracking in ALEPH

Before any measurement of the momentum and track parameters are performed, the raw data coming from the tracking detectors has to be processed and track coordinates have to be measured in order to join them together to finally form a track helix. The next subsections describe the coordinate finding of the three subdetectors and the track reconstruction from them

4.1.1 Coordinate finding

TPC The TPC measures the ionization induced by a charged particle traversing the gas volume of the chamber. The cloud of charge is projected onto the TPC end-plates (by the electric field) and is measured by the sense wires and the pads. The information coming from both is grouped in hits, which contain the pad or wire number, the pulse length and the arrival time of each pulse, and digitizations, that contain pulse-height samples, ie. the details of the pulse shapes [34].

The pad hit-data are grouped into two-dimensional clusters; starting with one pulse, another pulse on an adjacent pad is included if it overlaps the first by at least one sample. In order to separate, or at least recognize, within each cluster the contributions coming from different particles, all clusters are analysed again, this time with the digitization information considered. Peaks that are sufficiently

isolated from others form subpulses. For each subpulse, both a charge estimate and a time estimate are made from digitizations. These estimates are used by the coordinate algorithms. For each good subcluster a three dimensional coordinate is calculated and errors are determined from the widths, in space and time, of the subcluster. The $r\phi$ coordinates are calculated by using a Gaussian model of the pad response if only a few pads are involved, or simply by taking a charge-weighted average of the positions if many pads are involved. The z -coordinate is always determined from a charged weighted average of time estimates of the individual subpulses. All coordinates are corrected for misalignment and distortions of the drift field.

The efficiency of the coordinate finding has been estimated with MonteCarlo events and is 92% for particles above 500 MeV and 75% for those with momentum between 100 and 200 MeV. It should be noticed that the signals in the end-plates are ~ 1.5 cm in $r\phi$ and ~ 2 cm in z . Thus, there are cases in which the clusters belong to more than one track. However, the probability that two tracks overlap all their clusters is small.

The $r\phi$ spatial resolution depends on the diffusion (which is dependent of the drift distance), the alignment of the electric and magnetic fields, the localization of the avalanche in the sense wire, the angle to the track with respect to the pad and of electronic noise and errors in the calibration. An overall resolution $\sigma_{r\phi} = 173 \mu\text{m}$ is measured. The resolution in the z coordinate is $\sigma_z = 740 \mu\text{m}$.

ITC The ITC also produces three dimensional coordinates from the raw data consisting on the wire (channel) number, and the TDC valued in $r\phi$ and z .

The z coordinate is reconstructed from the z digitization using an equation which relates the digitization value to the time difference (Δt) of the signals, originating from a pulse at z , arriving at the two ends of the wire.

To obtain the nominal $r\phi$ coordinate the wire number is used. The $r\phi$ TDC value is used to calculate the drift-time. The relationship between the drift-time and the distance is not linear. The drift-time value is used to generate two coordinates one on each side, azimuthally, of the anode wire. The proper location of the coordinate (and its ambiguity) can only be obtained at the tracking stage when the angle of the track through the drift cell is known.

The $r\phi$ resolution depends on the drift time, the error being worse close to both anode and field wires than in between. The resolution is parametrised as a parabola in azimuthal drift-distance with the minimum of approximately $100\ \mu\text{m}$ (occurring mid-way between the anode and field wires).

VDET The raw data of the Vertex Detector contain the list of channels (and its pulse-height) in the event with a signal above a defined threshold and the seven channels of each side of it.

4.1.2 Track Reconstruction

Once all the coordinates have been found, the tracking [35], [36] is done starting in the TPC by first merging coordinates consistent with an arc of helix less than π radians to form a chain. The chains that are determined to belong to the same helix are linked together into a single track candidate.

Finally, the five helix parameters, as defined in figure 4.1, are determined by a fit of a helix to the pad coordinates within the first half turn of each track candidate. To account for multiple scattering within the fit, the coordinate error estimates are increased in accordance with the distance from the track origin. The fit is allowed to remove outlying coordinates and to break a track between two coordinates if there is evidence from the fit of a particle decay. What results, in the end, is a set of TPC-fitted tracks.

These track candidates are extrapolated to the inner detectors (ITC and VDET) where consistent hits are assigned. First, the TPC track trajectories are projected back into the ITC and a search is made for ITC coordinates around each trajectory. If more than three hits are found a fit is performed and the ITC track is accepted if the fit satisfies a χ^2 cut. Afterwards, the same procedure is performed with VDET hits to associate them to the extrapolated ITC-TPC tracks using a χ^2 discriminator to decide which hit has to be associated to a given track.

Coordinate errors are determined using the preliminary track parameters. The final track fit based on Kalman filter [37] techniques uses these errors and takes into account multiple scattering between each measurement.

The track finding efficiency in the TPC has been studied using Monte Carlo

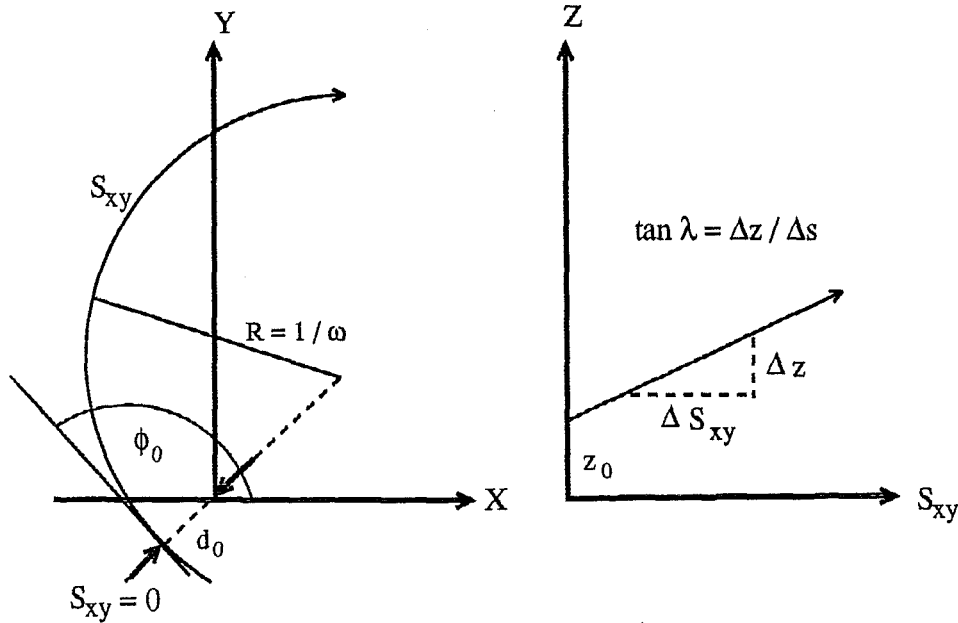


Figure 4.1: Helix parameters used in the TPC tracking programs: ω , inverse radius of curvature; d_0 , distance of closest approach to the z axis; z_0 , z coordinate where d_0 is measured; ϕ_0 , ϕ at closest approach to the z axis, and $\tan \lambda$, tangent of the dip angle.

simulation. In hadronic Z events, 98.6% of tracks that cross at least four pad rows in the TPC are reconstructed successfully; the small inefficiency, due to track overlaps and cracks, is reproduced to better than 10^{-3} by the simulation. The efficiency of associating a vertex detector hit to an isolated track is about 94% per layer, within the geometrical acceptance.

Systematic effects in the tracking parameters come from electric and magnetic field inhomogeneities, unknowns in the small angle between the axes of the electric and magnetic fields or from the systematic errors in the drift velocity. The distortions induced by these effects can be corrected and affect mainly to the tracks parameters related with the position of the tracks.

A transverse momentum resolution of

$$\sigma(1/p_T) = 0.6 \times 10^{-3} (\text{GeV}/c)^{-1} \quad (4.1)$$

is measured (for 45 GeV muons). At low momentum multiple scattering dominates and adds a constant term of 0.005 to $\sigma(p_T)/p_T$.

4.2 Energy and position reconstruction with the calorimeters

To reconstruct the calorimetric energy, the hit storeys are combined to find topologic clusters (a cluster being a group of spatially connected storeys, having at least one corner in common). In the ECAL, the triggered storeys are scanned and the first cluster is created if the energy of the storey is larger than a certain amount ($t_{high} = 90$ MeV). Then the neighbouring storeys are scanned and they are added if their energy is larger than $t_{low} = 30$ MeV. In a similar fashion, in the HCAL, the tower information is also reconstructed in the form of clusters.

To associate clusters with charged tracks, the track is extrapolated step-by-step to the ECAL region. At each step, the ECAL geometry package is used to determine which storeys are intercepted by the track. Then the clustering algorithm is used to determine if the storey, or its neighbours, are hit and to which cluster they belong. A track and a cluster are associated if one point of this track is in one storey of the cluster or in a storey which has at least one corner in common with the cluster.

The position of the showers is calculated by an energy-weighted mean of the position of the individual storeys or towers in the cluster. This is corrected for the usual ‘S-shape’ effect present in all the granular detectors.

The information from the calorimeters is heavily used in the particle identification algorithms giving good electron and muon identification efficiencies and, photon and π^0 reconstruction.

4.3 Energy flow determination

The energy flow algorithm [38] is used in the event-shape algorithm used for the identification of different flavour hadronic events. A description of the algorithm is given in this section.

The simplest way to determine the energy flow of an event recorded in the

ALEPH detector is to make the sum of the raw energy found in all calorimetric cells without performing any particle identification. This method yields a resolution of $\sigma(E)/E = 1.2/\sqrt{E/\text{GeV}}$ for hadronic decays of the Z . The energy flow algorithm developed in ALEPH improves this resolution by making use of track momenta and taking advantage of the photon, electron and muon identification capabilities.

A first cleaning procedure is done to eliminate poorly reconstructed tracks, V0 not compatible to originate from the nominal collision point, and noisy channels and fake energy deposits in the calorimeter towers.

After the cleaning, the charged particle tracks are extrapolated to the calorimeters, and groups of topologically connected tracks and clusters (called ‘calorimeter objects’) are formed. Each calorimeter object is then processed using the following steps.

1. All the charged particle tracks coming from the nominal interaction point or belonging to a reconstructed V^0 , are counted as charged energy assuming they are pions.
2. The charged particle tracks identified as electrons, are removed from the calorimeter object, together with the energy contained in the associated electromagnetic calorimeter towers. If the difference between this calorimeter energy and the track momentum is larger than three times the expected resolution, this difference is assumed to come from a bremsstrahlung photon, and is counted as neutral electromagnetic energy.
3. The charged particle tracks identified as muons, are removed from the calorimeter object, together with a maximum of 1 GeV from the closest associated electromagnetic calorimeter cluster (if any) and a maximum of 400 MeV per plane fired around the extrapolation of the muon track from the corresponding hadron calorimeter cluster.
4. The photons and π^0 's, are counted as neutral electromagnetic energy and are removed from the calorimeter object.
5. At this stage, the only particles left in the calorimeter object should be charged and neutral hadrons. The charged hadron energy has already been determined in the first step, but the neutral hadron energy has not been accounted for.

Although possible in principle via a specific tube pattern recognition, a direct identification of neutral hadrons is difficult and has not yet been attempted for the energy-flow reconstruction. Here, a neutral hadron is identified as a significant excess of calorimetric energy: in a given calorimeter object, the remaining energy left in the calorimeters is summed, after first scaling that from the electromagnetic calorimeter by the ratio of the calorimeter's response to electrons and pions. If this sum exceeds the energy of any remaining charged particle tracks, and the excess is both larger than the expected resolution on that energy when measured in the calorimeters, and greater than 500 MeV, then it is counted as neutral hadronic energy. The ratio of the electromagnetic calorimeter's response to electrons and pions has been determined to be ~ 1.3 with test-beam data. However, in order to account for the fact that low energy photons often escape identification in the preceding step of this analysis, the ratio is modulated according to the penetration of the particle and is taken as 1.0, 1.3 and 1.6 in the first, second and third segments in depth of the calorimeter, respectively.

This is repeated for all the calorimeter objects of the event and results in a set of 'energy-flow objects' (electrons, muons, photons, charged or neutral hadrons), also called particles, characterized by their energies and momenta. To this list are added all the clusters found in the luminosity monitor, where no particle identification is available. This list is expected to be a close representation of the reality, i.e. of the stable particles actually produced by the collision. Since the neutrinos escape undetected, they cannot be in the list but they should be detected indirectly by the presence of missing energy in the event.

The energy-flow resolution can be determined from the data using a sample of selected hadronic events. A Gaussian to the total energy distribution gives a peak value of 90.5 GeV (62 % from charged particles, 25 % from photons and 13 % from neutral hadrons), with a resolution of 6.2 GeV. It is well reproduced by a sample of 700,000 fully simulated hadronic events in which a peak value of 90.7 GeV and a resolution of 6.5 GeV are obtained. The jet angular resolution is 18 mrad for the polar angle and 19 mrad for the azimuthal angle.

4.4 flavour tagging algorithms

Two flavour tagging algorithms have been developed in ALEPH. The Impact parameter tag makes use of the relatively long lifetime of hadrons containing a b quark to construct the likelihood of a group of tracks coming from the primary vertex to distinguish between heavy quark events from the light quark ones. The event shape tag makes use of two global properties of the event to make the same classification.

4.4.1 Impact parameter tag

The long lifetime and large mass of b hadrons give their decay products large impact parameters, allowing a separation of these hadrons from hadrons coming from fragmentation or decay of a light quark. This tagging algorithm computes the probability that a track comes from the primary vertex using the measurement of its impact parameter. The probabilities of coming from the primary vertex of all the tracks from a given jet, hemisphere or event can be combined to finally have the probability that the given object (jet, hemisphere or event) comes from a b quark.

The main tool in the analysis is, then, the impact parameter of a track. The measurement of this quantity needs, however, a precise estimation of the e^+e^- interaction vertex for each event which needs also the estimation of the overlap region of the electron and positron beams (beam spot) where it lies on. The description of each of these measurements follows:

Beam spot measurement. The position of the beam spot is determined by studying the distance of closest approach of tracks to the coordinate origin in the $r\phi$ plane, d_0 . This quantity is signed according to the sign of the angular momentum component of the track along the beam axis, and in the absence of track distortions, should have a distribution centered on zero. If the beam spot is not centered on the coordinate origin, the mean value of d_0 has a sinusoidal dependence on the azimuthal angle ϕ . This dependence can be seen looking at the relation

$$d_b = d_0 - x_b \sin \phi + y_b \cos \phi - d_{\text{off}} \quad (4.2)$$

which can be deduced from figure 4.2. d_b is the distance of closest approach of tracks to the beam spot, x_b and y_b are the coordinates of the beam position and d_{off}

is an additional offset that takes into account residual tracking effects (alignment errors, field parametrization, etc.).

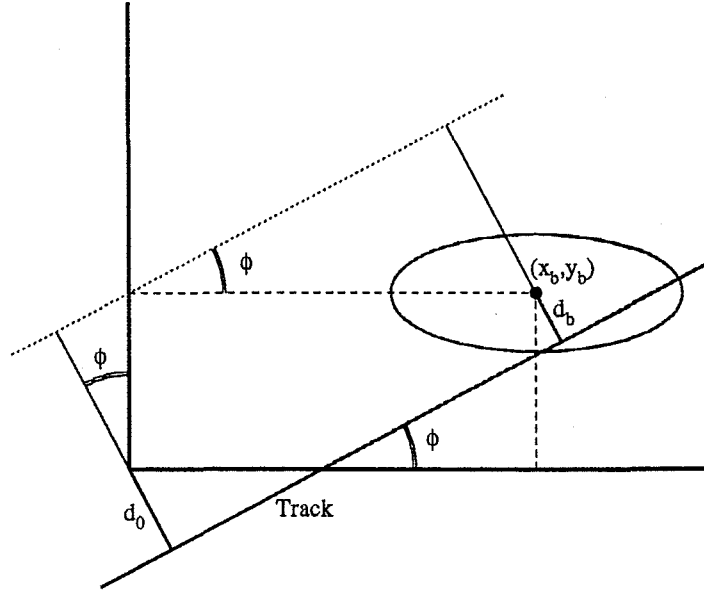


Figure 4.2: Impact parameter with respect to the coordinate origin and with respect to the beam spot centroid.

The mean of d_b for each ϕ is zero. Thus, the fit to the dependence of $\langle d_0 \rangle$ as function of the angle ϕ gives the coordinates of the luminous region as well as the value of d_{off} .

Since there are variations in the crossing beam coordinates even inside the same fill, this measurement is done every ~ 100 events. For the optics of the LEP machine, the beam spot is expected to be elliptical in shape in the plane perpendicular to the beam direction, with the horizontal width much greater than the vertical due to synchrotron radiation effects. The predicted dimensions are $\sigma_H = 200 \mu\text{m}$ and $\sigma_V = 12 \mu\text{m}$, respectively (table 3.1).

Event crossing point measurement. For each event, the measurement of the three coordinates of the collision point is needed. To perform this, the event is clustered in jets using the E clustering scheme with a true mass metric (look at what it is or reference...) using the energy flow objects with a $y_{\text{cut}} = 0.02$. All tracks

satisfying minimal quality cuts are assigned to the nearest jet and then projected into the plane perpendicular to its corresponding jet. The primary vertex in the plane of each jet is then found. Knowing the direction of each, the projected primary vertexes are expanded back in three dimensions and all jets are added together with the beam spot information in the X-Y plane. This way ensures that the hadron lifetime does not bias the position of the primary vertex introducing correlations in the tagging algorithm.

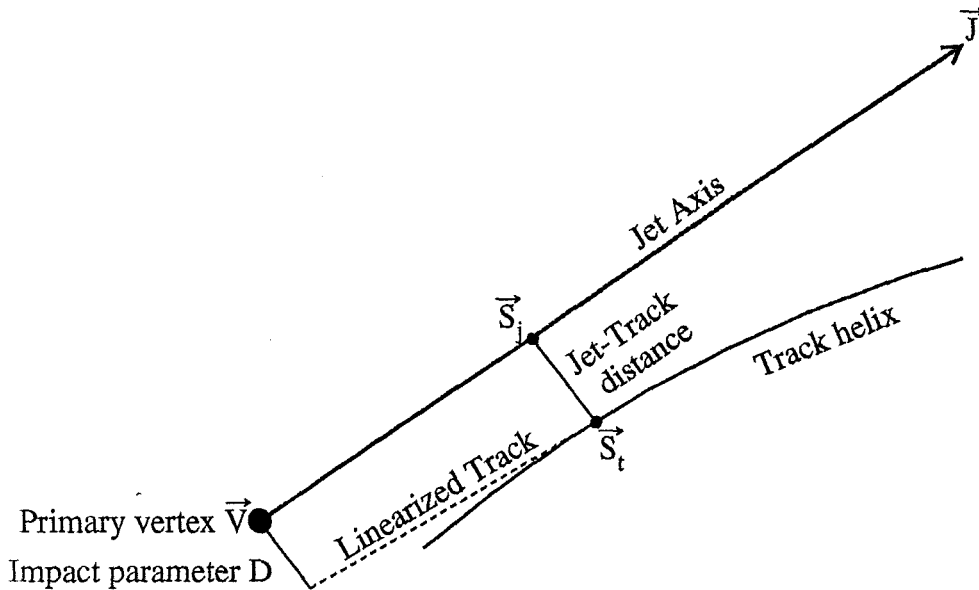


Figure 4.3: Definition of the signed impact parameter. See text for details.

Track impact parameter measurement. The impact parameter of a track is defined as the closest approach of the track to the production point of the mother particle of the track. The method to measure this parameter is described in figure 4.3. The point \vec{V} is the primary vertex. \vec{J} is the direction of the mother particle momentum, as approximated by the jet direction. The circular arc represents a track, assumed here to be a decay product. Point \vec{S}_t is the point on the track where it comes closest to the line going through \vec{V} with direction \vec{J} . The point \vec{S}_t is used as an approximation to the decay point of the track. The track is linearized at \vec{S}_t , and the signed impact parameter is defined as

$$\tilde{D} \equiv \text{sign}(\vec{S}_t - \vec{V}) \cdot \vec{J} \cdot D, \quad (4.3)$$

being a positive number with value D if the vector $\vec{S}_j - \vec{V}$ lies in the same direction as the jet direction \vec{J} , negative otherwise.

The experimental resolution generates a random sign for tracks which originate from the primary vertex. The negative tracks form a control sample that can be used to measure the resolution.

In the tagging algorithm, the statistical significance of the impact parameter of the tracks, defined as \tilde{D}/σ_D , is used. The uncertainty in D , σ_D , is computed from the error matrices from the track and primary vertex, plus their correlations. Since the error of the track is highly dependent on its angle, the number of VDET hits and the planes of the VDET that it traverses, this allows to treat all the tracks nearly uniformly for all the angles and number of VDET hits.

The probability that a track comes from the primary vertex is then defined as

$$P_T(\tilde{D}/\sigma_D) = \int_{-\infty}^{-|\tilde{D}/\sigma_D|} dx \mathcal{R}(x), \quad (4.4)$$

being $\mathcal{R}(\tilde{D}/\sigma_D)$, the resolution function, the parametrization of the distribution of the impact parameter significance for tracks with negative value of \tilde{D} .

The same argument can be extended to a group of tracks forming a jet, an hemisphere or an event. The variable to compute, P_N , is the probability that any set of N tracks without lifetime produce the same set of observed probabilities or any other set of values equally or more unlikely. Being P_T the individual track probabilities, the differential probability for the observed set of variables to happen is given by

$$\Pi \equiv \prod_{i=1}^N P_{T_i}. \quad (4.5)$$

Considering that all the individual track probabilities belong to a N -dimensional space, P_N can be computed as

$$\begin{aligned} P_N &= \int_{(0,0,\dots,0)}^{\prod_{i=1}^N x_i=\Pi} dx_1 dx_2 \dots dx_N \\ &= 1 - \int_{\prod_{i=1}^N x_i=\Pi}^{(1,1,\dots,1)} dx_1 dx_2 \dots dx_N \\ &= 1 - \int_{\Pi}^1 \int_{\Pi/x_N}^1 \int_{\Pi/(x_N x_{N-1})}^1 \dots \int_{\Pi/(\prod_{i=2}^N x_i)}^1 dx_1 dx_2 \dots dx_N, \end{aligned} \quad (4.6)$$

which working out the mathematics, gives

$$P_N = \Pi \cdot \sum_{j=0}^{N-1} \frac{(-\ln \Pi)^j}{j!} \quad (4.7)$$

and represents the likelihood for the group of tracks of coming from the primary vertex.

4.4.2 Event shape tag

Events produced by the fragmentation of a b quark are expected to have different shape than the ones coming from light quarks or c quarks. In general, jets produced by a b fragmentation and decay are expected to have a larger opening angle due to the higher mass of the b hadron and the fact that they can decay to a charmed hadron that would decay afterwards to lighter hadrons, thereby randomizing the directions of the final particles. This can be used to classify different quark flavours.

Considering all the energy flow objects computed according to the algorithm explained in section ??, the thrust axis of the whole event, defined as the vector \vec{T} which minimizes the thrust value defined as

$$T = \frac{\sum_{i=1}^n |\vec{T} \cdot \vec{p}_i|}{\sum_{i=1}^n |\vec{p}_i|}, \quad (4.8)$$

where \vec{p}_i is the momentum of the i th particle, is defined. The event is divided in two hemispheres according to the plane perpendicular to thrust axis and another thrust axis is computed for each hemisphere. In order to avoid correlations among hemispheres, only particles forming an angle less than 45° are used. The selected particles are boosted into the rest frame of each hemisphere before computing the two variables used: the *moment of inertia* and the *lateral mass*.

The moment of inertia is defined as the minimum eigenvalue normalized to the sum of the three eigenvalues of the inertial matrix which is computed according to

$$\lambda_{ij} = \sum_{m=1}^n \frac{-p_m^i p_m^j}{|\mathbf{p}_m|} \quad (4.9)$$

and

$$\lambda_{kk} = \sum_{m=1}^n \frac{(p_m^i)^2 + (p_m^j)^2}{|\mathbf{p}_m|}, \quad k \neq i, j \quad (4.10)$$

where p_m^i is the i th component of the boosted momentum vector of the m th particle. The total momentum in the centre of mass frame of the b jets tends to be more uniformly distributed than the ones for lighter quark jets. Thus, b jets look more spherical and the three eigenvalues of the inertial matrix tend to be equal. In this case the moment of inertia tends to its maximum value of $1/3$.

The lateral mass is intended to distinguish between products of gluon bremsstrahlung and decay products in the final state based on the direction relative to the boost of the jet. It is defined as the sum of the boosted momenta of those particles in the hemisphere that make an angle with the hemisphere axis smaller than $\cos^{-1}(0.75)$. The distribution of lateral mass for hemispheres produced from a b quark is peaked at higher values than for the other flavours.

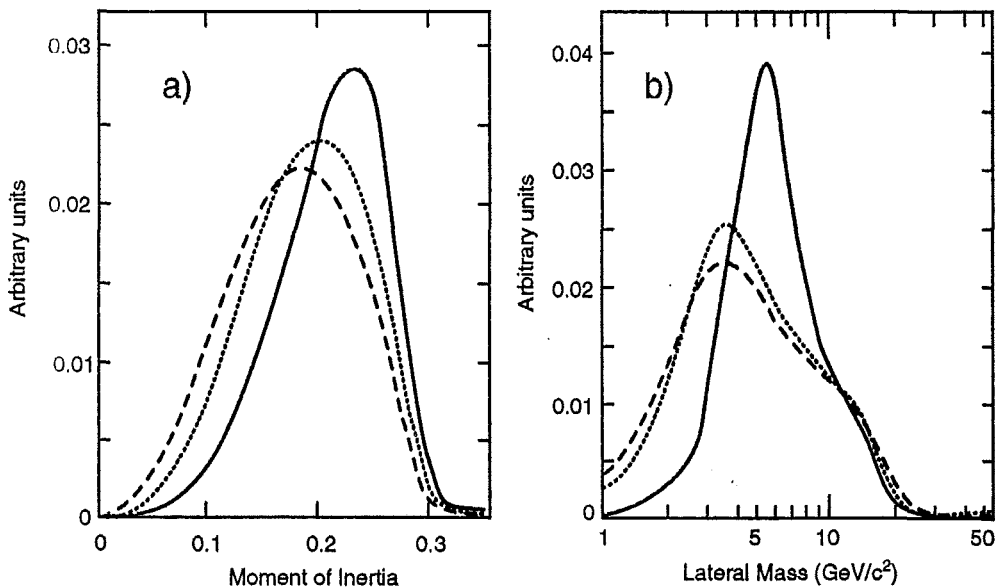


Figure 4.4: Distributions of quantities used in the two variable hemisphere method. (a) lateral mass variable, (b) moment of inertia variable, for different Monte Carlo events: b solid line, c dotted, uds dashed. (All curves are normalized to have the same area).

Figure 4.4 shows the distribution for the Moment of inertia and the lateral mass for the different flavours. Using Monte Carlo, the likelihood that an hemisphere with a given moment of inertia and lateral mass comes from a $Z \rightarrow b\bar{b}$ event l_h , is computed and this is the estimator used in the tag.

4.5 The Event Simulation

The different physics analyses use Monte Carlo simulated events to evaluate background contaminations, compute acceptances and efficiencies and, in general, compare theoretical models to the experimental results. These simulated events have exactly the same format that the real data events, so the same reconstruction process is performed in it. The chain to produce them is as follows:

- Generation of the event kinematics. The different particle four-momenta are generated according to the different physics processes (in parentheses the names of the computer programs used).
 - $e^+e^- \rightarrow \mu^+\mu^-$ (KORALZ [15]).
 - $e^+e^- \rightarrow \tau^+\tau^-$ (KORALZ).
 - $e^+e^- \rightarrow e^+e^-$ (BABAMC [16]).
 - $e^+e^- \rightarrow q\bar{q}$ (LUND [17] + DYMU[18]).
 - $e^+e^- \rightarrow \ell^+\ell^-(\ell^+\ell^-)$ (PHOPHO [19], [20]).

In ALEPH, all these programs have been unified through the common interface KINGAL [21].

- Simulation of the detector. This is done using a GEANT [22] based program (GALEPH [23]) where all the information about the geometry and materials involved in the experimental setup are described. For the tracking simulation, the primary long-lived particles are followed through the detector. Secondary particles are also produced by interaction with the detector materials. Bremsstrahlung, Compton and ionization are some of the processes simulated. GEANT and GHEISHA [24] are used to simulate the electromagnetic and nuclear interactions respectively. Digitization or simulation of the detector behaviour. The energy depositions are converted to measurable electrical signals. The complexity of the TPC required the development of a special package (TPCSIM) for its tracking and digitization. Also, a simulation of the trigger with the same conditions as the real one is implemented.

Chapter 5

Data used in the analysis

This chapter describes the data used in the analysis. It is important to have as much information as possible for different flavour-quark samples. Thus, light(uds)-, c- and b-flavour enriched scaled energy distributions are measured besides the scaled energy distribution for all flavours that gives the information to the evolution of the fragmentation functions. The selection, correction and systematics estimates procedures are explained in sections 5.1 and 5.2. The estimation of the correlation errors among all these distributions is explained in section 5.4. Useful information on the gluon fragmentation function is obtained in the analysis of three jet events and the measurement of the longitudinal and transverse scaled energy distributions. These measurements are described in sections 5.5 and 5.6, respectively. Finally, the scaled energy distributions measured at lower energies by other experiments than ALEPH, and the error assumption made in the normalization errors are described in section 5.7.

5.1 Selection of hadronic events

Before any flavour identification, a good selection of hadronic event has to be made. Since the interest is in the scaled energy distribution and the available statistics of around 20 tracks per event is rather high, the interest of the global selection is in avoid possible biases that would result in high correction factors rather than in optimizing the selection efficiency.

For each event, only charged tracks with more than 4 TPC hits, originated in a cylinder of radius $d_0 = 2$ cm and length of $z_0 = 10$ cm, forming an angle with the z

axis, θ , between 20° and 160° , and with a transverse momentum, p_t , with respect to the z axis exceeding $0.2 \text{ GeV}/c$ are considered in the analysis. Tracks passing these requirements are called good tracks. An hadronic event should have more than four of these good tracks and their energy must sum more than 15 GeV .

The sphericity axis, defined as the eigenvector corresponding to the minimum eigenvalue of the tensor

$$S^{ab} = \frac{\sum_i p_i^a p_i^b}{\sum_i p_i^2} \quad (5.1)$$

is computed in the events passing the above selection cuts. Only those events in which the polar angle of the sphericity axis, θ_{sph} lies between 35° or above 135° are accepted. Since the opening angle of a jet is roughly 15° , this cut avoids larger correction factors removing those events that would not be fully contained in the detector acceptance.

A total of 911539 events from 1992 and 1993 LEP run periods with a center of mass energy of... (at peak) fulfil the requirements to be considered hadronic, the selection efficiency being 77%. The background was estimated from Monte Carlo, being the main contribution the one coming from taus (0.3%) and the ones from bhabha and dimuon events being negligible (0.004% and $6.10^{-5}\%$ respectively). No Monte Carlo two photon event passed the selection cuts.

5.2 Scaled energy non-flavour tagged distribution

For each event, the variable $x_E = E_{tr}/E_{beam}$ is computed for each charged good track, with E_{tr} being the energy of the track assuming the pion mass.

The raw data distribution is normalized to the total number of events such that, for each bin

$$\sigma_{i,raw} = \frac{1}{N_{events}} \frac{N_i^{tr}}{\Delta x_i} \quad (5.2)$$

where N_i^{tr} are the number of tracks such that its variable x_E lies within the bin interval and Δx_i is the width for bin i .

The distribution is corrected, using standard Monte Carlo methods, for effects of geometrical acceptance, detector efficiency and resolution, decays, secondary interactions, initial state photon radiation and mass of the particles.

To perform the correction, hadronic events were generated using the generators HVFL03 and HVFL04 [?]. The events generated with HVFL03 were used for the simulation of the 1992 geometry and efficiency. The 1993 data was simulated with the HVFL04 Monte Carlo. The main differences between them comes in the update of heavy flavour branching ratios and differences in the modeling of the hadronic decays of b hadrons. Initial state radiation is included in the simulation. The generated events were passed through the detector simulation program. The same procedure was performed for τ , Bhabhas, dimuon and two photon events using KORAL0Z [?] and BHABHA [] as generators. The same selection and analysis procedure was performed for the simulated data and distributions $\sigma_{i,sim}$ containing the hadronic events and all the background sources, were constructed.

Hadronic events were also generated using the HVFL03 and HVFL04 generators with neither initial state radiation nor detector simulation and with the requirement that all particles with mean lifetimes $> 10^{-9}$ s are stable. All charged particles were used to construct the $\sigma_{i,gen}$ distribution were, in the computation of x_E , the true mass of the particles is used to compute the energy.

Corrected data distributions were obtained using the bin-by-bin ration of the generated and simulated distributions according to

$$\sigma_{i,corr} = C_i \sigma_{i,raw} = \frac{\sigma_{i,gen}}{\sigma_{i,sim}} \sigma_{i,raw}. \quad (5.3)$$

The distributions were corrected separately for 1992 and 1993 data taking periods to take into account the proper detector configuration for each year. Afterwards, both corrected distributions were combined.

Althouth this correction can induce a small bias towards the model, the fact that the simulated and raw data agree and that the correction factors are relatively small indicate that this bias is not large. Figure 5.1(a) shows the correction factors, C_i , applied to the all flavour distribution. They are arround 7% or bellow in almost the whole interval, except the bins at larger momentum. This is due to the TPC momentum smearing. The reconstructed momentum error in the TPC is nearly gaussian in the inverse of the momentum. Thus, the momentum track distribution can be given

$$\frac{dn}{dp} = \frac{1}{p^2} \exp \left(-\frac{1/p - \langle 1/p \rangle}{\sigma_{1/p}} \right)^2, \quad (5.4)$$

which has non gaussian tail at large momentum. This causes particles above ~ 30 GeV to be more probably measured at higher momentum than at lower one. Since the scaled energy distribution is falls off rather steeply there are more particles at low momentum that then to populate the high momentum bins. This makes the correction factor in the last bins to be even above 20%.

Figure 5.1(b) shows the corrected scaled energy distribution for the normal flavour composition. The continuous lines show the same distribution constructed with different Monte Carlo models. The differences between the corrected data and the different models can be seen in more detail in figure 5.1(c) where the quantity $(\text{Model} - \text{Data})/\text{Error}_{\text{data}}$, being $\text{Error}_{\text{data}}$ the total statistical and systematic error of the distribution, is plotted for the different models. While the HVFL Monte Carlo, which is the one used in the correction procedure maintains a difference bellow three sigmas in the whole energy range, the rest of models disagree up to eight sigmas in, specially in the high energy range. The reason for this should be looked for in the better paramter tuning of the HVFL Monte Carlo, specially in the heavy flavour hadron decay branching fractions.

Systematic uncertainties due to: (a) possible discrepancies between the real and the simulated detector performance and, (b) due to the QCD generator chosen to calculate the correction factor were taken into account.

To estimate the uncertainties of the first kind, all the selection cuts were varied, once at a time, taking alternatively the values listed in table 5.2 and the same correction and combination procedure was used to produce analogous corrected distributions for each set of cuts. In each bin, the maximum change with respect to the standard set of cuts corrected distribution was taken as the systematic error. Figure 5.2 shows these differences in number of statistical standard deviations of the reference distribution. The maximum variation comes from accepting events with four good tracks, were a large τ contamination enters and from the change in the cuts in the angle of the sphericity axis. Most of the differences are below one standard deviation showing the robustness of the selection criteria.

To estimate the systematic uncertainties coming from the QCD generator chosen, a simplified method wich does not use the full detector simulation performance, was applied. Five million events were generated using the ARIADNE [?], NLLJET [?] and JETSET PS[?] generators. HERWIG [?] was not used in this procedure

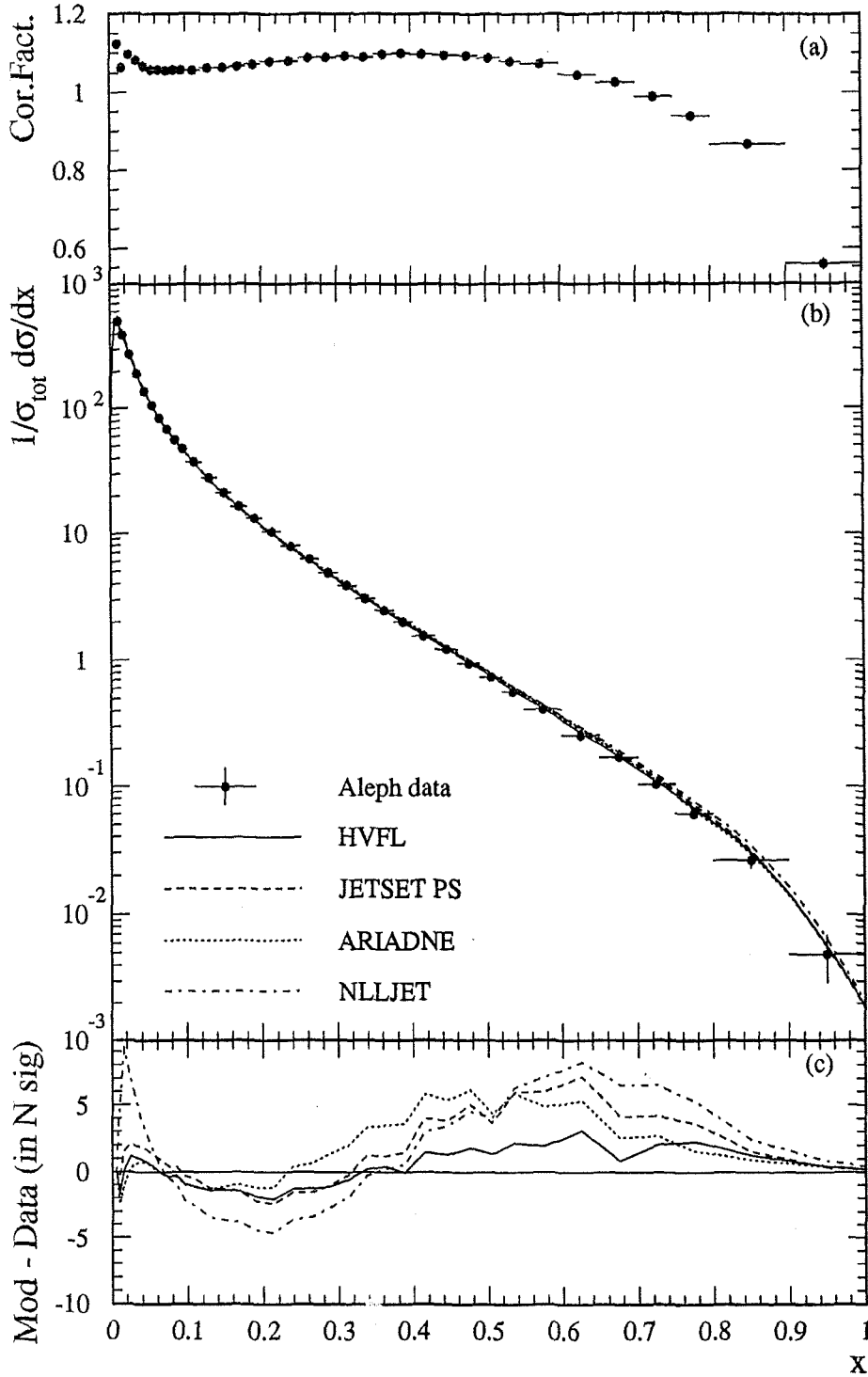


Figure 5.1: Correction factors applied to the all-flavour inclusive energy distribution(a), corrected distribution and comparison with different MonteCarlo models (b), and deviation of the models from the corrected data measured in number of standard deviations, where the error includes statistical and systematical sources (c).

Standard cut	Variation 1	Variation 2
$N_{\text{TPC}} \geq 4$	$N_{\text{TPC}} \geq 3$	$N_{\text{TPC}} \geq 5$
$d_0 \leq 2.0$ cm	$d_0 \leq 1.5$ cm	$d_0 \leq 3.0$ cm
$z_0 \leq 5.0$ cm	$z_0 \leq 3.0$ cm	$z_0 \leq 10.0$ cm
$20^\circ \leq \theta_{\text{track}} \leq 160^\circ$	$30^\circ \leq \theta_{\text{track}} \leq 150^\circ$	$15^\circ \leq \theta_{\text{track}} \leq 165^\circ$
$p_t \geq 200$ MeV	$p_t \geq 150$ MeV	$p_t \geq 400$ MeV
$N_{\text{good}} \geq 5$	$N_{\text{good}} \geq 4$	$N_{\text{good}} \geq 7$
$E_{\text{Ch}} \geq 15$ GeV	$E_{\text{Ch}} \geq 10$ GeV	$E_{\text{Ch}} \geq 25$ GeV
$35^\circ \leq \theta_{\text{spher}} \leq 145^\circ$	$45^\circ \leq \theta_{\text{spher}} \leq 135^\circ$	$65^\circ \leq \theta_{\text{spher}} \leq 155^\circ$

Table 5.1: Definition of the cuts for the standard analysis and the variation made for the systematics estimation. Each cut was varied at once taking, alternatively, the values in the two columns labelled as *Variation 1* and *Variation 2*, and the analysis was repeated for each combination. The rest of the cuts remain at their standard values.

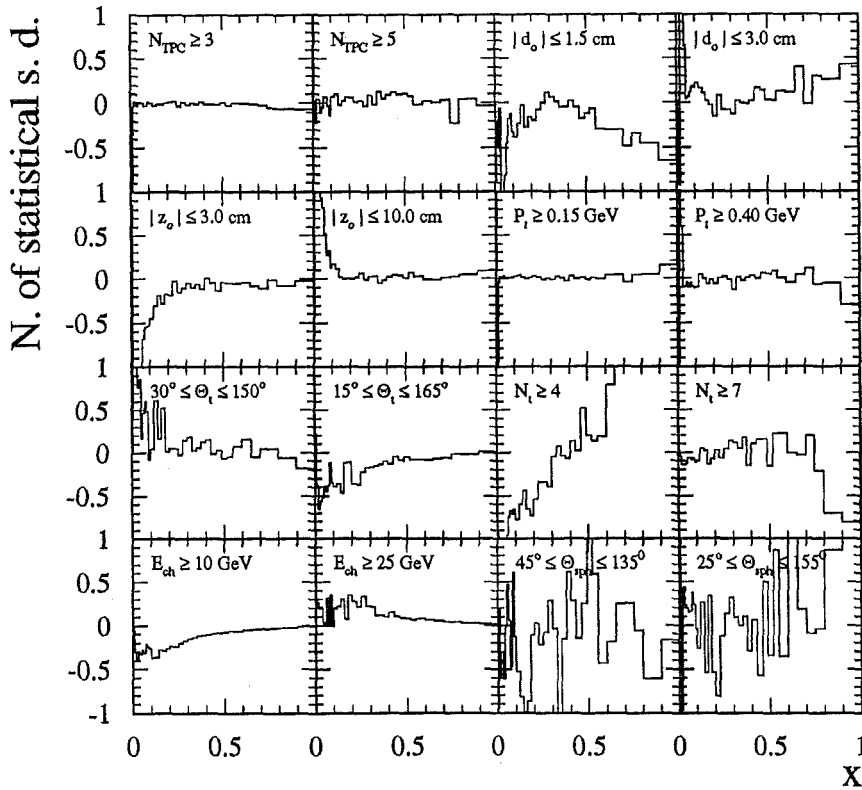


Figure 5.2: Differences between the distribution constructed with the standard selection cuts and the ones varying one of the cuts at a time. This difference is shown in number of statistical standard deviations of the reference distribution.

because the available version (5.6) does not reproduce the angular distribution of the data and the lower versions do not give the correct scale energy distributions. Thus, including it would give an artificial increase in the systematic uncertainties.

Simplified correction factors were computed for each model using the ratio of the generated distribution and the distribution containing tracks and events that fulfill the same selection criteria that for the standard data. The fact that no TPC smearing resolution and efficiency is taken into account in this simulation makes these simplified correction factors to be rather smaller than the ones coming from the full simulated distributions. Nevertheless, it is expected that when all the detector effects would be included, the differences between the models remain the same and that the maximum relative difference between the simplified correction factors is a good estimation of the systematic errors coming from this QCD model generator dependence.

The statistical error and the systematics coming from the limited statistics of the Monte Carlo used to perform the correction procedure, the selection cut variation and the QCD model dependence were added in quadrature to compute the total bin by bin error of the distribution. A common normalization error, which is correlated, not only in all the bins, but also in all the distributions is also added in quadrature to the total error. Table C in appendix C lists the cross-section and all the error contributions for all the bins.

5.3 Enriched flavour distributions.

Since the distributions for the light quarks (u,d,s) are expected to be almost indistinguishable, three different enriched flavour distributions were prepared: for light, c and b quarks. This section describes the measurement of these enriched flavour distributions two tagging algorithms used to construct them.

To prepare a sample of enriched flavour distribution, the same selection cuts as described in section 5.1 were first applied. The selected events were then divided in two hemispheres separated by the plane perpendicular to the thrust axis. The two flavour tags described in sections 4.4.1 and 4.4.2 were applied to the two hemispheres of the event giving the estimators P_H and l_H , respectively, for each hemisphere.

In order to reduce the bias introduced by the tagging algorithm (which is more

efficient for events with large charged multiplicity) the algorithm is applied only to the tracks of the first hemisphere. If that hemisphere passes the selection cut, the other one is used to measure the charged particle spectrum, weighting each track with a factor of two. Finally, since the two hemispheres are independent, the procedure is repeated with the tag applied to the second hemisphere.

This procedure makes the assumption that the correlations of the tag among hemispheres is small. It can be shown that, for the lifetime tag [?], this correlation is smaller than one per cent for the cut in P_H used in this analysis. In the case of the event shape tags, these correlations are already small by construction, since only particles forming an angle below 45° with the jet axis are used in the variables. Residual correlations between the hemispheres are taken into account in the correction procedure.

The b enriched distributions only make use of the lifetime tag to remove those events with high probability that their tracks come from the primary vertex. The same technique, but accepting only the hemispheres with high P_H is used to construct the uds enriched distributions. For the c enriched distributions, the use of a window cut lifetime tag together with the enhancement of b events produced by the cut in the event shape likelihood, l_H , was necessary to obtain a slightly better c purity that was possible with the lifetime tag alone.

A total of nine distributions were formed using both tags. Table 5.3 shows the cuts applied in the two algorithms to construct them and the flavour composition of each one together with the efficiency of the cut (without including the global $\sim 77\%$ of the hadronic selection) for the flavour that is enriched in each one. Those labeled with 'stand' are the ones that are used in the nominal analysis and the ones with '+' and '-' are more enriched and less enriched distributions to study the systematic errors coming from the tag.

The same systematic error estimation and correction procedure described in section 5.2 was used in the tagged distributions. Systematic effects coming from the possible defects in the simulation of the flavour tag will be taken into account in the α_s measurement but they have not been included in the measurement of the enriched flavour distributions.

The corrections were made using distributions generated with the same flavour composition as the ones resulting applying the different tag algorithms to the Monte

Dist. Name	% uds	% c	% b	Efficiency	Cut definition
uds-enr. (stand)	78.9	14.5	6.6	$\epsilon_{uds} = 74.0$	$P_h \geq 0.3$
uds-enr. (-)	75.0	16.1	8.9	$\epsilon_{uds} = 91.0$	$P_h \geq 0.1$
uds-enr. (+)	82.8	12.5	4.7	$\epsilon_{uds} = 37.8$	$P_h \geq 0.7$
c-enr. (stand)	38.2	35.1	26.7	$\epsilon_c = 9.0$	$0.001 \geq P_h \geq 0.07, l_h \leq 0.2$
c-enr. (-)	41.1	31.5	27.4	$\epsilon_c = 15.9$	$0.0005 \geq P_h \geq 0.12, l_h \leq 0.25$
c-enr. (+)	35.6	36.9	27.5	$\epsilon_c = 6.2$	$0.001 \geq P_h \geq 0.05, l_h \leq 0.18$
b-enr. (stand)	2.2	7.3	90.5	$\epsilon_b = 32.5$	$P_h \leq 0.001$
b-enr. (-)	3.5	9.7	86.8	$\epsilon_b = 39.7$	$P_h \leq 0.003$
b-enr. (+)	0.9	3.9	95.2	$\epsilon_b = 21.3$	$P_h \leq 0.0001$

Table 5.2: Flavour composition of the different distributions considered in the analysis. For each distribution, the flavour composition is shown and the efficiency of selecting those flavour events that want to be enriched. Also the cuts applied to the hemispheres for the lifetime tag (P_h) and the event shape tag (L_h) are shown.

Carlo sample after detector simulation. Figures 5.3, 5.4, 5.5(a) show the correction factors applied in the enriched flavour distribution marked as 'stand' in table 5.3. While they are comparable to the ones shown in figure 5.1(a) corresponding to the all flavours distribution bellow $x \sim 0.6$, differences arise above this limit going from $\sim 15\%$ for the uds enriched flavour distribution (figure 5.5(a)) up to more than 50% for the b enriched flavour distribution (figure 5.3(a)). This effect can be explained again by the TPC momentum esmearing described in section 5.2. The more steeply dropping distribution for the b enriched flavour distribution accentuates the effect while the harder momentum distribution of the lighth quarks gives correction factors even smaller than the all flavour distribution for the large momentum bins.

Figures 5.3, 5.4, 5.5(b) and (c) show the corrected distributions and their comparison with the different Monte Carlo models. The larger discrepancies arise in the b enriched flavour distribution which should be attributed to a lack of branching ratio tuning as was pointed out in section 5.2. The good agreement seen for the c enriched flavour distribution (figure 5.4(c)) should be attributed to the larger errors rather than a better agreement with the Monte Carlo models.

Figure 5.6 shows all scaled energy distributions where the differences between the light and heavy flavour enriched samples can be better appreciated.

Tables C, C, C, in appendix C lists the cross-section and all the error contributions

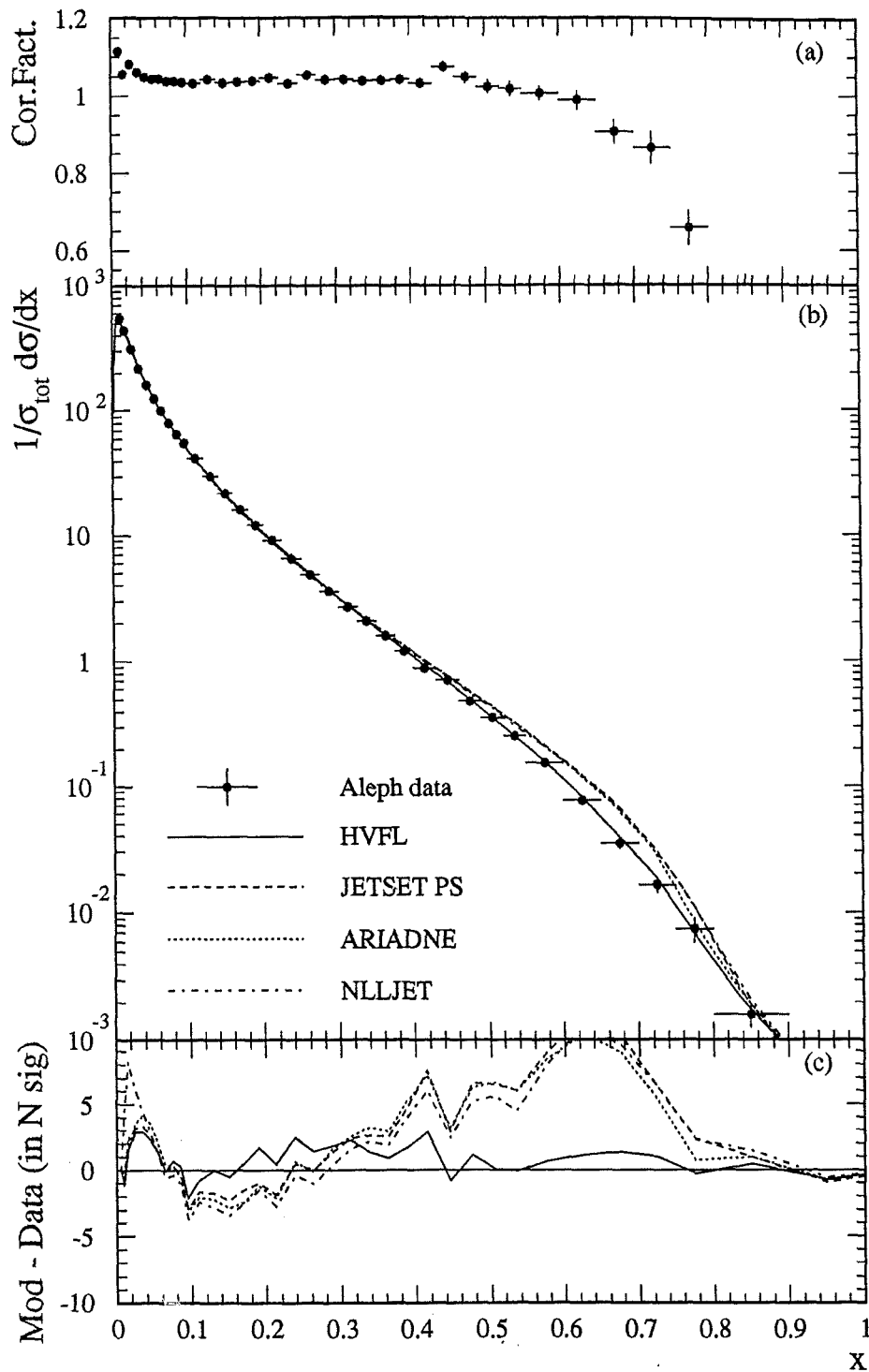


Figure 5.3: Correction factors applied to the b enriched flavour inclusive energy distribution (a), corrected distribution (b) comparing it with different MonteCarlo models and deviation of the models from the corrected data measured in number of standard deviations (including statistical and systematic error) (c).

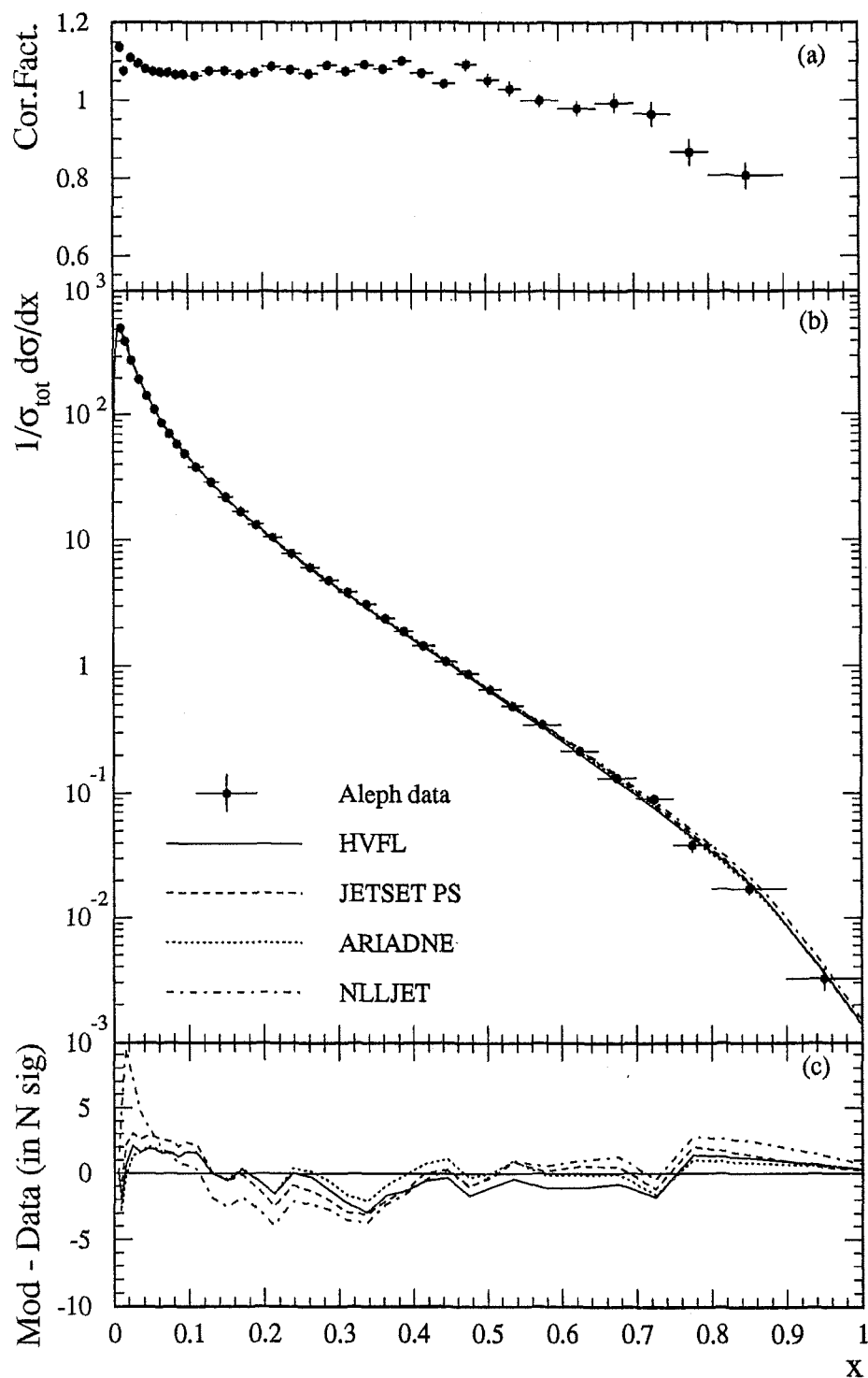


Figure 5.4: Correction factors applied to the c enriched flavour inclusive energy distribution(a), corrected distribution (b) comparing it with different MonteCarlo models and deviation of the models from the corrected data measured in number of standard deviations (including statistical and systematic error) (c).

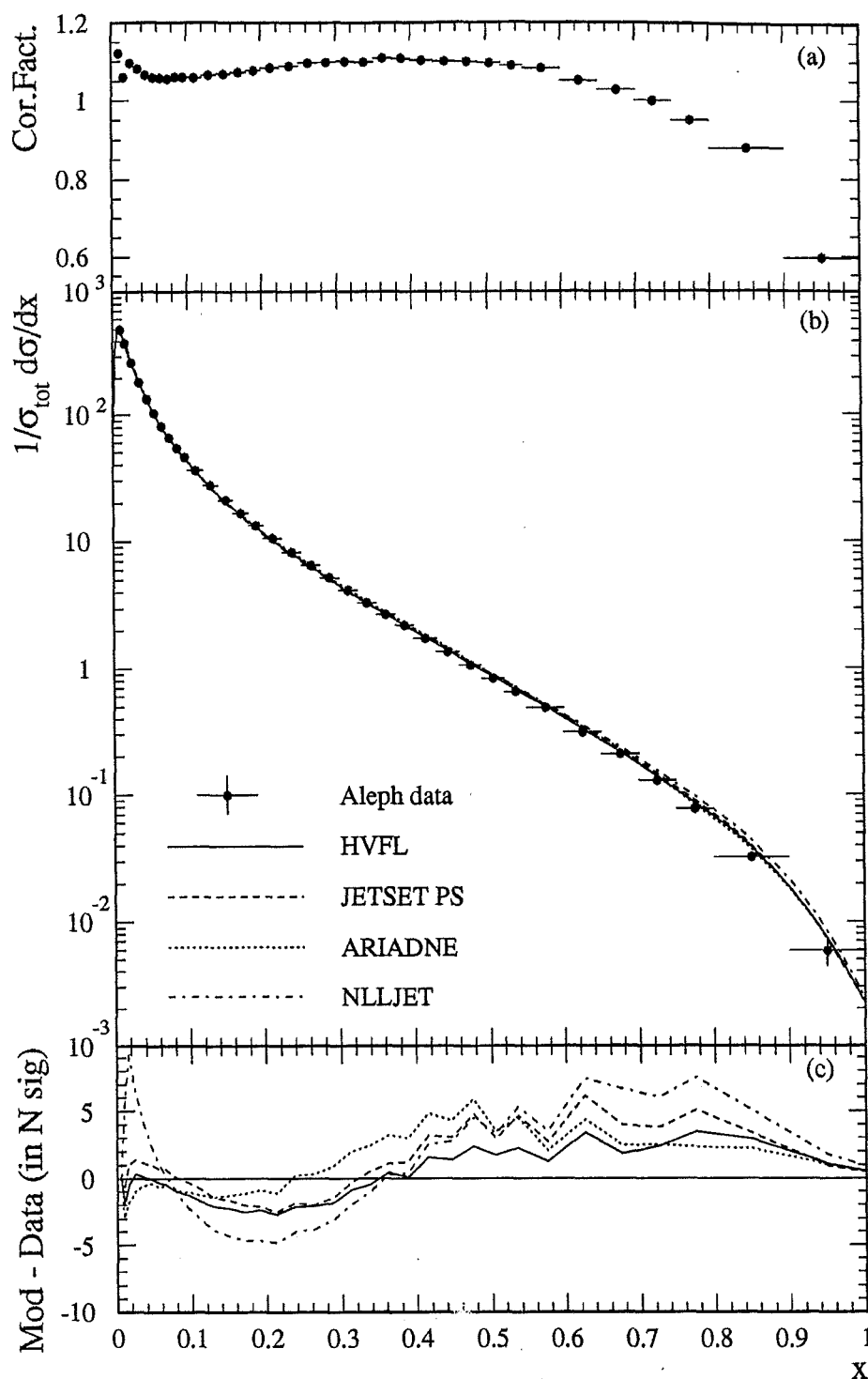


Figure 5.5: Correction factors applied to the uds enriched flavour inclusive energy distribution (a), corrected distribution (b) comparing it with different MonteCarlo models and deviation of the models from the corrected data measured in number of standard deviations (including statistical and systematic error) (c).

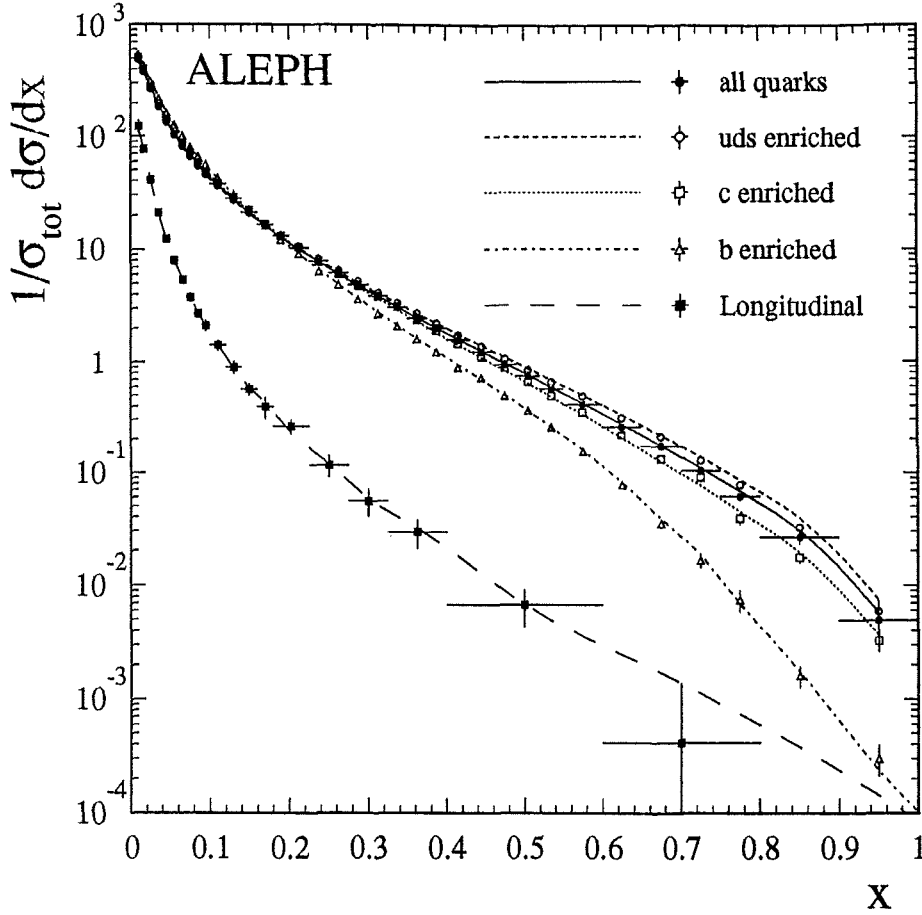


Figure 5.6: Measured scaled-energy distributions corrected for detector effects (symbols) and comparison with the predictions from HVFL. The distributions are normalized to the total number of events. Error bars include statistical and systematics uncertainties. The same binning is used for the inclusive and flavour-tagged distributions.

for all the bins for the standard flavour enriched distributions.

5.4 Correlation between the quark distributions

Apart from the statistical and systematic errors coming from the selection cuts or from the Monte Carlo model used in the detector correction, there exist correlated errors between the bins of all the measured distributions. One affects all the bins of all the measured distributions and it comes from systematic uncertainties in the normalization of the distributions. The other comes from the fact that some tracks

enter more than one distribution.

5.4.1 Normalization errors

The scaled energy distributions are normalized such that the integral of them is the mean number of charged tracks per event. Thus, any uncertainty in the charged multiplicity would affect at all the bins of all the distributions. The study of the charged multiplicity of hadronic events was already performed by ALEPH in [41]. The error in the total charged multiplicity is about 1% and is mainly coming from the uncertainty in the multiplicity of tracks with transverse momentum below 0.2 GeV/c and from the uncertainty in the simulation of accepting tracks from photon conversions.

Any uncertainty of this kind in one bin of one distribution will affect the consecutive bins and also all the bins of all the other distributions since the events taken are the same. Thus, a 1% error has been added in quadrature to all the elements of the covariance matrix formed from all the distributions.

5.4.2 Common-tracks correlations

Since all the tracks that enter in one bin of one of the tagged distributions enter also in the analogous bin of the distribution corresponding to all flavours, there is a statistical correlation between these bins. The cuts used for the flavour enriched distributions have been chosen to be exclusive and the binning is the same in all the distributions. This makes these correlations not to be present between analogous bins of different tagged distributions neither between different bins of the same or other distribution.

Suposing the number of tracks entering bin i in the all flavours distribution is n_i^{tot} and that the number of tracks in a given flavour tagged distribution for the same bin is n_i^{tag} , being $n_i^{tag} < n_i$, the correlation coefficient that should be included in the corresponding element of the covariance matrix is

$$\rho_i^{tot,tag} = \frac{n_i^{tag}}{\sqrt{n_i^{tag}} \sqrt{n_i^{tot}}} = \sqrt{\frac{n_i^{tag}}{n_i^{tot}}}. \quad (5.5)$$

Therefore,

$$\sigma_i^{tot,tag} = \sqrt{\frac{n_i^{tag}}{n_i^{tot}}} \sigma_i^{tot,stat} \sigma_i^{tag,stat} \quad (5.6)$$

was added in quadrature to the appropriate covariance matrix element.

5.5 Three-jet events gluons distribution

The gluon fragmentation function can be extracted directly from the data using three jet symmetric events. These events are characterized by two of the jets having essentially the same energy and the angular separation between any of the two lower energetic jet and the highest energetic jet being in the range $150^\circ \pm 7.5^\circ$.

The most energetic jet has a high probability of originating from a quark or an antiquark. To identify the gluon jet from the two lower energy jets a b anti-tagging method is used. If one of the two jets carries significant impact parameter information associated with a heavy quark jet, it has a high probability of being a b jet. The remaining jet is then tagged as the gluon jet.

Two samples of jets were prepared. In the symmetric S-sample no gluon jet tagging is applied and contains the two lower energetic jets from all the events. This untagged mixture contains $P_g^S = 48.5\%$ of gluons and 51.5% of quarks as computed by Monte Carlo. In the tagged T-sample, only those jets not tagged as coming from a b quark are considered. The gluon purity in this sample is $P_g^T = 90.0\%$.

Any observable, A , can be measured in both samples and extract the measurement for gluons and quarks, A_g and A_q , from the following relations for the S- and T-samples

$$A^S = P_g^S \cdot A_g + (1 - P_g^S) \cdot A_q \quad (5.7)$$

$$A^T = P_g^T \cdot A_g \cdot \delta A_g + (1 - P_g^T) \cdot A_q \cdot \delta A_q \quad (5.8)$$

where $\delta A_{g(q)}$ is a measurement of the bias coming from the fact that the tagged sample is largely enriched in jets coming from b quarks. This bias has to be estimated from Monte Carlo and is given by

$$A_{g(q)} = \frac{A_{g(q)}^{MC,T}}{A_{g(q)}^{MC,S}}, \quad (5.9)$$

where $A_{g(q)}^{MC,T}$ and $A_{g(q)}^{MC,S}$ are the MonteCarlo measurements for correctly identified gluons (quarks) jets in the tagged and symmetric configurations. Further details of the procedure to estimate the purities and the corrections can be found in [42]

The gluon fragmentation function extracted using the technique described above is presented in figure 5.7 and in table ?? in appendix C. The mean energy of the gluon jets is 24 GeV.

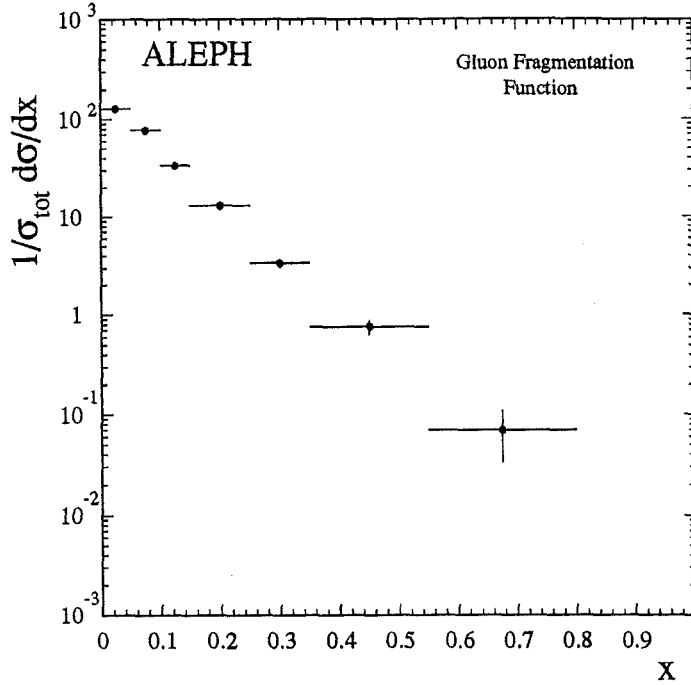


Figure 5.7: Gluon scaled energy distribution measured in three jet symmetric events.

5.6 Transverse and longitudinal distribution

The longitudinal and transverse cross sections defined in equation 2.21 are known to be useful for the extraction of the gluon fragmentation function through equation ???. They can be extracted from the data, either by fitting the angular dependence for each value of x [?], or by weighting each by weighting the double-differential cross section with respect to x and $\cos \theta$ with the appropriate weight to project onto the $(1 + \cos^2 \theta)$ component (transverse) or the $\sin^2 \theta$ component (longitudinal):

$$\frac{d\sigma^{L,T}}{dx} = \int_{-v}^{+v} d\cos \theta W_{L,T}(\cos \theta, v) \frac{d^2\sigma}{dx d\cos \theta} \quad (5.10)$$

with [?]

$$W_L(\cos \theta, v) = [v^2 (5 + 3v^2) - 5 \cos^2 \theta (3 + v^2)] / 4v^5 \quad (5.11)$$

and

$$W_T(\cos \theta, v) = [5 \cos^2 \theta (3 - v^2) - v^2 (5 - 3v^2)] / 2v^5 \quad (5.12)$$

being the longitudinal and transverse projectors, respectively, and v defining the detector acceptance, which is considered to be constant in the range $|\cos \theta| < v = 0.94$.

The event and track selection are the same as described in section 5.1 except that the requirement on the sphericity axis is removed for the measurement of the longitudinal and transverse distributions, because it would introduce an effective strong $\cos \theta$ dependence in the track selection efficiency. Due to lack of statistics in the measurement of the longitudinal distribution, the binning was changed with respect to the other measured distributions.

The selected tracks are then used to construct the inclusive transverse and longitudinal distributions according to

$$\begin{aligned} \frac{1}{\sigma_{tot}} \frac{d\sigma^{L,T}}{dx} &= \left(\sum_{\text{tracks}} W_L(\cos \theta, v) \right) \int_{-v}^v d\cos \theta \frac{d^2\sigma}{dx d\cos \theta} \\ &= \left(\sum_{\text{tracks}} W_L(\cos \theta, v) \right) \frac{3}{4} \left[v + \frac{v^3}{3} + \frac{d\sigma^{T,L}/dx}{d\sigma^{tot}/dx} (v - v^3) \right], \quad (5.13) \end{aligned}$$

where $W_{L,T}(\cos \theta, v)$ are given in equations (5.11) and (5.12). The factor accompanying the sum is not depending on the acceptance cut and the ratio of the longitudinal and total scaled energy distributions for the corresponding bin. However the dependence on the ratio of the distributions is of the order of 1.5% for the values of the distributions measured. Therefore, it was assumed that this dependence would be taken into account in the correction factors and the expression (5.13) was approximated by

$$\frac{1}{\sigma_{tot}} \frac{d\sigma^{L,T}}{dx} = \left(\sum_{\text{tracks}} W_{L,T}(\cos \theta, v) \right) \frac{3}{4} \left[v + \frac{v^3}{3} + \left\langle \frac{d\sigma^L/dx}{d\sigma^{tot}/dx} \right\rangle (v - v^3) \right], \quad (5.14)$$

which, for $v = 0.94$ is ~ 0.915 with small variations with the value of $\left\langle \frac{d\sigma^L/dx}{d\sigma^{tot}/dx} \right\rangle$.

The correction procedure is performed bin by bin in the way described in section 5.2. Figures 5.8 and 5.9 show the correction factors and the comparison with different Monte Carlo models for the transverse and longitudinal scaled energy distribution, respectively. The only significant discrepancy is between ARIADNE and the corrected longitudinal distribution. While the correction factors for the

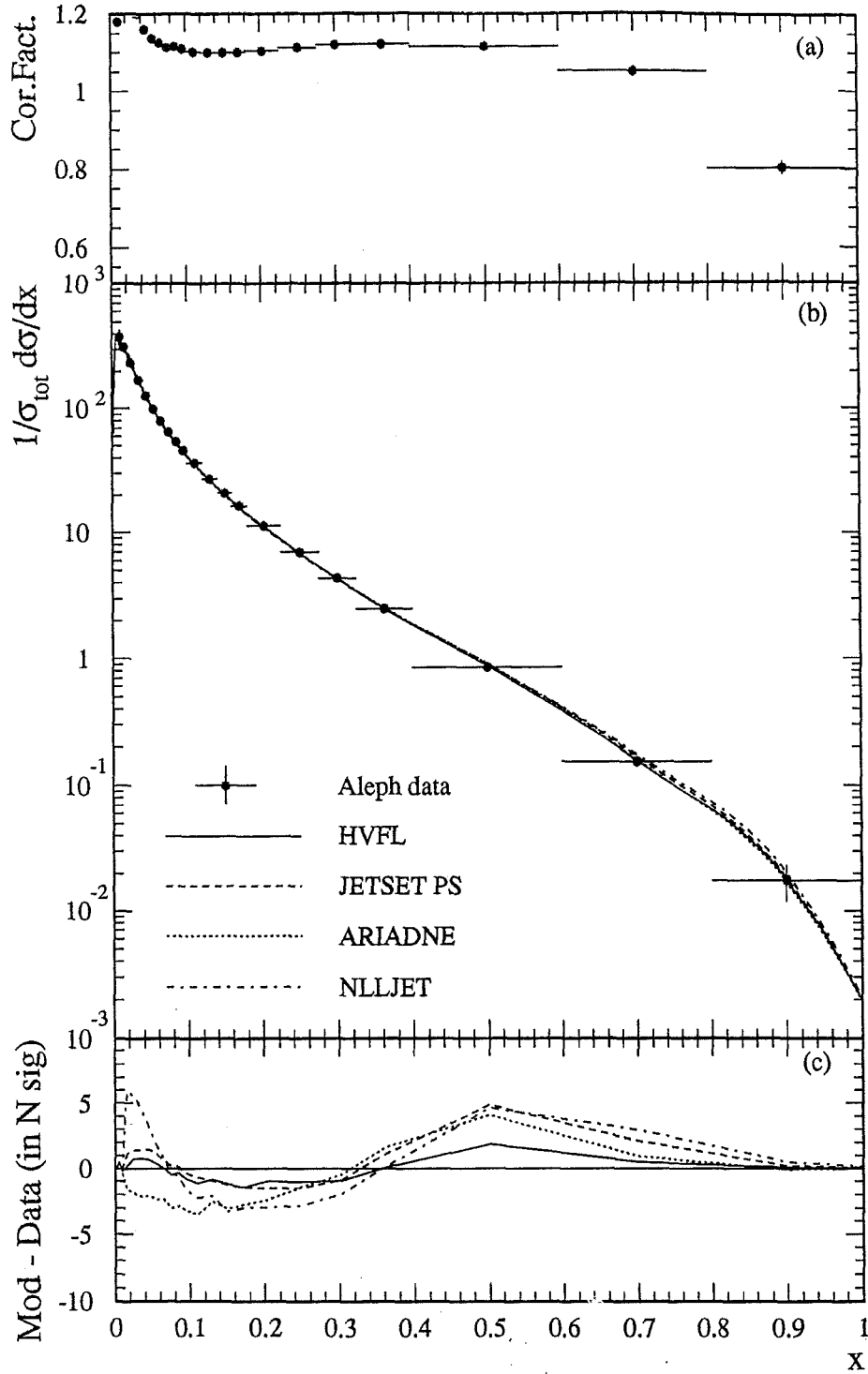


Figure 5.8: Correction factors applied to the transverse inclusive energy distribution(a), corrected distribution and comparison with different MonteCarlo models (b), and deviation of the models from the corrected data measured in number of standard deviations, where the error includes

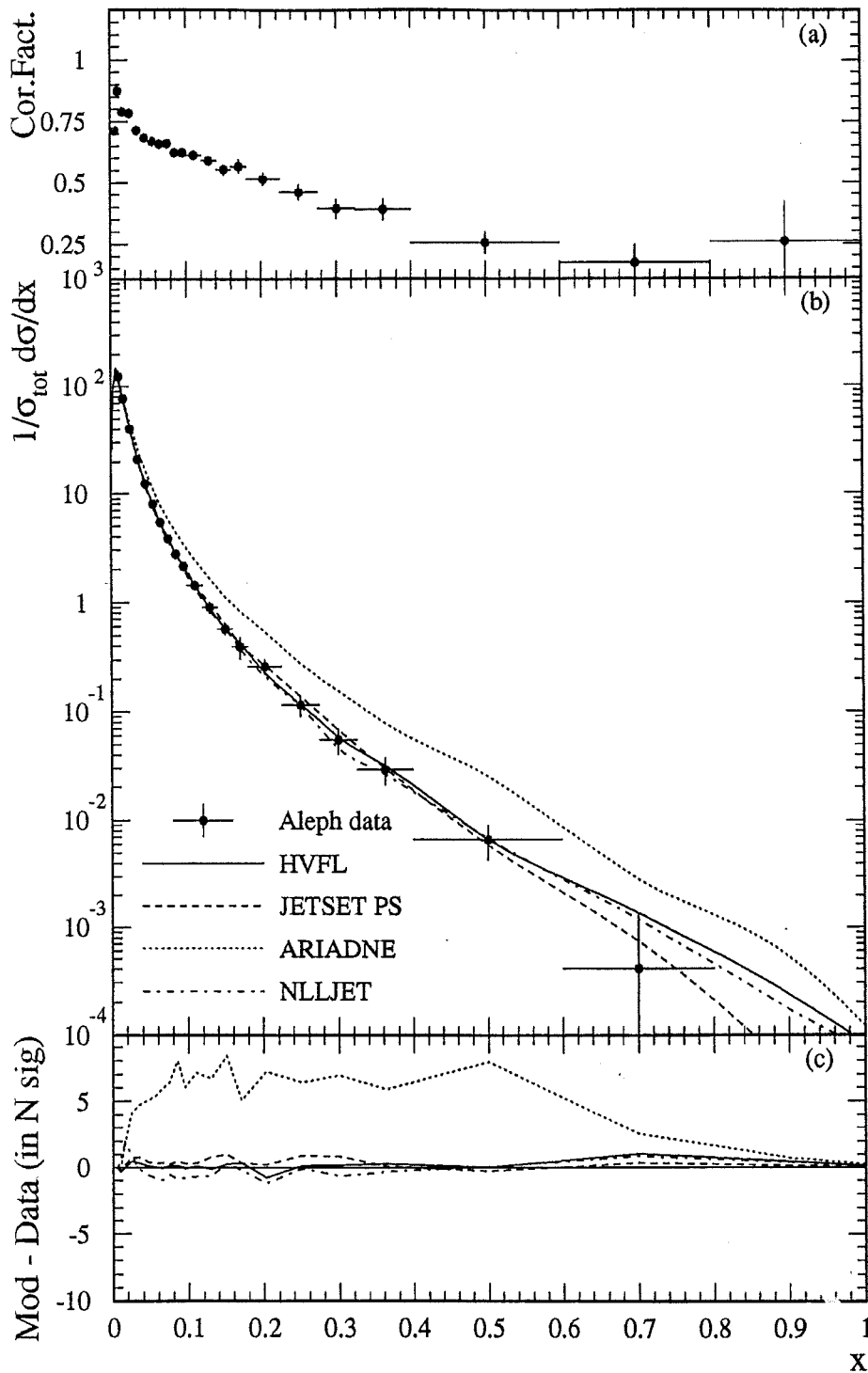


Figure 5.9: Correction factors applied to the longitudinal inclusive energy distribution(a), corrected distribution and comparison with different MonteCarlo models (b), and deviation of the models from the corrected data measured in number of standard deviations, where the error includes

transverse scaled energy distribution (figure 5.8(a)) are rather similar to the corresponding ones for the total distributions (figure 5.1(a)), the ones for the longitudinal distribution (figure 5.9(a)) deserve more explanation.

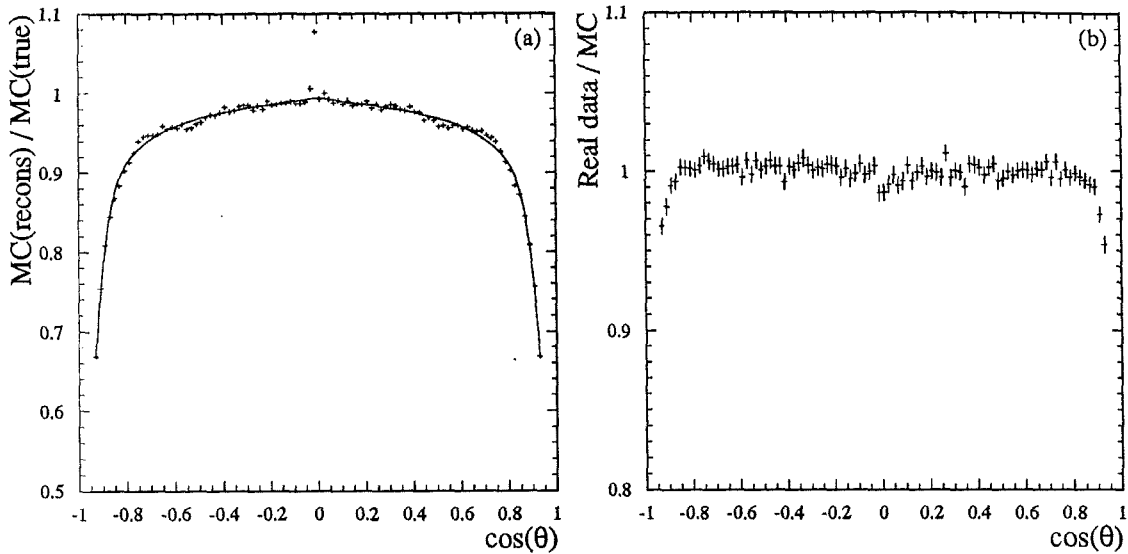


Figure 5.10: Angular efficiency of charged tracks (a) and angular difference between Monte Carlo simulated data and real data (b).

Figure 5.10(a) shows the tracks selection efficiency for tracks inside the acceptance of $v = 0.94$. The hypothesis that this efficiency is constant over all the angles is not true and this causes these correction factors, specially for the longitudinal distribution, to be larger. To confirm this hypothesis, studies with a toy Monte Carlo, parametrizing the angular track selection efficiency to the sum of a cubic polynomial and a hyperbolic tangent as a function of θ . This parametrization is shown by the continuous line in figure 5.10(a). The correction factors obtained with this toy Monte Carlo follow the qualitative behaviour of the ones shown in figure 5.9(a). Thus, would be avoided correcting the angular distribution before projecting the double differential cross section of x and $\cos \theta$ into the longitudinal and transverse distributions. However, conceptually is the same that include this effect in the bin to bin correction made.

Figure 5.10(b) shows the angular differences in between real and simulated data. There exist differences below 1% in almost the whole angular interval, except for angles below $\sim 25^\circ$. To take into account, the analysis was repeated with this value

for the acceptance and the difference with the nominal distribution was taken into account in the systematic error computation which followed the same procedure explained in section 5.2.

The cross sections and the detailed error contributions for the transverse and longitudinal scaled energy distributions are given in tables C and C in appendix C.

For the measurement of the longitudinal and transverse distributions the requirement on the sphericity axis is removed, as it would introduce a strong $\cos \theta$ dependence in the track selection efficiency. This effect is taken into account in the correction procedure, which is identical to that used for the other distributions. Although it leads to somewhat larger corrections those are well understood, with the uncertainty in the reconstruction efficiency propagated into the systematic errors.

5.7 Low energy data

In addition to the ALEPH data, inclusive charged particle spectra from TASSO [43] at $\sqrt{s} = 22, 35$ and 45 GeV, MARK II [44] and TPC/2 γ [45] at $\sqrt{s} = 29$ GeV, CELLO [46] at $\sqrt{s} = 35$ GeV, AMY [47] at $\sqrt{s} = 55$ GeV and DELPHI [48] at $\sqrt{s} = 91.2$ GeV have been used. Lower-energy data have been discarded because of the larger size of power-law corrections.

Further treatment to the errors was done in the cases where normalization errors were not specified. In some cases neither statistical and systematic errors were separated. The principle to estimate the normalization error was to take the minimum percentual systematic error as normalization error. To perform this, first the statistical errors were computed from the published number of event used in the measurement. This error was subtracted in quadrature to all the bins to compute the systematic error. The minimum percentage of computed systematic error was taken as percentual normalization error for all the bins. Table 5.7 shows the normalization errors for all the experiments used in the analysis.

Experiment	Normalization error
Tasso (22 GeV)	2.3%
Tasso (35 GeV)	1.0%
Tasso (44 GeV)	1.5%
Mark II (29 GeV)	1.5%
TPC/ 2γ (29 GeV)	3.2%
Amy (55 GeV)	0.4%
Delphi (91.2 GeV)	3.0%
Aleph (91.2 GeV)	1.0%

Table 5.3: Normalization errors used in the x-inclusive distributions for all the experiments used in the analysis. The errors on TPC/ 2γ , DELPHI and ALEPH are from the published papers. The rest are estimated as explained in the text.

Chapter 6

Description of the analysis

In chapter 2 was shown that the effective fragmentation functions evolve with the energy in a way that is predictable by perturbative QCD. This evolution depends on α_s . Therefore, data at different centre-of-mass energies can be used to extract a value of the strong coupling constant in an analogous way as it is done in deep-inelastic scattering with the structure functions, which evolve following analogous evolution equations as the fragmentation functions in e^+e^- annihilation.

Schematically, a QCD test based on measurements of inclusive cross sections at different centre-of-mass energies, E_{cm} , can be visualized as shown in figure 6. Assuming a given set of fragmentation functions is specified at an initial factorization scale μ_i , perturbative QCD relates those fragmentation functions to an observable cross-section which, after inclusion of the non-perturbative power-law corrections, can be compared with experimental data (horizontal arrows). The natural choice

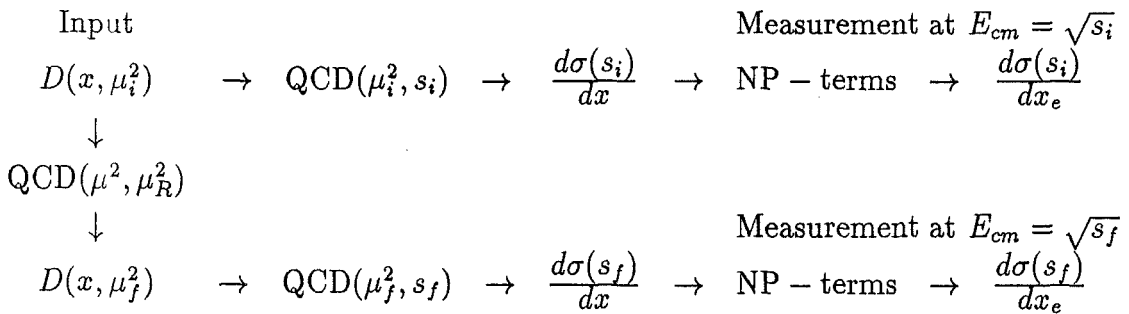


Figure 6.1: Scheme of the scaling violations analysis

is $\mu_i = s_i$ and $\mu_f = s_f$. Since the fragmentation functions are not calculable in perturbative QCD they can be adjusted such that the theoretical prediction agrees with the data at a given energy. However, having once fixed the initial conditions, a QCD test can be performed by comparing the QCD prediction for various centre-of-mass energies to actual measurements. The energy evolution (vertical arrows) of the fragmentation functions again is described by perturbative QCD. Here the renormalization scale μ_R^2 appears, i.e. the energy variation of the fragmentation functions at the scale μ is expressed as function of μ and the renormalization point μ_R^2 . The natural choice is $\mu_R = \mu$

Although the analysis scheme presented seems to be simple, there are some practical problems that have to be solved before a reliable measurement of α_s can be performed. An important one is the fact that there exist evolution equations for fragmentation functions corresponding to each flavour and the gluon, and none of them have been measured isolated so far at any energy. In fact they cannot be measured directly, but their value should be inferred from their relation to the measurable cross-sections as given in equation (??) and as described above. The measurement of the fragmentation function for each flavour would have little importance if flavour percentage composition would be the same at all the energies. But this is not the case as it was shown in ?? Thus, the b-flavour softer fragmentation function enriched composition of the scaled energy distribution at LEP with respect to lower energies, would be a source of fake scaling violation that have nothing to do with strong interactions. Even if these measurements are made, the coarse binning of the data does not allow to do an accurate enough evolution without a parametrization of the fragmentation functions, which should be supported by some physics arguments.

Another still undefined part of the analysis is the introduction of the non-perturbative contributions to the evolution. In sections ?? some sources of power-law corrections were presented. There are corrections that go as $1/\sqrt{s}$ and another ones that go as $1/s$. Although it is expected that the dominant one is coming from hadronization corrections (section ??), which go as $1/\sqrt{s}$, the actual form of the non-perturbative contribution to the evolution are not known and some parametrization has to be performed also in these terms.

Still some more practical problems arise. The evolution equations and the ones that relate the fragmentation functions with the cross-sections are not at all triv-

ially solvable equations. The methods to handle this numerical problem are also described in this chapter.

6.1 Evaluation of the Convolution Integrals

The equations relating the fragmentation functions to the measured cross-sections (section ??) and the evolution equations themselves (section ??) contain multiple convolution integrals of the type

$$\int_x^1 dz P(z)Q(x/z). \quad (6.1)$$

As the functions P and Q are rather complicated expressions of their argument, a fast algorithm to perform those integrals, which avoids a lot of slow numerical integrations, has to operate on tabulated function values. Thus, a uniform coverage in x and z , based on n subdivisions of the interval $[0,1]$ would require to tabulate $P(z)$ on n , and $Q(x/z)$ on n^2 grid points, which already for a moderately small coordinate spacing results in huge memory requirements.

These can be avoided going to another set of variables. Since the evolution of the fragmentation functions at a fractional momentum x_0 only depends on the values of the fragmentation and splitting functions at $x > x_0$, the analysis can be restricted also to a finite region in $\ln x$. It is therefore possible to substitute x and z by $t = \ln(z)$ and $u = \ln(x)$. In these variables equation (6.1) becomes

$$\int_x^1 dz P(z)Q(x/z) = \int_u^0 dt \tilde{P}(t)\tilde{Q}(u-t) \quad (6.2)$$

with

$$\tilde{P}(t) = e^t P(e^t) \quad \text{and} \quad \tilde{Q}(u-t) = Q(e^{u-t}). \quad (6.3)$$

Choosing an equidistant grid in the new variables allows to evaluate the convolution integrals based on the same number of tabulated points for both \tilde{P} and \tilde{Q} . Indexing the grid points from 1 to n , the convolution integral (6.2) can be approximated by the sum

$$\int_x^1 dz P(z)Q(x/z) \approx \Delta \sum_{i=k}^n \tilde{P}_i \tilde{Q}_{n-i} \quad (6.4)$$

where k is the index of the first \tilde{P}_i such that $P(z > x)$ and Δ is the grid spacing in the transformed variables. The original convolution integral has been turned into a scalar product between two partial arrays of tabulated function values.

An algorithmically simple way to do the convolution integrals is only one aspect. In addition high numerical accuracy is required. The simple unweighted sum (6.4) evaluates the convolution integral with a residual error $\mathcal{O}(\Delta)$. This can be improved to $\mathcal{O}(\Delta^4)$ with only minimal additional computing costs by using the alternative extended Simpson's rule [39], where (6.4) is improved by adding a correction term which only depends on the function values at the first and last four knots. The alternative extended Simpson's rule requires at least $N = 8$ knots where the integrand is evaluated. The cases $N < 8$ have to be dealt with individually.

A collection of integration rules for arbitrary $N > 0$ is given below. Information about how they are derived can be found in [39]. Let

$$\int_a^b dx f(x) = I \quad (6.5)$$

be the integral to be evaluated. Estimates for I shall be based on N evaluations $y_k = f(x_k)$, $k = 1, \dots, N$, of the integrand on an equidistant grid with grid spacing Δ . If both endpoints are included, $x_1 = a$, $\Delta = (b - a)/(N - 1)$ and $x_N = b$. A complete set of closed quadrature formulas I_N is given by:

$$I_1 = 0 \quad (6.6)$$

$$I_2 = \frac{\Delta}{2}(y_1 + y_2) \quad (6.7)$$

$$I_3 = \frac{\Delta}{3}(y_1 + 4y_2 + y_3) \quad (6.8)$$

$$I_4 = \frac{3}{8}\Delta(y_1 + 3y_2 + 3y_3 + y_4) \quad (6.9)$$

$$I_5 = \frac{\Delta}{3}(y_1 + 4y_2 + 2y_3 + 4y_5 + y_5) \quad (6.10)$$

$$I_6 = \frac{\Delta}{48}(17y_1 + 59y_2 + 44y_3 + 44y_4 + 59y_5 + 17y_6) \quad (6.11)$$

$$I_7 = \frac{\Delta}{3}(y_1 + 4y_2 + 2y_3 + 4y_4 + 2y_5 + 4y_6 + y_7) \quad (6.12)$$

$$I_N = \Delta \sum_{k=1}^N y_k - \frac{\Delta}{48}(31y_1 - 11y_2 + 5y_3 - y_4 - y_{N-3} + 5y_{N-2} - 11y_{N-1} + 31y_N) \quad N \geq 8. \quad (6.13)$$

For functions which are difficult to evaluate at $x = b$, a modified set of open quadrature formulas I_N^+ can be derived. Here the information from the given grid points is extrapolated into the region between x_N and b . With $x_1 = a$, $\Delta = (b - a)/N$

and $x_N = b - \Delta$, the following expressions, which are of the same accuracy as the closed formulas given above are obtained:

$$I_1^+ = I_1 + \Delta y_1 \quad (6.14)$$

$$I_2^+ = I_2 + \frac{\Delta}{2}(3y_2 - y_1) \quad (6.15)$$

$$I_3^+ = I_3 + \frac{\Delta}{12}(23y_3 - 16y_2 + 5y_1) \quad (6.16)$$

$$I_N^+ = I_N + \frac{\Delta}{24}(55y_N - 59y_{N-1} + 37y_{N-2} - 9y_{N-3}) \quad N \geq 4 \quad (6.17)$$

6.2 Methods to solve the Evolution equations

Looking at the non trivial structure of the evolution equations (2.38), it can be deduced that is almost unavoidable to use some numerical method to solve them. The standard method used in the analysis is the Runge-Kuta method. However, in some cases, different approach can be useful. The Moment analysis, apart of being an elegant method, allows to solve the equations analytically, at least, restricted to first order in α_s . This is no longer true when order α_s^2 is introduced. Therefore, this method is only used in the study of Monte Carlo models to try to have an insight in the parametrization of the non-perturbative terms.

6.2.1 Runge-Kuta Method

The general problem of solving a system of differential equations of any order can be reduced to solve a coupled system of N first-order equations like

$$\frac{dy_i(x)}{dx} = f_i(x, y_1, \dots, y_N), \quad i = 1, \dots, N \quad \longrightarrow \quad \frac{d\vec{y}(x)}{dx} = \vec{f}(x; \vec{y}). \quad (6.18)$$

Knowing the solution at a point x_n , a solution can be found at the point $x_{n+1} \equiv x_n + h$ with

$$y_{n+1}^{\vec{}} = \vec{y}_n + h \vec{f}(x_n, \vec{y}(x_n)) + \mathcal{O}(h^2) \quad (6.19)$$

However, the method above is unstable and not enough accurate. Instead, the fourth-order Runge-Kuta method, which is more robust and precise, can be used [39]. For each step in the solution, the following sequence of evaluations must be made

for each of the f_i

$$\begin{aligned}
 k_1 &= h f(x_n, y_n) \\
 k_2 &= h f\left(x_n + \frac{h}{2}, y_n + \frac{k_1}{2}\right) \\
 k_3 &= h f\left(x_n + \frac{h}{2}, y_n + \frac{k_2}{2}\right) \\
 k_4 &= h f(x_n + h, y_n + k_3) \\
 y_{n+1} &= y_n + \frac{k_1}{6} + \frac{k_2}{3} + \frac{k_3}{3} + \frac{k_4}{6} + \mathcal{O}(h^5)
 \end{aligned} \tag{6.20}$$

where f stands for any of the f_i . It is easy to transport the method described in equations (6.20) to the evolution equations (2.38), where the right-hand f_i of (6.20) are the convolution integrals, h is the evolution variable, $\log \sqrt{s}$, and the y are each of the values of the tabulated fragmentation functions. The value of h was chosen to be the logarithmic difference between the center of mass of two consecutive distributions.

6.2.2 Moments analysis method

An alternative method to solve the evolution equations is to convert them in simple differential equations. The evolution equations for the singlet (2.42) and non-singlet (??) parts, contain convolution integrals that, forgetting the energy dependence, are of the form

$$\int_x^1 dz P(z) A\left(\frac{x}{z}\right). \tag{6.21}$$

Taking into account that x and z take values between 0 and 1, this can be written in the form

$$\int_0^1 dy \int_0^1 dz \delta\left(y - \frac{x}{z}\right) P(z) A(y) \tag{6.22}$$

where the lower limit in the integral over the z variable can be moved from x to 0 because the δ function ensures that the integrand is zero over the added interval between 0 and x . Multiplying this by a power of x and integrating over the whole interval, gives

$$\int_0^1 dx x^n \int_0^1 dy \int_0^1 dz z \delta(x - yz) P(z) A(y) = \int_0^1 dy y^n A(y) \cdot \int_0^1 dz z^{n+1} P(z). \tag{6.23}$$

This property can be used to simplify the evolution equations in such a way that they become simple differential equations when they are expressed in form of

the moments of the fragmentation functions. The formalism is described in detail in [?]. Here it is described at leading order, since this formalism was used in the leading order study of the scaling violations with the different Monte Carlos with the purpose to have an insight of the parametrization of the non-perturbative power-law corrections (section 6.4).

The moments of the cross-sections are defined in such a way that the zeroth-order moment is related with the energy-momentum conservation sum rule:

$$M_n = \int_0^1 dx x^{n+1} \frac{d\sigma}{dx}. \quad (6.24)$$

Then, taking into account that the singlet and non-singlet parts of the fragmentation functions have been defined weighted with x according to eq. (2.40), the n -order moment for the singlet, non singlet and gluon fragmentation function has to be defined as

$$A_n = \int_0^1 dx x^n A(x, s) \quad A = N, S, G. \quad (6.25)$$

Up to leading order, the running coupling constant is given by

$$\alpha_s(s) = \frac{1}{b_0 t} \quad (6.26)$$

where b_0 is given in (??) and t is defined as

$$t = \ln \left(\frac{s}{\Lambda^2} \right) \quad (6.27)$$

being Λ the effective QCD scale described in section ?? . With this definitions, and the property of equation (6.23), it is easy to show that the evolution equations simplify to

$$\begin{aligned} t \frac{d}{dt} \begin{pmatrix} S_n \\ G_n \end{pmatrix} &= \begin{pmatrix} a_{\text{QQ}}^n a_{\text{GQ}}^n \\ a_{\text{QG}}^n a_{\text{GG}}^n \end{pmatrix} \begin{pmatrix} S_n \\ G_n \end{pmatrix} \\ t \frac{d}{dt} N_n &= a_{\text{QQ}}^n N_n. \end{aligned} \quad (6.28)$$

with the coefficient a_{xx}^n given by

$$b_0 a_{\text{QQ}}^n = \left[-\frac{1}{2} + \frac{1}{(n+2)(n+3)} - 2 \sum_{j=2}^{n+2} \frac{1}{j} \right] \quad (6.29)$$

$$b_0 a_{\text{GG}}^n = 2X \left[-\frac{1}{12} + \frac{1}{(n+1)(n+2)} + \frac{1}{(n+3)(n+4)} - \sum_{j=2}^{n+2} \frac{1}{j} \right] - \frac{2}{3} Z \quad (6.30)$$

$$b_0 a_{\text{GQ}}^n = \frac{n^2 + 5n + 8}{(n+1)(n+2)(n+3)} \quad (6.31)$$

$$b_0 a_{\text{QG}}^n = 2Z \frac{n^2 + 5n + 8}{(n+2)(n+3)(n+4)} \quad (6.32)$$

where X , Z , and b_0 are defined equations (2.12) and (2.20). The solution of the non-singlet part is rather trivial and gives

$$N_n(s) = N_n(s_0) \left(\frac{\ln(s/\Lambda^2)}{\ln(s_0/\Lambda^2)} \right)^{a_{\text{GQ}}^n}. \quad (6.33)$$

The solution for the coupled system needs a little bit more algebra and can be expressed as

$$\begin{pmatrix} S(t) \\ G(t) \end{pmatrix} = \alpha_1 \vec{e}_1 \left(\frac{t}{t_0} \right)^{\lambda_1} + \alpha_2 \vec{e}_2 \left(\frac{t}{t_0} \right)^{\lambda_2} \quad (6.34)$$

where $\lambda_{1,2}$ are the eigenvalues of the respective coefficient matrix a_{xx} and $\vec{e}_{1,2}$ the corresponding eigenvectors. The parameters $\alpha_{1,2}$ are determined through the initial conditions for $t = t_0$ at the initial centre-of-mass energy $\sqrt{s_0}$.

6.3 Parametrization of the fragmentation functions

The scheme presented in figure 6 assumes that the fragmentation functions are specified at one particular energy scale. With enough amount of data, it would be possible to perform a moment analysis, in a similar way as the described in section 6.2.2, where this parametrization would not be necessary. But, the coarse binning of the data due to statistical limitations does not allow to fix the initial conditions truly unambiguously. Some assumptions about the shape of the fragmentation functions must be done, the least restrictive ones being the requirements of positiveness and smoothness. The most convenient approach is to use a phenomenological parametrization, where the shape is described by a small number of free parameters.

Perturbative QCD, in the framework of the modified leading-log approximation (MLLA), predicts that the momentum spectrum of final state particles should exhibit and approximately gaussian peak in $\ln x$ [?] From this, it can be inferred a functional form for the fragmentation function like

$$\frac{d\sigma}{d \ln x} \sim \exp(-c(d - \ln x)^2) \quad \Leftrightarrow \quad \frac{d\sigma}{dx} \sim \frac{1}{x} \exp(-c \ln^2 x) x^{2cd}. \quad (6.35)$$

Combined with the expectation that the momentum spectrum falls off with some power of $1 - x$ for $x \rightarrow 1$ finally yields the ansatz

$$D(x) = N(1 - x)^a x^{b-1} \exp(-c \ln^2 x), \quad (6.36)$$

where N , a normalization constant and a , b and c are free parameters which have to be determined from the data. With the possible exception of c , the parameters are expected to be different for light quarks, c -quarks, b -quarks and gluons. The parameter c is in principle predicted by the MLLA and, in leading order, should also be flavour independent. Treating it as an effective phenomenological parameter, flavour independence a priori cannot be expected to hold any more. However, it turns out that the experimental data actually support the idea that c is a universal parameter. Taking it to be the same for all flavours successfully improves the description of the measured cross sections towards small x significantly with only one additional parameter.

In order to avoid correlations between the normalization and the rest of parameters, the final parametrization function chosen for the analysis is given by

$$xD_i(x, s_0) = N_i \frac{(1 - x)^{a_i} x^{b_i} \exp(-c \ln^2 x)}{\int_{0.1}^{0.8} dx (1 - x)^{a_i} x^{b_i} \exp(-c \ln^2 x)}, \quad (6.37)$$

where i stands for uds , c , b , and g (gluons), and the dependence on s_0 comes from the implicit dependence of the parameters (N_i , a_i , b_i and c) on this variable.

6.4 Parametrization of the non-perturbative terms

The only missing ingredient in the analysis scheme of figure 6 is the parametrization of the power-law corrections to the perturbative evolution. Given sufficient data, it would also be possible to determine them from the data without strong external assumptions. Such an approach was followed in the analysis of the SLAC/BCDMS deep-inelastic scattering data [?]. There the power-law corrections were known to behave like $1/Q^2$ with the available data covering the range $0.5 \text{ GeV}^2 < Q^2 < 260 \text{ GeV}^2$. In the study of scaling violations in fragmentation functions the power-law corrections are expected to behave like $1/\sqrt{s}$, while a typical analysis covers data in the range from $22 \text{ GeV} < \sqrt{s} < 91 \text{ GeV}$. Thus the dynamical range to separate power-law

corrections from the logarithmic scaling violations due to perturbative QCD is 125 times larger in deep-inelastic scattering experiments than it is in e^+e^- -annihilation. This severely restricts the number of parameters describing non-perturbative effects that can be determined from the data to essentially only a single number.

A simple effective way of parametrizing the non-perturbative effect is by doing a change of variables and relate the perturbative variable x to the measured quantity x_e through $x = g(x_e)$. Imposing the condition of energy conservation before and after the transformation fixes the relation between the perturbative prediction $\sigma(x)$ and the observable cross section $\sigma_{NP}(x_e)$:

$$\int dx x \frac{d\sigma}{dx} = \int dg(x_e) g(x_e) \frac{d\sigma}{dx} = \int dx_e g(x_e) g'(x_e) \frac{d\sigma}{dx} = \int dx_e x_e \frac{d\sigma_{NP}}{dx_e} \quad (6.38)$$

From this, it can be deduced that

$$\frac{d\sigma_{NP}}{dx_e} = \frac{g(x_e) g'(x_e)}{x_e} \frac{d\sigma}{dg(x_e)}. \quad (6.39)$$

The simplest ansatz for g is given by a rescaling of the type $x = x_e(1+h_1/\sqrt{s})$ [?]. However, it was found that some other corrections could work better. A general ansatz for the non-perturbative effects is given by

$$x = g(x_e) = x_e + (h_0 + h_1 x_e + h_2 x_e^2 + \dots) \left[(\sqrt{s})^{-k} - (\sqrt{s_0})^{-k} \right]. \quad (6.40)$$

Using only the parameter h_0 means that the perturbative prediction and the observable cross-sections are related by a shift of the spectra, using only h_1 corresponds to a rescaling of x . The energy-dependence of this transformation is given by the term in square brackets. This term is built such that the non-perturbative corrections are zero at the scale $\sqrt{s_0}$ where the fragmentation functions are parametrized, which takes into account the fact that the fragmentation functions themselves already parametrize all non-perturbative effects at a given scale. Perturbative QCD then predicts logarithmic scaling violations in the evolution of those fragmentation functions, and the above ansatz takes care of the power law corrections that come on top.

Section ?? describes the different sources of non-perturbative corrections to the evolution. There are sources in which $k = 1$ and another ones in which $k = 2$. Since the number of parameters allowed from the currently available experimental is only one, some guidance about the appropriate choice has to be taken from

Monte Carlo simulations of e^+e^- annihilation processes into hadrons. In addition to a discrimination between using h_0 and h_1 (shift versus rescaling) those models also allow to infer the power k to be used in ??.

For this purpose a leading-order moments analysis as described in section 6.2.2 was performed on results of the JETSET, ARIADNE and HERWIG Monte-Carlo models. Here even the higher moments of the fragmentation functions can be reliably determined, something which unfortunately is practically impossible for the comparatively coarse-binned published experimental x -distributions. Moments can be viewed as a convenient means to describe the shape of the fragmentation functions without having to resort to an explicit parametrization. Low order moments probe mainly the low x -part of the distribution, higher order moments progressively test the region $x \rightarrow 1$. The next sections describe this analysis and the parametrization of the non-perturbative terms used in the analysis described in section ??.

6.4.1 Non-perturbative terms in the Moments analysis

The missing ingredient to perform the Moments analysis is the inclusion of the non-perturbative effects. This is easy for the two parametrizations discussed above (section 6.4). Defining

$$f(x) = \frac{d\sigma}{dx}(x) \quad (6.41)$$

$$a_1 = 1 + h_1 \left[(\sqrt{s})^{-k} - (\sqrt{s_0})^{-k} \right] \quad (6.42)$$

$$a_0 = h_0 \left[(\sqrt{s})^{-k} - (\sqrt{s_0})^{-k} \right] \quad (6.43)$$

the introduction of the reescaling in the moments becomes

$$M_n(\text{NP}) = \int_0^1 dx_e x_e^{n+1} f_{\text{NP}}(x_e) = \int_0^1 dx_e a_1^2 x_e^{n+1} f(a_1 x_e) = \int_0^{a_1} \frac{dx}{a_1} a_1^2 \frac{x^{n+1}}{a_1^{n+1}} f(x) = \int_0^{a_1} dx a_1^{-n} x^{n+1} f(x) \quad (6.44)$$

were the last step is done because the integral in the interval $(0, a_1)$ in y is the whole phase space as $(0, 1)$ is for the variable x .

In the case of the shift,

$$M_n(\text{NP}) = \int_0^1 dx_e x_e^{n+1} f_{\text{NP}}(x_e) = \int_0^1 dx_e \frac{x_e + a_0}{x_e} x_e^{n+1} f(x_e + a_0) \quad (6.45)$$

$$= \int_0^1 dx_e \left(1 + \frac{a_0}{x_e} \right) x_e^{n+1} \left[f(x_e) + a_0 f'(x_e) + \frac{1}{2} a_0^2 f''(x_e) \dots \right] \quad (6.46)$$

where a Taylor expansion is made in the cross-section. The following property can be applied

$$\int_0^1 dx f'(x) = -(n+1) M_{n-1} \quad (6.47)$$

to transform equation 6.46 in

$$\begin{aligned} M_n(\text{NP}) &= M_n + a_0 M_{n-1} - a_0(n+1) M_{n-1} - a_0^2(n) M_{n-2} + \frac{1}{2} a_0^2 n(n+1) M_{n-2} \\ &= M_n - n a_0 M_{n-1} + \frac{n(n-1)}{2} a_0^2 M_{n-2} \end{aligned} \quad (6.48)$$

giving finally

$$M_n(\text{NP}) = \sum_{k=0}^n \binom{n}{k} M_k (-a_0)^{n-k} \quad (6.49)$$

Here M_n are the moments without power-law corrections and $M_n(\text{NP})$ the moments including the non-perturbative effects.

6.4.2 Monte Carlo study

The energy-evolution of the moments seen in the Monte Carlo to the leading-order QCD prediction allows to infer the behaviour of the non-perturbative corrections. A leading-order analysis is justified since the Monte Carlo models are based on a leading-log cascade and only partially incorporate next-to-leading logarithmic effects. Although the HERWIG model approaches [?] the true next-to-leading order case for $x \rightarrow 1$, the above justification at least holds for the analysis of the low-order moments.

Monte Carlo data containing 1 Million events were generated with the natural flavour mix for centre-of-mass energies of 22, 35, 44, 55 and 91 GeV for all three models. At 91 GeV, additional samples of 1 Million events with primary c - and b -quarks were generated. From this the moments for light-, c - and b -quark fragmentation functions at an initial scale of 91 GeV were determined. The gluon fragmentation function, which in leading order does not contribute to the observable cross section but is needed in the evolution equations, was assumed to be equal to the c -quark fragmentation function. The associated uncertainty was estimated by alternatively setting it equal to the b -quark fragmentation function and taking the corresponding change in the evolution of the moments as a theoretical error.

For the determination of the parameters governing the power-law corrections the QCD scale parameter Λ describing the logarithmic part of the scaling violations

JETSET 7.3		$\Lambda_{QCD} = 0.319 \text{ GeV}$			
Ansatz	χ^2/n_{df}	Parameter Value h			
h_0 $1/\sqrt{s}$	154	-0.78	± 0.15	± 0.15	
h_1 $1/\sqrt{s}$	183	-2.3	± 1.40	± 0.41	
h_0 $1/s$	356	-15.	± 1.7	± 2.8	
h_1 $1/s$	411	-45.	$\pm 28.$	± 7.8	
ARIADNE 4.02		$\Lambda_{QCD} = 0.225 \text{ GeV}$			
Ansatz	χ^2/n_{df}	Parameter Value h			
h_0 $1/\sqrt{s}$	46	-0.59	± 0.13	± 0.13	
h_1 $1/\sqrt{s}$	56	-1.8	± 0.95	± 0.38	
h_0 $1/s$	132	-11.	± 1.7	± 2.5	
h_1 $1/s$	152	-35.	$\pm 20.$	± 7.4	
HERWIG 5.6		$\Lambda_{QCD} = 0.152 \text{ GeV}$			
Ansatz	χ^2/n_{df}	Parameter Value h			
h_0 $1/\sqrt{s}$	13	-0.41	± 0.12	± 0.11	
h_1 $1/\sqrt{s}$	15	-1.3	± 0.59	± 0.36	
h_0 $1/s$	43	-8.5	± 2.3	± 2.3	
h_1 $1/s$	48	-25.	$\pm 13.$	± 7.1	

Table 6.1: Monte-Carlo studies of non-perturbative correction.

was fixed to the input value used for the respective model. Different functional forms for the non-perturbative corrections were tried separately for the leading ten moments in single-parameter fits of h_0 and h_1 assuming the energy dependence to be $1/\sqrt{s}$ or $1/s$. The parametrization scale was set to $\sqrt{s_0} = 22 \text{ GeV}$.

The results are summarized in table 6.1 and one example is displayed in figure ?? . For each ansatz of the non-perturbative terms the average chisquare per degree of freedom $\overline{\chi^2/n_{df}}$ is given together with the value obtained for the non-perturbative parameter h_i . The quoted number is the central value obtained over the first 10 moments, the first error the corresponding half-range and the second one the half range found when varying the QCD scale from one half to twice its nominal value. The statistical errors are completely negligible.

Although $\overline{\chi^2/n_{df}}$ is rather large one has to keep in mind that the Monte Carlo statistics used in this study is roughly a hundred times of what is available in

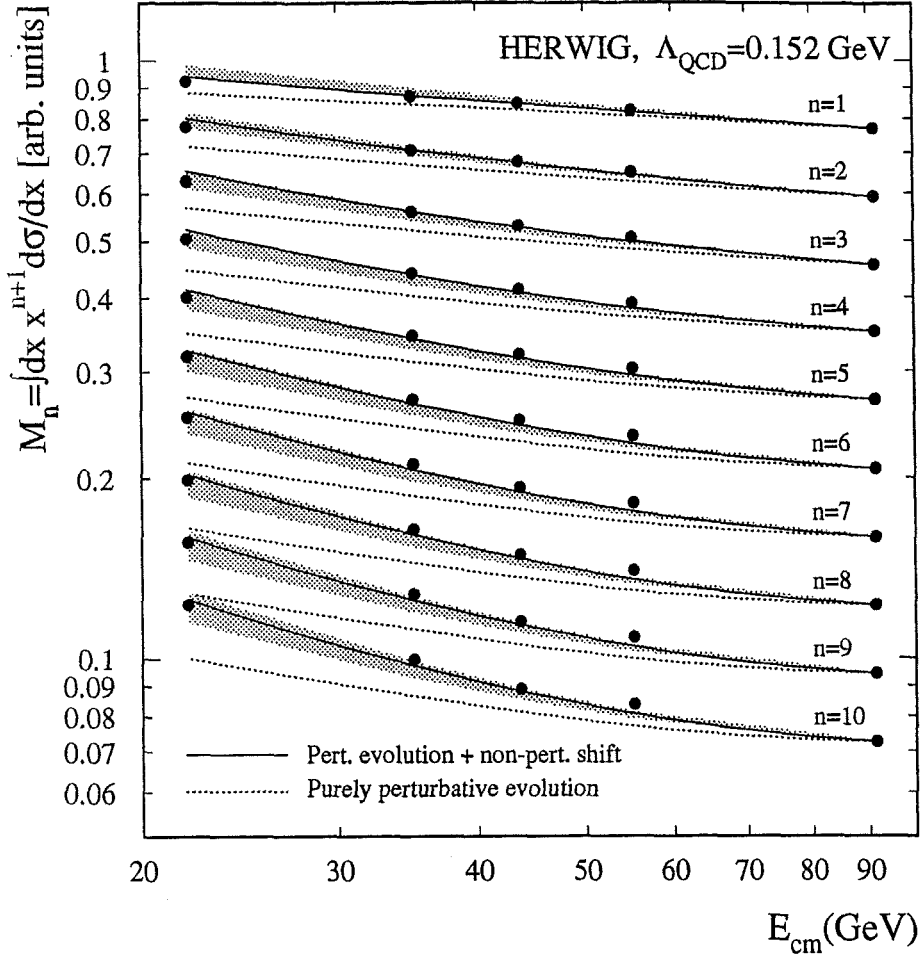


Figure 6.2: Energy evolution for the leading moments of the inclusive x -distributions as predicted by the HERWIG model. The points are the actual moments, the curves are the results of a leading order QCD analysis. The dotted lines show the result of a purely perturbative evolution from 91 GeV to 22 GeV. The full lines are evolutions over the same range with power law corrections included in such a way that they vanish at $\sqrt{s} = 22$ GeV; $x = x_e + h_0(1/\sqrt{s} - 1/22)$. The parameter h_0 is optimized separately for each moment. The shaded bands finally are obtained by varying a global parameter h_0 between the extreme values found in the individual fits.

the data. Consequently even values $\chi^2/n_{df} \approx \mathcal{O}(100)$ correspond to a satisfactory description of the data. As can be seen from figure 6.2 even despite the bad χ^2 the qualitative behaviour is well reproduced by the fits. Studying the χ^2 -values given in table 6.1 shows that a power-law behaviour with $1/\sqrt{s}$ is clearly preferred over a $1/s$ dependence. Concerning the choice of h_0 versus h_1 the χ^2 -values are less conclusive. However, from the spread of the results (first quoted error) one sees, that h_0 is much more stable than h_1 . This can be traced to the fact that the fitted

value for h_1 becomes more and more negative for lower order moments, i.e. when putting more emphasis on the low- x region, suggesting a behaviour $h_1 \sim 1/x$ which is equivalent to parametrizing the non-perturbative terms by a shift h_0 .

In conclusion, the Monte-Carlo studies suggest a simple effective parametrization of the non-perturbative terms of the functional form

$$x = x_e + h_0 \left(\frac{1}{\sqrt{s}} - \frac{1}{\sqrt{s_0}} \right) \quad (6.50)$$

with a negative parameter h_0 .

6.5 Choice of parametrization scale

With the Monte Carlo parameters given in table 6.1 typical shifts in x are of the order $\Delta x = \mathcal{O}(0.01)$. At high values of x where the cross section goes to zero such a shift is much smaller than the experimental resolution and thus has only very little impact. At small x it amounts to a non-negligible change of the cross-section for two reasons: the momentum measurement is much more precise and the cross section rises rapidly. The fact that h_0 is negative and the functional form (6.50) suggests to use a parametrization scale $\sqrt{s_0}$ smaller or equal to the smallest scale used in a scaling violations analysis, such that the value x at which the perturbative cross section is evaluated in order to obtain the cross-section at the experimental value x_e is always larger than x_e . This assures that x never is needed at unphysical negative values. Unphysical values $x > 1$ may occur, but as explained above are much less severe and can easily be tolerated, thus permitting to have a really simple way of parametrizing non-perturbative effects.

Another argument to choose the smallest value of s_0 available for the parametrization of the fragmentation functions is the fact that the corrections to the evolution are of order $1/s$. Thus, they are expected to be smaller if they only account for the non-perturbative effects of the evolution to higher energies and the non-perturbative effect to the fragmentation are absorbed in the parametrization of the fragmentation functions at low energies that making it in the opposite way.

6.6 Results of the fit

An overall fit of the QCD predictions to all ALEPH and low energy data between 22 GeV and 91.2 GeV presented in chapter 5. Following the arguments given in section 6.5, the fragmentation functions for the different flavours are parametrized at 22 GeV according to equation (6.37). The non-perturbative effects are parametrized by (6.50). In total, thirteen parameters are used to describe the fragmentation functions at one energy. The evolution to another energy requires two more parameters: α_s , which determines the perturbative evolution, and h_0 , which parametrizes the non-perturbative effects in the evolution. Finally, the first order strong coupling constant, β_s , introduced in equation (??) is also required. Altogether there are sixteen parameters, which are all fit simultaneously to the available data.

The flavour-tagged distributions serve mainly the purpose of fixing the parameters of the corresponding fragmentation functions. The gluon-tagged sample and the longitudinal and transverse distributions determine the leading-order coupling constant, β_s , and the parameters of the gluon distribution function. Then, from the low energy data and the inclusive data at 91 GeV the values of α_s and h_0 are obtained.

The fit range is chosen as $0.1 < x < 0.8$ for all data at all energies. Outside this range, systematic effects, especially at low \sqrt{s} , start to become important. However, for the longitudinal cross section (measured only at 91 GeV), the fit range is taken as $0.04 < x < 0.8$ to increase the statistical sensitivity.

$\alpha_s(M_Z) = 0.1258 \pm 0.0053$				
$h_0 = -0.14 \pm 0.10 \text{ GeV}$				
	light (<i>uds</i>) quarks	<i>c</i> quarks	<i>b</i> quarks	gluons
<i>N</i>	0.372 ± 0.005	0.359 ± 0.006	0.295 ± 0.008	0.395 ± 0.020
<i>a</i>	1.69 ± 0.04	3.09 ± 0.16	3.29 ± 0.09	2.6 ± 0.8
<i>b</i>	-1.40 ± 0.06	-1.10 ± 0.09	-1.69 ± 0.07	-1.59 ± 0.29
<i>c</i>	0.252 ± 0.014			
β_s	0.199 ± 0.008			

Table 6.2: Results of the fit to all data. The errors include statistical and experimental systematic uncertainties, except for those related to flavour tagging. See text for definition of parameters.

The results of the fit are shown in Table ?? . There are sizable correlations amongst most of the parameters, which may be as large as 90% between the parameters of the fragmentation functions. The parameter most strongly correlated with $\alpha_s(M_Z)$ is the one describing the energy evolution of the non-perturbative terms, h_0 . Here the correlation is 36%. The value found for h_0 is compatible with zero, which indicates that non-perturbative effects are small, within the parametrization given by equation (6.50). Its influence in the α_s can be seen fixing it at its nominal value. The error on α_s decreases to ± 0.0049 . Thus, its contribution to the total error can be estimated to be ± 0.0020 . Fixing the parameters describing the shape of the fragmentation function and the non-perturbative corrections, the purely experimental error of $\alpha_s(M_Z)$ would be $\Delta\alpha_s = 0.0017$.

Figure 6.3 shows that the overall agreement between data and prediction is good and that the QCD evolution reproduces the observed scaling violations. All error bars include both statistical and experimental systematic uncertainties. This can be seen in better detail in figure ?? where the differences between the fitted and the measured value is plotted in number of standard deviations (statistical and systematic error of the measure distribution are included) of the measured distributions. All the distributions disagree with the fit result bellow $x = 0.1$, where the fit is not performed. This is due to inadequacies in the parametrization of the fragmentation function in this zone. High deviations are also observed at high x mainly due to experimental systematic uncertainties. The ALEPH data gives the impression of having a huge contribution to the total χ^2 mainly coming from the low momentum (bellow $x = 0.4$). This is not the case because all the data has the normalization error correlation (section 5.4.1) and it can be demonstrated that when the correlated error is the dominant one (as in the case in this momentum region for the ALEPH data), the contribution to the χ^2 is the same as the one coming from only one bin and not the sum of all the deviations of all the bins. Thus, although the deviations are two standard deviations for all the bins in this region, the contribution to the total χ^2 is only of roughly two units. A change in the normalization of $\approx 2\%$ in that region will make the distribution to agree almost perfectly.

The size of the scaling violations can be seen in Figure 6.5, where the ratio of the inclusive cross sections measured by ALEPH at $\sqrt{s} = 91.2 \text{ GeV}$ and TASSO as $\sqrt{s} = 22 \text{ GeV}$ is plotted as function of x . For comparison also the expectation

for the case all the distributions would have the same flavour composition as at 91.2 GeV is given. This can also be seen comparing the fragmentation functions obtained at the two energies (figure 6.6).

The value found for α_s agrees with previous ALEPH determinations [?, ?] and c with the MLLA expectation [?]. Also β_s is consistent with typical values for a leading-order α_s -measurement. Since β_s is allowed to vary, the information about the gluon fragmentation function obtained from the longitudinal cross section improves only marginally the direct measurement [?].

The χ^2 per degree of freedom of the fit is 307.3/213. The contributions from each distribution are detailed in table 6.6. The contributions from the ALEPH all flavour and enriched flavour distribution have to be considered only as approximate since the correlation among them were not considered when extracting their individual value.

Distribution	χ^2/n_{df}
Tasso (22 GeV)	7.3/13
Tasso (35 GeV)	44.6/13
Tasso (44 GeV)	13.6/13
Mark II (29 GeV)	36.8/14
TPC/2 γ (29 GeV)	9.5/12
Amy (55 GeV)	7.8/7
Delphi (91.2 GeV)	32.1/22
Aleph all flavours (91.2 GeV)	28.9/23
Aleph uds-enriched (91.2 GeV)	29.7/23
Aleph c-enriched (91.2 GeV)	26.9/23
Aleph b-enriched (91.2 GeV)	66.5/23
Aleph gluons (48 GeV)	2.8/5
Aleph Longitudinal (91.2 GeV)	7.8/16

Table 6.3: Detail of the χ^2/n_{df} per experiment in the standard analysis

As can be seen in table 6.6, three distributions contribute substantially: MARK II (37/14), TASSO at 35 GeV (45/13) and the ALEPH b -enriched sample (66/23). The large χ^2 for the b quark enriched sample is due to inadequacies of the simple parametrization of the fragmentation function. While the simple ansatz is good enough to describe the fragmentation of the gluon and the light quarks including

the c quark, it fails to reproduce the detailed structure of b quark fragmentation and decay over the full x -range. Removing the high- x points above $x = 0.6$ changes the χ^2/n_{df} to 31/19 while the result of the fit remains unchanged. The relatively high values of the χ^2 for MARKII and TASSO(35 GeV) point to an inconsistency in the experimental data, since there are data from other experiments at the same energy which are perfectly consistent with the QCD fits. In order to understand the importance of those problems for the fit, the errors of these two distributions are scaled up by the corresponding values of $\sqrt{\chi^2/\text{dof}}$, effectively deweighting the results from those experiments. The results of the fit with the enlarged errors and the ALEPH b -enriched sample restricted to the range $0.1 < x < 0.6$ is $\alpha_s(M_Z) = 0.127 \pm 0.006$, fully consistent with the previous one with an overall $\chi^2/n_{df} = 219/209$.

6.7 Systematic errors

The error in $\alpha_s(M_Z)$ presented in section ?? contains the statistical errors and most of the systematic errors from the measurement of the scaled energy distributions. Also the error from the correlations in all the parameters is included in the fit. The only missing uncertainties come from the assumption made in the normalization errors for those experiments in which this is not specified, the dependence of $\alpha_s(M_Z)$ on the assumed flavour composition for the enriched flavour scaled energy distributions, and the factorization and renormalization scale dependence,

6.7.1 Experimental systematic errors

Normalization errors assumption. In the low energy experiments where only the combined statistical and systematic errors have been published, the nominal result was performed with the assumptions explained in section 5.7 for the normalization errors. Alternatively, all unspecified errors were taken as bin-to-bin errors giving the result $\alpha_s(M_Z) = 0.1278 \pm 0.0058$. The corresponding shift of $\Delta\alpha_s = 0.002(\text{norm})$ was taken as an additional systematic error.

Flavour composition systematic. By varying the confidence-level cuts in the lifetime tags, the flavour compositions were changed such that the flavour enrich-

ment for u, d, s and b quarks changed by $\pm 4\%$ and for c quarks by -4% and $+2\%$ (it was found to be very difficult to get higher purities). The flavour composition of the different distributions obtained with these changes are specified in table 5.3. The results of the fit changing one of the corresponding enriched flavour distributions at a time are given in table 6.7.1.

Changed distribution	χ^2/n_{df}	$\alpha_s(M_Z)$
uds-enr. (-)	303.8/213	0.1253 ± 0.0056
uds-enr. (+)	309.1/213	0.1263 ± 0.0054
c-enr. (-)	307.1/213	0.1218 ± 0.0055
c-enr. (+)	308.9/213	0.1246 ± 0.0055
b-enr. (-)	289.2/213	0.1259 ± 0.0054
b-enr. (+)	294.8/213	0.1252 ± 0.0053

Table 6.4: Results of $\alpha_s(M_Z)$ for different flavour compositions tagged distributions. For each fit, the tagging cuts of a given distribution are changed, giving the flavour compositions specified in the table 5.3. A fit is performed with this new distribution but leaving the rest untouched. The value of the χ^2/n_{df} and $\alpha_s(M_Z)$ is presented.

The maximum change was $\Delta\alpha_s = 0.004$, which was taken as an additional systematic error due to flavour composition of the tagged data samples. This result can be confirmed from the extrapolation of the results presented in table 6.7.1 where the nominal values of the purities were varied artificially by $\pm 1\%$. The shifts in $\alpha_s(M_Z)$ were ~ 0.001 . Assuming a linear variation of the fitted value on $\alpha_s(M_Z)$ with variation of the Monte Carlo estimates in the purities, the estimated systematic error would be equivalent to an uncertainty of $\pm 4\%$ in the purity estimates from the Monte Carlo.

Considering also the fit error, the total experimental error of $\alpha_s(M_Z)$ is $\Delta\alpha_s(exp) = \pm 0.005(fit) \pm 0.002(norm) \pm 0.004(purity) = \pm 0.007(exp)$.

6.7.2 Theoretical errors

A priori, the scales μ_i, μ_f and μ_R in figure 6 are unconstrained. When calculating to all orders, any dependence on the choice of the scales vanishes. In finite order perturbation theory, a residual scale dependence is related to the sensitivity to uncalculated higher order terms. In order to avoid large logarithms in the theoretical

Changed purity	χ^2/n_{df}	$\alpha_s(M_Z)$
uds-enriched -	308.9/213	0.1262 ± 0.0054
uds-enriched +	308.3/213	0.1251 ± 0.0055
c-enriched -	308.2/213	0.1250 ± 0.0055
c-enriched +	306.6/213	0.1266 ± 0.0052
b-enriched -	308.5/213	0.1247 ± 0.0054
b-enriched +	306.4/213	0.1269 ± 0.0053

Table 6.5: Results of $\alpha_s(M_Z)$ for different purities in the tagged distributions. For each fit, the nominal purity taken from the MonteCarlo was changed by $\pm 1\%$. The fits were done with the same nominal distributions but with this ‘artificially’ changed purity.

predictions, the natural choice of scales is $\mu_i^2/s_i = \mu_f^2/s_f = \mu_R^2/\mu^2 = 1$ and these are the values used for the standard analysis. Varying the scales allows to estimate the theoretical uncertainties of the prediction.

The renormalization and factorization scales were parametrized according to $\mu_{R,F} = f_{R,F}\sqrt{s}$, being the nominal value determined by $\ln f_{R,F} = 0$. The scale values were varied, one at a time, in the range $-1 \leq \ln f_{R,F} \leq 1$, giving the values of $\alpha_s(M_Z)$ presented in table 6.7.2.

Value of the scale	χ^2/n_{df}	$\alpha_s(M_Z)$
$\ln f_R = -1$	307.3/213	0.1242 ± 0.0052
$\ln f_R = +1$	307.3/213	0.1281 ± 0.0056
$\ln f_F = -1$	310.8/213	0.1196 ± 0.0049
$\ln f_F = +1$	304.7/213	0.1310 ± 0.0061

Table 6.6: Results of $\alpha_s(M_Z)$ for different factorization and renormalization scale assumptions. The theoretical errors are taken from the maximum variation of each scale.

The quality of the fit is totally insensitive to the renormalization scale and does not change substantially with the changes made in the factorization scale. Taken the two scales as independent sources of theoretical error, the theoretical systematic error on $\alpha_s(M_Z)$ will be given by

$$\Delta\alpha_s(\text{theory}) = \pm 0.002(\mu_R) \pm 0.006(\mu_F). \quad (6.51)$$

which, combined in quadrature with the experimental error gives

$$\alpha_s(M_Z) = 0.126 \pm 0.007(\text{exp}) \pm 0.006(\text{theory}) = 0.126 \pm 0.009. \quad (6.52)$$

6.8 Consistency checks

Several additional consistency checks were carried out in the analysis varying some of the assumed parameters.

6.8.1 Parametrization scale variation

Although there are reasons to choose the parametrization scale at 22 GeV as was explained in section ??, repeating the fit with different parametrization starting points will prove, not only that the value of α_s does not strongly depend on this assumptions, but also that the result is not widely sensitive to the choice of the parametrization of the fragmentation functions. This last point comes from the fact that, given the fragmentation functions in the exact form ?? at an initial scale $\mu_i = s_0$, the evolution to a final scale μ_f will transform them to a similar shape which, however, will be outside the original parameter space. Thus varying the scale of the parametrization is a way to probe slightly different families of functions $D(x)$.

Two different scales were tried for the parametrization scale giving the results: (PUT THIS IN A TABLE???)

$$\alpha_s(M_Z) = 0.1246 \pm 0.0059 \quad \text{for} \quad s_0 = 45.0 \text{ GeV} \quad (6.53)$$

$$\alpha_s(M_Z) = 0.1240 \pm 0.0063 \quad \text{for} \quad s_0 = 91.2 \text{ GeV} \quad (6.54)$$

which deviate less than 0.002 from the nominal result. The chiesquared values differ in less than one unit from the standard fit.

6.8.2 Parametrization of the non-perturbative effects

Although the parametrization of the non-perturbative terms is justified in the Monte Carlo (section ??), it is worth to probe the dependence of the result of it.

The energy dependence of the non-perturbative evolution terms was changed from $1/\sqrt{s}$ to $1/s$, as is known to be in deep-inelastic scattering. The result was $\alpha_s(M_Z) = 0.1265 \pm 0.0052$ in perfect agreement with the nominal result. The value of the χ^2 increased in less than one unit and the value of the non-perturbative parameter changed to $h_0 = -2.7 \pm 2.0$. Thus, the data themselves cannot confirm that the energy dependence of the non-perturbative evolution terms is of the form $1/\sqrt{s}$ but the change in $\alpha_s(M_Z)$ is negligible with the $1/s$ assumption. However, the nominal result is well supported by Monte Carlo studies (section ??) and phenomenological theoretical assumptions (section ??).

The rescaling ansatz used in reference [?]

$$x = x' \left[1 + h_1 \cdot \left(\frac{1}{\sqrt{s}} - \frac{1}{\sqrt{s_0}} \right) \right] \quad (6.55)$$

was also tried. The fit to all the parameters gave a $\chi^2 = 314.1/213$, and a result of $\alpha_s(M_Z) = 0.108 \pm 0.010$ with a correlation of 87% between α_s and h_1 . This correlation precludes a simultaneous measurement of both parameters. In reference [?], the value of h_1 was estimated from the HERWIG Monte Carlo, giving a value of $h_1 = -0.5$. Moving and fixing the value of this parameter from its fitted value ($h_1 = -1.03 \pm 0.44$) to the estimated one gave $\alpha_s(M_Z) = 0.1184 \pm 0.0050$ which is compatible with the nominal result although is totally dependent of the assumptions made in the HERWIG Monte Carlo.

6.8.3 Dependence on the fit range

The dependence on the choice of the fit interval was studied by varying the lower and upper bounds of the fit range around the nominal value of $x_{\min} = 0.1$ and $x_{\max} = 0.8$. The results on α_s (shown in table 6.8.3) are compatible with the nominal result. The χ^2 of the fit degrades considerably when going to smaller x_{\min} , indicating that the parametrization of the fragmentation functions and non-perturbative terms is not suitable for very small x . This is because Going to larger values of x_{\min} amounts to giving up much of the available data, and the fit of all 16 parameters becomes unstable, with correlations of more than 90% between many of the variables.

Finally, the whole parametrization except $\alpha_s(M_Z)$ was fixed to the nominal result, and the strong coupling constant was fitted, using the same formalism as

Interval	χ^2/n_{df}	$\alpha_s(M_Z)$	h_0
0.1-0.5	162.4/148	0.1215 ± 0.0071	-0.077 ± 0.108
0.05-0.8	702.2/259	0.1331 ± 0.0036	-0.253 ± 0.084
0.15-0.8	244.7/180	0.1326 ± 0.0100	-0.094 ± 0.169

Table 6.7: Results of the fit to $\alpha_s(M_Z)$ to different intervals in x . All the parameters are fitted.

before in independent x -intervals of size $\Delta x = 0.1$ between $x = 0.1$ and $x = 0.8$. The different fitted values are shown in table 6.8.3. All results were found to be statistically compatible with the nominal one, verifying that scaling violations over the full x range are described by one single coupling constant.

Interval	χ^2/n_{df}	$\alpha_s(M_Z)$
0.1-0.2	51.9/73	0.1313 ± 0.0040
0.2-0.3	47.8/57	0.1234 ± 0.0073
0.3-0.4	33.9/54	0.1200 ± 0.0078
0.4-0.5	50.1/43	0.1249 ± 0.0075
0.5-0.6	41.1/39	0.1255 ± 0.0075
0.6-0.7	43.5/37	0.1261 ± 0.0075
0.7-0.8	52.8/37	0.1247 ± 0.0088

Table 6.8: Results of the fit to $\alpha_s(M_Z)$ to different intervals in x . All the parameters except $\alpha_s(M_Z)$ are fixed.

6.8.4 Different experiment combinations

Removing the data of one experiment at a time from the overall fit leads to the results presented in table 6.8.4.

All the results are compatible with the nominal result except for the case of removing the information of the gluons coming from the three jet symmetric events and the data from Tasso at 35 GeV and Mark II at 29 GeV.

The case of the removal of the gluon information is explained because doing this, the only remaining information on the gluon fragmentation function is the one coming from the constraint in the longitudinal and transverse cross-sections

Removed distribution	χ^2/n_{df}	$\alpha_s(M_Z)$
Tasso (22 GeV)	299.8/200	0.1235 ± 0.0057
Tasso (35 GeV)	255.3/200	0.1152 ± 0.0060
Tasso (44 GeV)	293.5/200	0.1251 ± 0.0054
Mark II (29 GeV)	258.9/199	0.1391 ± 0.0055
TPC/ 2γ (29 GeV)	297.4/201	0.1278 ± 0.0056
Cello (35 GeV)	296.2/191	0.1236 ± 0.0055
Amy (55 GeV)	299.5/206	0.1257 ± 0.0053
Tasso (35 GeV) + Mark II (29 GeV)	221.6/186	0.1307 ± 0.0065
Delphi (91.2 GeV)	272.1/191	0.1268 ± 0.0054
Aleph (91.2 GeV) All	286.1/190	0.1244 ± 0.0054
Aleph (91.2 GeV) uds	289.0/190	0.1252 ± 0.0054
Aleph (91.2 GeV) c	283.6/190	0.1242 ± 0.0095
Aleph (91.2 GeV) b	238.7/190	0.1230 ± 0.0064
Aleph (91.2 GeV) gluon	300.6/208	0.1045 ± 0.0079
Aleph (91.2 GeV) Longitudinal	297.8/197	0.1275 ± 0.0057

Table 6.9: Results of $\alpha_s(M_Z)$ for removing one distribution at a time. The table shows the result of the fit when removing the specified distribution

through equation ???. There, the values of β_s and the normalization of the gluon fragmentation functions become strongly correlated and this makes the correlation between β_s and α_s to increase up to 75% which makes the result for α_s unreliable.

The large variations removing one of the two other experiments can be justified because they are the distributions that mostly contribute to the overall χ^2 . Removing one of them make the other have a strong weight in the fit, therefore shifting the value of α_s . Removing both experiments at the same time gives a compatible result with the standard one.

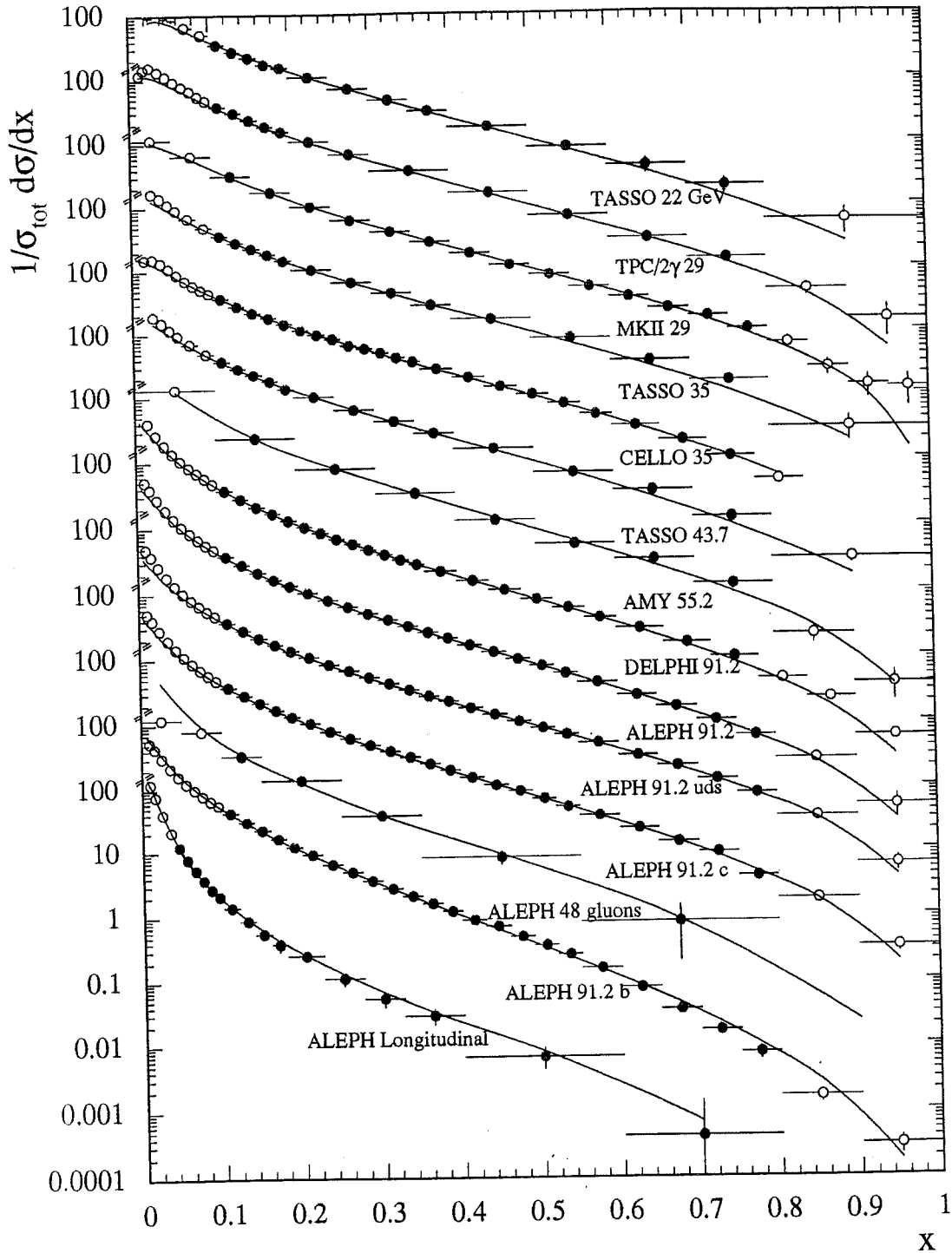


Figure 6.3: Scaled-energy distributions used in the QCD fit. Only the dark points enter the fit. Errors shown include statistical and systematic uncertainties. The lines represent the result of the fit.

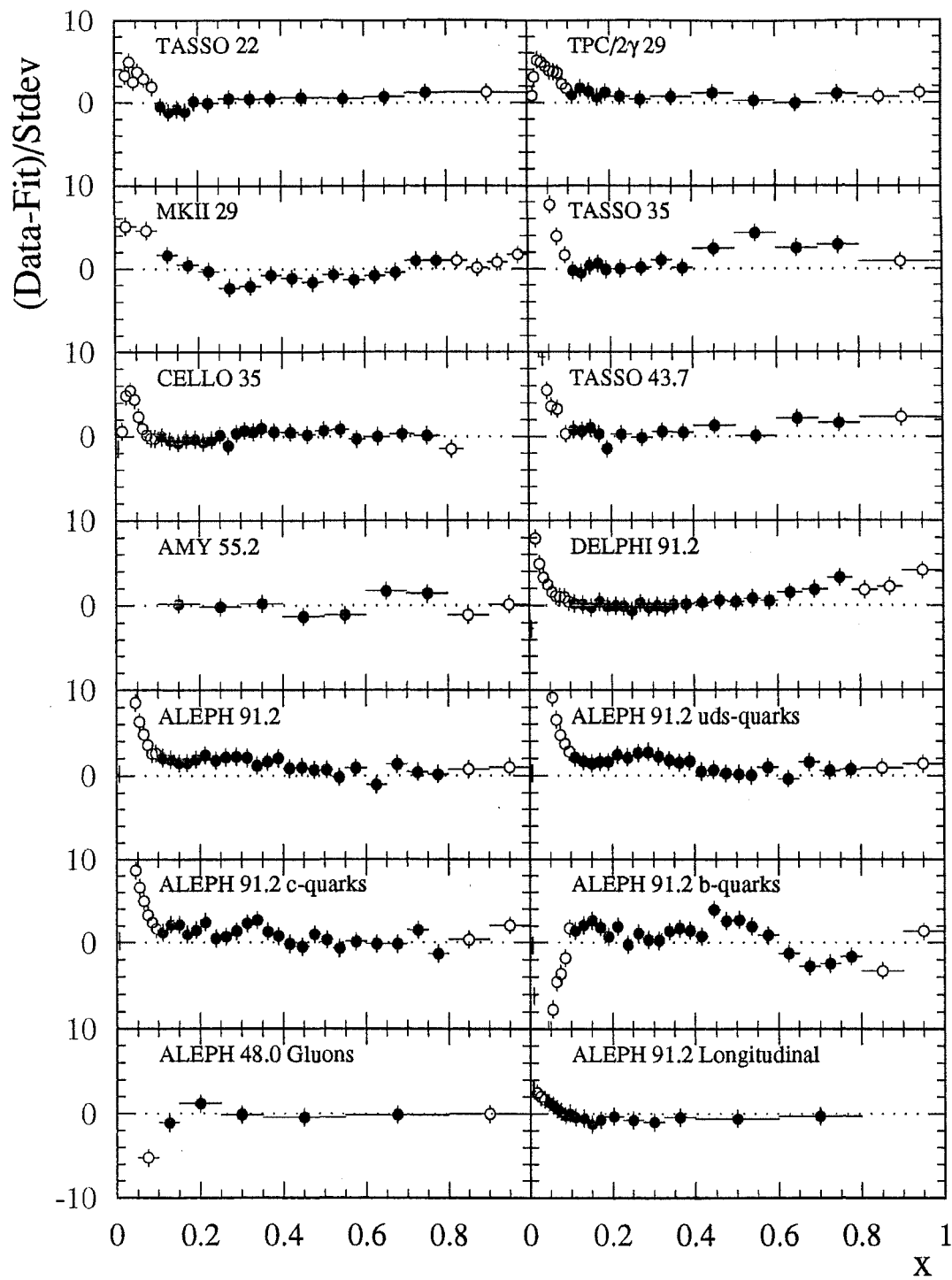


Figure 6.4: Differences between the fit result and the data in number of standard deviations (including statistical and systematic errors) for all the distributions used in the fit. Only the dark points enter the fit.

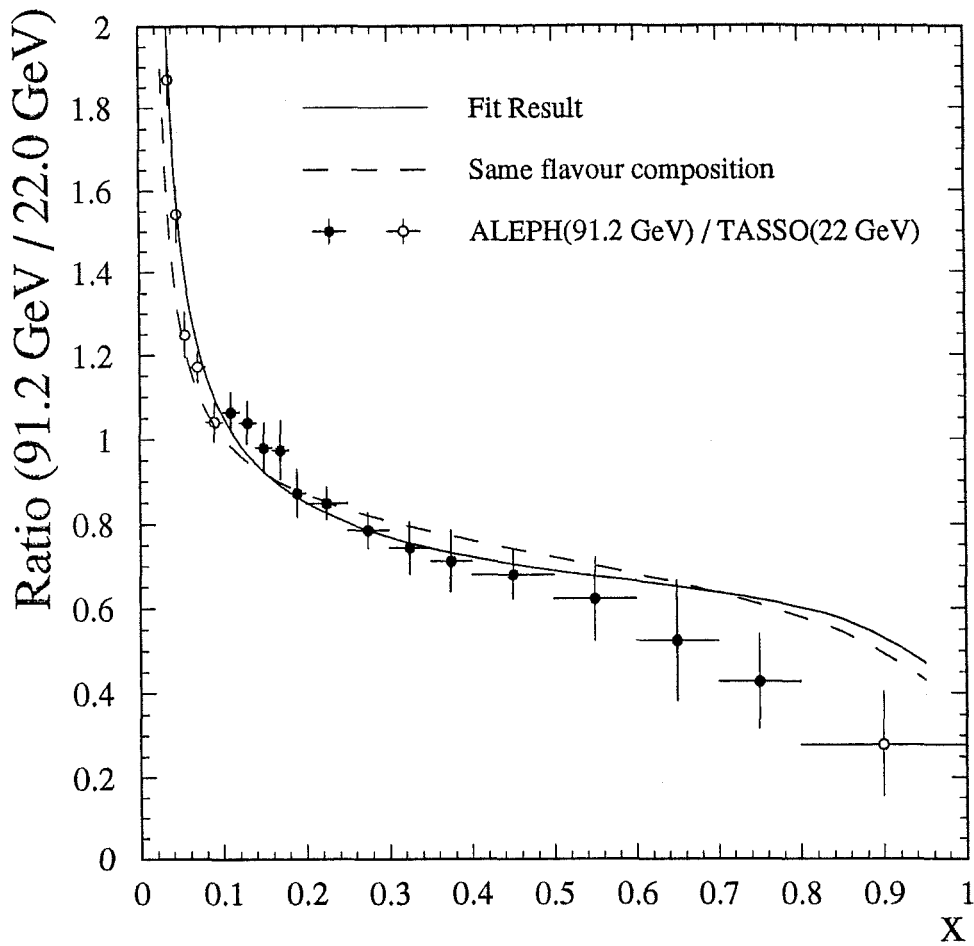


Figure 6.5: Ratio of inclusive cross sections at $\sqrt{s} = 91.2 \text{ GeV}$ and $\sqrt{s} = 22 \text{ GeV}$ compared to the QCD prediction. The full dots contributed in the global fit.

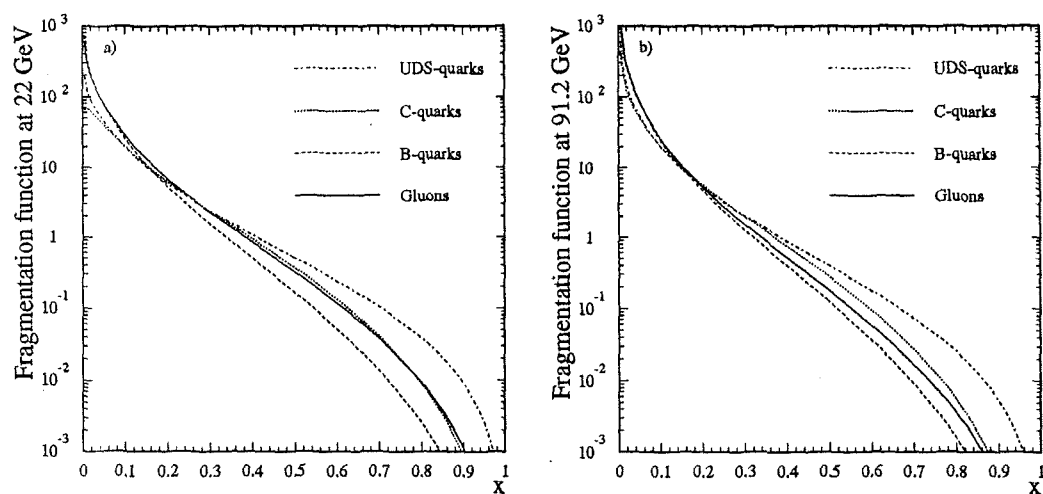


Figure 6.6: Fragmentation functions at (a) 22 GeV and (b) 91.2 GeV obtained from the fit. It can be observed the generally harder spectra of the functions at lower energy. The gluon fragmentation function becomes closer to the b-fragmentation as the energy increases.